# STRUCTURAL INVESTIGATIONS OF ZEOLITES

Thesis by
Paul A. Wagner

In Partial Fulfillment of the Requirements
for the Degree of
Doctor of Philosophy

California Institute of Technology
Pasadena, CA

1999
(Submitted May 24, 1999)

## Acknowledgments

None of the work presented within this thesis would have been possible without the solid support and vision of Professor Mark E. Davis. His confidence in my abilities and his leadership style have allowed me to achieve more than I thought I was capable of when I came to Caltech four years ago. The lessons learned beyond the laboratory setting from Professor Davis will be carried with me and relied upon throughout my life.

I am professionally indebted to many people who have provided me with guidance and insight into many research problems and include: Dr. Clemens Freyhardt, Dr. Ralf Grosse-Kunstleve, Dr. Stacey I. Zones and Dr. John Higgins. I am particularly indebted to Professor Osamu Terasaki for accepting me into his laboratory and providing a stimulating and supportive environment in which to work. My stay in Japan with Prof. Terasaki is certainly one of the highpoints of my Ph.D. career.

I have met numerous truly remarkable individuals here at Caltech many of whom I am proud to call friends. In particular, I wish to acknowledge the support and friendship of Alex Katz; it is a rare pleasure to have a friend of Alex's character and intellectual strength. Numerous fine evenings of great culinary experiences followed by impromptu adventures are very fondly remembered. Shervin Khodabandeh is acknowledged for many stimulating conversations and charismatic insights into life; Larry and Dara Beck for their relentlessly good-heartedness and for helping me see how to savor life more by slowing it down a bit; Cheryl Anderson (Dartt) for her unwaveringly good humor and openness; Hector Gonzalez for numerous intemperate (and a few not-so-intemperate) adventures; Patricia Andy for remaining stoic in the face of life. Additionally, I would like to thank Jon Holmes, Javier Garcia Martinez, Arik Johnson, Joel Berg and Arron Samuels for many colorful and indelible experiences. Sherry Shams has added depth and perspective to my life, thank you for seizing the moment and not letting go. You continuously enrich and invigorate me. Finally, I wish to thank my parents and relatives for their unwavering love and support, certainly I would never have been able to accomplish what I have were it not for them.

## Abstract

Microporous materials (including zeolites) that contain molecular-sized pores and cavities have found wide-spread use in industry as molecular sieves for chemical separations, as ion-exchangers for detergents and as heterogeneous, shape-selective catalysts. The number of unique molecular sieve structures discovered over the past few decades has burgeoned and currently is over 121.

Knowledge of the crystal structure of these microporous solids can provide important insights into their properties that can ultimately lead to the design of desirable materials. However, the structure solution of microporous materials can be challenging because they tend to form as micron or submicron sized crystals that are too small for single crystal X-ray analysis. Thus, the objective of this work is to develop and apply new techniques for solving the structures of microporous materials that tend to form micro- and nanocrystals and to utilize these structural investigations to gain a more thorough understanding of the zeolite/ organic structure directing agent (SDA) interactions that lead to the observed zeolite phase selectivity in their synthesis.

In the absence of single crystal data, structure solution and refinement have typically required the use of powder X-ray data. The difficulty in solving crystal structures from powder X-ray data is that the three dimensions of information available in a single crystal data set are collapsed into one dimension (d-spacing) in a powder X-ray data set. If the reflections in the powder X-ray data are significantly overlapping then solving the crystal structure from this data can be extremely difficult. Several techniques are applied here for solving microporous crystal structures from powder X-ray data.

The structure solution of CIT-5 (California Institute of Technology Number 5), a new high-silica molecular sieve synthesized under hydrothermal conditions in the presence of N(16) methylsparteinium and lithium cations, is obtained though an iterative process of model

building and comparison of the simulated powder X-ray data with the experimental powder X-ray data. Rietveld refinement of the synchrotron powder X-ray data supports the symmetry and space group assignment for the structure as $Pmn2_1$ (No. 31) with refined unit cell parameters of a=13.6738(8) Å, b=5.0216(3) Å and c=25.4883(7) Å (V=1750.1 $Å^3$) and confirms that CIT-5 is the first ordered zeolite to contain one-dimensional extra-large pores circumscribed by 14 tetrahedral-atoms (14 MR).

Computational techniques for solving the structures of microcrystals from powder X-ray data are continuing to increase in sophistication and capability. The crystal structures of two high-silica molecular sieves, SSZ-44 and SSZ-35, are solved using Fourier recycling and represents the first application of this new computational technique for solving novel high-silica zeolite structures from powder X-ray data. Both materials contain unusual 1-dimensional pores circumscribed by 10 and 18 membered-rings, and are the first high-silica zeolites found that possess pores containing greater than 14 membered-rings.

Electron diffraction data, obtained from a transmission electron microscope (TEM), has inherent advantages over X-ray data for analyzing small crystals due to the stronger interaction between the electron beam and matter compared to X-rays. This stronger interaction allows a single crystal diffraction data set to be obtained from much smaller crystals. Provided that the interaction of the incident electron beam with the crystal is nearly kinematical direct methods can be used as a powerful tool for obtaining the phase information required to solve the crystal structure.

The development of electron diffraction methods for solving the structure of nanocrystals is described and the application of this technique to solve the structure of a large-pore, high-silica zeolite, SSZ-48, that contains an occluded organic structure directing agent is presented. The structure is confirmed by electron diffraction refinement and by high resolution transmission electron microscopy and is found to contain a one-dimensional pore system circumscribed by 12 tetrahedral atoms (12 MR). SSZ-48 is the most complex

three-dimensional material to be solved at atomic resolution using electron diffraction methods and illustrates the power of electron diffraction data for resolving the structures of materials that form crystals too small for standard single crystal X-ray analysis.

These investigations into the structural details of micro- and nanocrystalline microporous materials can be utilized to gain a more thorough understanding of the zeolite/ organic structure directing agent (SDA) interactions that lead to the observed zeolite synthesis phase selectivity. Two studies are conducted to probe the relationship between the organic structure directing agent and the zeolite framework that is formed from its use.

The first study probes the interaction between the CIT-5 framework and the N(1)-methyl-α-isosparteine SDA **I** that is found to be a more effective structure directing agent for CIT-5 than the diastereomer N(16)-methylsparteinium **II** originally used to direct this new high-silica zeolite. Molecular modeling calculations reveal that **I** is capable of forming a greater number of van der Waals interactions with the framework than **II** thereby providing a greater degree of stabilization for the CIT-5 structure as compared to **II**.

Finally, a study into the guest/host interactions between three new zeolite structures, SSZ-35, SSZ-36 and SSZ-39 and the 37 organic structure directing agents that are capable of directing for these zeolites is presented. The size and shape of the organic SDAs presented in this study are designed in order to obtain novel, open framework zeolites. The design effort focused on synthesizing large rigid spheroidal SDAs that will preclude the crystallization of the commonly observed clathrates and straight 1-dimensional channel system zeolites that result when either small or rigid elongated molecules are employed as SDAs. Computational calculations of the organic/inorganic energy of interactions provided significant insights into the observed zeolite phase selectivity by the organic SDAs. The molecular modeling investigations presented here highlight the potential for developing a rational route to the design of desirable zeolite frameworks.

## Table of Contents

# I. Zeolite Structure Solution

# List of Figures

## Chapter One

## Chapter Two

## Chapter Three



## Chapter Four

## Chapter Five



## Chapter Six

# List of Tables

## Chapter One



## Chapter Two



## Chapter Three

## Chapter Four



## Chapter Five



## Chapter Six

# CHAPTER ONE

# Introduction and Objectives

Reprinted in part with permission from:

[P. Wagner and M. E. Davis *Photofunctionalized Zeolites : From Zeolite Synthesis to Applications;* M. Anpo, Ed.; NOVA Sciences, New York; **1999** (in press)]

Abstract

Crystalline microporous materials (including aluminosilicate zeolites) have found widespread industrial applications because they possess large internal surface areas that are accessible through uniform molecularly sized channels and cavities. The number of unique molecular sieve structures discovered has burgeoned over the past few decades and currently they number over 121. Here, we will provide an overview of the current state of zeolite technology including the synthesis, characterization and uses of these important materials.

Introduction

The term zeolite is derived from the Greek words "zeo" meaning "to boil" and "lithos" meaning "stone." This name originates from the Swedish mineralogist Cronstedt who discovered a silicate mineral in 1756 that intumesced when heated in a blowpipe flame [1]. Zeolites are composed of a 3-dimensionally connected framework of silica and alumina tetrahedra containing an O/[Si+Al] =2. Each $Al^{+3}$ in the oxide framework requires an extra-framework charge-balancing cation to maintain electroneutrality of the material (Figure 1). The charge balancing cation for the as-synthesized zeolite can be inorganic, organic or organometallic in nature, and in some cases can be exchanged post-synthetically to industrially useful cations such as protons and transition-metals.

In addition to aluminosilicates, crystalline microporous materials can be aluminophosphate based (Figure 1). The $AlPO_4$ framework is electroneutral, however the aluminum or phosphorous tetrahedral-atoms can be substituted by a number of metal and non-metal atoms that results in a charged framework requiring extraframework cations for charge-balancing. Additional unique elemental compositions of microporous materials have been reported recently, e.g., silicon

nitride based [2]. However, these solids account for only a small fraction of the known structures and have not, as yet, found significant industrial applications. Therefore we will not focus on these materials here.

As previously mentioned, approximately 121 different microporous structures have been reported to the International Zeolite Commission (IZC) for structure codes [3]. Each microporous material is assigned a three-letter code by the IZC (the IZC code will be used through-out the remainder of this article). These microporous materials are distinguished by the size and dimensionality of the pores and/or cages that they possess (see Table 1).

The cage or pore size is denoted by the number of oxygen atoms (likewise the number of tetrahedral atoms) circumscribing the pore or cavity, *e.g.*, a pore circumscribed by $n$ oxygen-atoms is referred to as an $n$ membered-ring pore, or more simply, $n$-MR. If the framework is composed of cages that can only be accessed through windows that are 6 MR or smaller the material is referred to as a clatherate. Microporous materials containing pores and/or cages with molecular-sized windows (containing 8 MRs or larger) can have industrial utility for separations, ion-exchange, and catalysis.

In the discussions to follow, we will equate the dimensionality of the pore system to the degree of interconnections between the pores within the structure. For example, a 1-dimensional (1-D) pore system contains pores that do not interconnect with each other, a 2-dimensional (2-D) pore system allows interconnection of pores in only one crystallographic direction, and a three-dimensionally connected (3-D) pore system contains interconnections of the pores in two crystallographic directions and thus allow molecules to travel through the material in three dimensions (in the direction of the pores or through the interconnections in either of

the remaining two crystallographic directions). Examples of the different pore system dimensionalities are presented in Figure 2.

Industrial Uses

Over 1 million metric tons of synthetic zeolites were produced in 1994 in the U.S., Western Europe, Japan and Canada with a market value of approximately $1.5 billion. The use of synthetic zeolites as ion-exchangers in detergents accounted for 906 thousand metric tons, zeolite catalysts accounted for 102 thousand metric tons, and 55 thousand metric tons of zeolites found industrial use as desiccants and adsorbents[4].

The usefulness of aluminosilicate zeolites for ion-exchange applications depends on the framework aluminum content, the structure of the zeolite, and the positions of the charge balancing cations within the structure [5]. As mentioned earlier, each tetrahedrally coordinated aluminum imparts a negative charge to the framework and requires a charge balancing counter-cation in order to maintain the overall electroneutrality of the material. Zeolite A, LTA (Figure 3), that has a Si/Al=1, is the primary zeolite used for ion-exchange in detergents because it possesses a high extra-framework cation density resulting from the high aluminum content. The Si/Al ratio of 1 for LTA is the lowest observed in zeolites because Al-O-Al connections are not favored in tetrahedrally connected frameworks due to unfavorable electrostatic interactions (Loewensteins rule). For ion-exchange applications, Na-LTA (LTA with $Na^+$ as the counter cation) is used in detergents as a builder to exchange "hard" cations (e.g. alkaline earth metal cations such as $Ca^{+2}$) with "soft" cations (e.g. $Na^+$) that increases the efficacy of the surfactants in the detergent [6]. A recent advance in the use of zeolites for ion-exchange is maximum

aluminum containing zeolite P (GIS) [7], or MAP, that also has a Si/Al = 1. The recent increased dependence on zeolite ion-exchangers in detergents is primarily a response to social and regulatory pressures to replace environmentally unfriendly phosphates [8].

Microporous materials are also heavily relied upon by the petrochemical and chemical industries for performing shape-selective, heterogeneous catalysis. Selectivity is achieved because of the uniformly sized channels and cavities in which the reactions occur (Figure 4). High-silica aluminosilicate zeolites are in demand because they possess the required strong acidity and thermal stability to perform acid catalyzed reactions on hydrocarbon molecules. The acidity of zeolites arises from the exchange of the charge balancing counter-cation to the proton form (Bronstedt acidity) and also due to the electronegativity of the metal center within the framework (Lewis acidity). Some examples of acid zeolites that have found use in industry and some of the important reactions that they catalyze are listed in Table 2.

High-silica, titanosilicate microporous materials such as Ti-ZSM-5 (TS-1) [9] are also in demand for their ability to perform shape-selective oxidation and epoxidation reactions on hydrocarbon molecules. Figure 5 outlines a number of the oxidation reactions that can be carried out over TS-1. A key to the success of this material is that isolated $Ti^{4+}$ can be stabilized by substituting for $Si^{4+}$ in the crystalline framework. A particularly interesting catalytic oxidation reaction performed over TS-1 is the ammoximation cyclohexanone to produce ε-caprolactam (a precursor for nylon-6) [10]. The reaction yields an oxime that can then undergo

a Beckmann rearrangement to ε -caprolactam. EniChem developed this process in a 15,000 ton per year pilot plant in 1994 [11].

While some aluminophosphate-based molecular sieves are too thermally and/or hydrothermally unstable for most industrial applications, workers at Chevron recently reported using SAPO-11 (silicoaluminophosphate number 11, AEL) [12] for the isodewaxing of lubeoils[13]. Lubeoil applications require saturated hydrocarbon molecules that are branched and contain some ring structure. Waxes (n-paraffins) are undesirable in lubeoils because they tend to crystallize at relatively high temperatures adversely effecting the viscosity (or pourpoint) of the oil. The straight chain hydrocarbons (n-paraffins) have been separated from the desirable iso-paraffins using solvents. However, catalytic dewaxing, that is catalytically converting or removing n-parrafins, has recently gained prominence. Mobil has explored the use of ZSM-5 to preferentially hydrocrack the undesirable wax molecules[14]. Hydrocracking paraffins converts a valuable feedstock to a less valuable, lower molecular weight feedstock (producing $C_3$-$C_4$ molecules from high molecular weight hydrocarbon molecules). Workers at Chevron have found that Pt-SAPO-11 (a silicoaluminophosphate molecular sieve containing Pt clusters) isomerizes the n-paraffins to iso-paraffins with high selectivity and conversions [15]. The higher selectivity of Pt-SAPO-11 over MFI for isomerizing the waxes is presumed to be due to the slightly narrower 1-dimensional channel system of SAPO-11 that precludes the secondary cracking reactions that can occur within the larger multidimensional pores of MFI

Molecular sieves are also utilized as adsorbents and separation media. For example, zeolite A (LTA) is used in the UOP ISOSIV process for the separation of branched from normal hydrocarbons. The normal paraffins are selectively

adsorbed because the branched paraffins are too large to enter the pore system of LTA.

The industrial separation of nitrogen from oxygen in air also utilizes molecular sieves as selective adsorbents. $Li^+$ exchanged zeolite X (FAU) with a Si/Al ~1 is in industrial use for separating nitrogen from oxygen in air; the nitrogen is preferentially adsorbed due to the interaction of the quadropler moment of nitrogen with the $Li^+$ cations[16]. This zeolite based adsorbent is economical for nitrogen volumes up to 50 tons per day and oxygen volumes up to 200 tons per day (for larger quantities the gases are cryogenically separated) [17].

Synthesis

In nature, zeolites commonly form as geothermally heated ground water passes through silicate volcanic ash. Typically, in silica-rich volcanic deposits, heulandite and analcime tend to form while in low-silica deposits chabasite, phillipsite and natrolite are favored[18]. Early attempts to synthesize zeolites centered around recreating the high-pressure, high-temperature conditions found in nature. Barrer demonstrated the first successful zeolite synthesis (mordenite (MOR))[19], while Milton developed large-scale zeolite syntheses at low-temperatures and pressures that allowed zeolites to gain industrial importance [20]. These zeolite syntheses relied on the presence of alkali metal hydroxides in the synthesis mixture to serve as a mineralizing agent. The alkali metal cations also play a role in the structure direction of the particular zeolite that forms. Building on the concept of cationic structure direction, Barrer and Denny [21], and Kerr and Kokotailo[22] subsequently expanded the range of cations from the inorganic metal cations to organic cations. Using a quaternized amine (tetramethylammonium, TMA), Barrer successfully synthesized sodalite (SOD) and zeolite A (LTA). The

TMA cations were found to be occluded within the sodalite cages [23]. Because the TMA molecules are too large to diffuse into the sodalite cages the molecules must have been occluded during the crystal growth and thus confirmed the structure directing effect of the TMA. Following this initial discovery of organic structure direction, tetraethylammonium (TEA), tetrapropylammonium (TPA) and tetrabutylammonumium (TBA) were employed to synthesize the zeolites beta (BEA) [24], ZSM-5 (MFI)[25] and ZSM-11/ZSM-5[26], respectively. The syntheses are all carried out under basic hydrothermal conditions (pH > 10), that enhances the dissolution and condensation reactions necessary for zeolite crystallization from the silica species present in solution.

A typical MFI synthesis procedure using TPA is as follows:

Gel Composition

$2.0\ TPABr : 2Na_2O : 20SiO_2 : 500H_2O$

2.94 g of NaOH pellets and 9.8 g TPABr are dissolved in 165.14 g of $H_2O$. 22.11 g of amorphous silica is then added and the gel is mixed to an even consistency. The mixture is charged into Teflon line autoclaves or sealed quartz tubes and heated at 150 °C for 24-48 hrs.

Organic Molecule Properties Favoring Zeolite Formation

The use of organic molecules to direct the formation of high-silica zeolitic phases has become commonplace and typically involves the use of a quaternized amine. Kubota and coworkers have studied the relationship between the ability of organic molecules to direct the formation of high-silica zeolites and the $C/N^+$, the

hydrophobicity, and the rigidity of the molecules[27]. Rigid organic molecules are found to favor zeolite formation presumably because molecules that undergo fewer conformational changes are better able to stabilize a smaller number of oxide frameworks through non-bonded organic/inorganic interactions. An optimal $C/N^+$ ratio is found to be between 12-13, and is interpreted in terms of the hydrophobicity of the organic molecule. Partitioning studies of quaternized amines between an aqueous solution and an organic chloroform layer reveals that organic molecules possessing intermediate hydrophobicity/hydrophilicity (as indicated by the similar preference of the molecule for the organic layer and the aqueous solution) tend to direct the formation of zeolites (Figure 6)[27, 28].

The effects of varying the hydrophilicity of tetrapropylammonium derivative molecules on high-silica ZSM-5 (MFI) formation has been examined by several researchers [28, 29]. TPA molecules readily crystallize MFI (ZSM-5) and display intermediate hydrophobicity as indicated by ~35% partitioning to the organic chloroform layer from the aqueous solution. As a test of the effects of the hydrophilicity of the organic molecule on the zeolite synthesis, the hydrophobicity of TPA was systematically decreased by replacing the propyl groups with ethanol groups (ethanoltripropylammonium (1OH), diethanoldipropylammonium (2OH) and tetraethanolammonium (TEAO) ). The TPA derivatives all possess geometries and volumes that are very similar to the parent TPA molecule and provide a direct test of the effects of increasing hydrophilicity of the organic molecule on the high-silica zeolite formation. As may be expected, increasing the number of ethanol groups increases the hydrophilicity of the molecules (as determined by the partitioning experiments). 1OH shows 14% partitioning to the organic layer, 2OH shows less than 8% partitioning, while TEAO shows no partitioning to the organic layer [28]. MFI syntheses were conducted under identical conditions and the TPA

derivatives were varied between the synthesis experiments. In the case of TPA, the onset of crystallization is detected after only three hours and crystallization is complete within 4 hours. Increasing the hydrophilicity of the organic molecule slightly to the 1OH derivative results in an decreased nucleation rate (5 hours until the onset of crystallization) and crystallization is not completed until after 11 hours. Further increases in the hydrophilicity (2OH and TEAO) result in no crystallization after more than 2 weeks. Additional crystallization kinetics using the 1OH and the 2OH derivatives, were conducted using ZSM-5 seed crystals (10 wt %). The seeded 1OH synthesis results in rapid crystallization of ZSM-5 in 5 hrs, while the seeded 2OH synthesis proceeds very slowly (less than 40% yield after 20 h), indicating that no viable nuclei exist in the 2OH synthesis in the absence of seeds but that slow crystal growth can be sustained in the presence of added nucleating centers (ZSM-5 seed crystals).

The ability of quaternized amines that posses intermediate hydrophobicity to crystallize zeolites can be understood in terms of the displacement of the hydrophobic hydration sphere of partially ordered water molecules about the organic molecules by silica that orders around the organic entities and condenses into the three dimensionally connected oxide network. If the organic molecule is too hydrophobic it cannot dissolve in the aqueous synthesis solution and will tend to phase separate. However, if the molecule is too hydrophilic, then the water molecules interact too strongly with the organic and cannot be readily diplaced by the silica. Early work by Frank revealed that water tends to order about quaternized amines and referred to the ordered water about the organics as "icebergs" [30]. Further work revealed that aqueous solutions of tetra n-butyl ammonium cations (1 -2 molal) precipitate crystalline hydrates of the amine with the crystalline hydrates containing 32 water molecules for each tetra n-butyl ammonium ion [31]. The

hydrate possesses a large unit cell (tetragonal a=23.6 Å, c=12.4 Å), and was hypothesized to possess dodecahedron cages that enclathrate the charged organic molecules. Additionally, silica hydrates that contain double-four-ring silica anions have been synthesized and are found to crystallize into a zeolite-A like structure [32]. The structure is composed of discrete double four ring anions of silica and water molecules that are not condensed together but are ordered about tetrabutylammonium cations. These results support the hydrophobic hydration sphere model in which water molecules are ordered or partially ordered about an organic cation and are displaced by silica subunits that organize about the organic and condense together to form the zeolite structure. The driving force for the displacement of the ordered water by silica is the favorable interaction energies between the organic and silica (enthalpy) and the entropy gain from the ordered water that is released from the hydrophobic hydration sphere of the organic.

Zeolite Nucleation and Crystal Growth

Recent studies have probed the assembly process of zeolite nucleation and crystal growth *in-situ* over length scales of 0.17nm-6000nm using Ultra Small Angle X-ray Scattering (USAXS), Small Angle X-ray Scattering (SAXS) and Wide Angle X-ray Scattering (WAXS) [33]. Using these techniques, three particle populations were observed during the synthesis of pure-silica ZSM-5 from TPA: 2.8 nm organic/silica composite particles, 10 nm organic/silica composite particles and the final crystals. In the case of low-alkalinity syntheses (Si/OH=3.02), two populations of particles were initially observed: a 2.8 nm particle population and a 10 nm particle population[34]. However, in the high-alkalinity syntheses (Si/OH < 2.65), only a 2.8 nm particle population was observed other than the final crystals [35]. The low alkalinity syntheses (Si/OH = 3.02), that initially contain the 10 nm

particles, also crystallized faster than the higher alkalinity syntheses (Si/OH = 2.42), that only contained the 2.8 nm composite particles, however the growth rate of the crystals was found to be independent of alkalinity. Crystallization occurred very slowly for the high-alkalinity (Si/OH = 2.12) synthesis. Seed crystals were added (0.02 wt%, 0.1 wt%, 0.5 wt%, and 2.5 wt%) to the Si/OH = 2.12 synthesis solution to determine whether the slow crystallization in this high alkalinity synthesis solution is a result of slow crystal growth or the lack of viable nuclei. The growth rates are similar between all of the seeded syntheses and are comparable to the growth rates observed in the unseeded lower alkalinity syntheses. The final crystal size increased as the amount of seed crystals was reduced and it is calculated that 1/3 of the MFI seeds nucleated crystallization [34]. The low alkalinity MFI syntheses (containing the 10 nm particles) therefore must possess a greater number of viable nuclei than the high alkalinity MFI syntheses. The entities for growth are present in the high alkalinity syntheses solution, that contain only the 2.8 nm composite particles. However the assemblies required for nucleation are not.

In light of these experiments, the nucleation and growth of pure-silica MFI from TPA is believed to occur through the aggregation of the 2.8 nm particles into 10 nm aggregates. However, only a portion of the 10nm aggregates are viable nuclei, possibly because the primary particles must aggregate into an *ordered* arrangement (analogous to the silica hydrate discussed previously) prior to becoming a viable nuclei (we have observed 7-10 nm particles possessing the MFI structure from these syntheses by TEM). As the ordered 10 nm particles nucleate crystal growth the 10 nm particles that are not ordered disaggregate and provide silica to the growing crystals. This model for zeolite nucleation and crystallization is illustrated in Figure 7 [36].

The MFI primary particle size of 2.8 nm is also initially observed in syntheses of MFI using different organic molecules, including: trimethylene-bis(N-hexyl, N-methyl-piperidinium), that crystallizes MFI from a gellating system, tetrabutylammonium (TBA) that directs for an intergrowth between MFI and MEL, and dimers and trimers of TPA that crystallize MFI. These results suggests that the size of the primary particle is independent of the structure-directing agent, the preparation method and the alkalinity for a particular zeolite phase.

These scattering experiments were repeated using different organics that direct for different zeolite phases and it is found that the size of the primary particles that initially forms is related to the particular zeolite phase. The primary particle size for MFI is 2.8 nm, the primary particle size for beta (BEA) synthesized from a gellating system using the SDA trimethylene-bis(N-hexyl, N-methyl-piperidinium) is found to be 2.6 nm, the same system can crystallize Si-ZSM-12 (MTW) depending on the synthesis conditions[37]. The primary particle size for Si-ZSM-12 (MTW) is found to be 1.5 nm. These primary particle sizes correspond to the size of the unit cell for each of these phases (MFI 2.0 x 2.0 x 1.3, BEA: 1.3 x 1.3 x 2.4 nm, and MTW: 2.5 x 0.5 x 2.5), and suggests that the primary particles contain a portion of the order required to form the viable nuclei from which zeolite crystallization commences. These results support the zeolite nucleation and crystallization model outlined above.

## Organic-Inorganic Interactions Leading to Zeolite Formation

### Overview

In examining the organic-inorganic interactions that lead to zeolite formation we have focused our attention on the high-silica zeolites. The electrostatic interaction energy between the disordered framework defect sites and the charge

balancing extraframework cations in these high-silica zeolite systems is neglected as it is constant from framework to framework. Therefore, the non-bonded van der Waal energy dominates the interaction between the organic molecules and the inorganic oxide framework. The effects of the organic-inorganic van der Waal interactions have been divided into three categories depending on the degree of interaction. In *templating,* there is a one to one correspondence between the organic molecule and the framework resulting in a silica structure that possesses similar symmetry to the organic molecule,*e.g.*, ZSM-18 (MEI) [38]. Next the term *structure directing* is employed to designate strong van der Waals interactions between the organic molecule and the oxide framework. However, there is not a correlation between symmetry of the organic molecule and the framework. Molecules that can act as structure directing agents may possess some degree of rotational or translational freedom within the oxide framework. Finally, *pore-filling* refers to weak van der Waal interactions between the organic molecule and the framework; the molecule simply fills the pore of the zeolite to decrease the internal surface area and slow the zeolite dissolution kinetics.

Templating (rare)

ZSM-18 synthesized using the triquaternium cation pictured in Figure 8 is an exceptional example of organic templating of an inorganic zeolite structure [38]. The point group symmetry of the triquat is $D_{3h}$, and is located within the ZSM-18 cages that possess the same symmetry as the organic. Furthermore, molecular modeling studies by Lobo and Davis reveal that the molecules are rigidly confined by the oxide framework and are not free to rotate or translate within the ZSM-18 cages [39]. As pointed out by Lobo, if the organic molecules are free to rotate within the zeolite pores then the framework needs to conform to the geometry of the

volume generated by the rotation of the molecule rather than the volume of the molecule itself. This lack of free rotation is a distinguishing feature of templating, and implies that the synthesis of the highly sought after chiral zeolite beta from optically active molecules must proceed through organic templating that inhibits free rotation of the molecules within the pores and imparts the symmetry of the chiral template molecule to the oxide framework.

Structure Direction

Structure direction of a high-silica zeolite by an organic molecule is a more common occurrence than templating. Pure-silica ZSM-5 that is structure directed by TPA is found to contain the TPA molecules at the channel intersections with the propyl arms extending into both the sinusoidal channels and the linear channels[40]. Due to the lack of rigidity of the propyl moieties of the TPA molecules, the symmetry of the ZSM-5 structure does not conform to the symmetry of the TPA molecules, however the TPA molecules are tightly held within the channel of the ZSM-5 material and can only be removed through calcination. This entrapment of the organic molecules occurs during crystal growth. Direct experimental support for the strong organic-inorganic van der Waals interaction is obtained from $^{1}H$-$^{29}Si$ cross polarization, magic angle spinning (CP MAS) NMR spectra from freeze dried TPA-ZSM-5 samples that indicates the protons of the organic molecules are in van der Waals contact with the oxide framework (~3.3 Å) [29]. This short range van der Waals interaction is observed to occur before the onset of the long range order detected by X-ray diffraction. No $^{1}H$-$^{29}Si$ cross polarization occurs if TMA molecules are substituted for the TPA molecules indicating that no van der Waals interactions occur between the TMA and the silica, and consequently no zeolite formation is observed.

Additional evidence of the influence of non-bonded van der Waals organic-inorganic interactions on zeolite formation is provided by the molecular modeling experiments of Harris and Zones in which they calculate the van der Waals energy of stabilization of nonasil (NON) from a variety of organic amine molecules [41]. The calculated van der Waals interaction energy correlates with the experimental crystallization times and indicates that stronger organic/inorganic van der Waals interaction stabilizes the growing zeolite framework.

Pore Filling

Pore filling describes a weak interaction of the organic molecule with the oxide framework in which there is not a unique specificity between the organic molecule and the inorganic framework. For example there are at least 13 known organic molecules that can be used in the synthesis of ZSM-48, and many of these organic molecules can be employed to crystallize different zeolite phases depending on the synthesis conditions [42]. It is hypothesized that in the case of pore-filling the organic molecules serve only to protect the internal surface from attack and dissolution by the mineralizing agent.

Zeolite Structure Solution

Overview

A particular challenge after a new microporous material is synthesized is to solve the crystal structure, *i.e.,* determine the arrangement of atoms in space. Typically, a large number of nuclei form in the zeolite synthesis mixture which

results in the formation of very small crystallites (micron to submicron in size) as seen in the SEM images in Figure 9. Although single crystal, synchrotron X-ray techniques continue to advance, crystals on the submicron length scale cannot be solved using standard single crystal X-ray analysis [43]. In the absence of single crystal X-ray data, zeolite crystallographers typically turn to powder X-ray data to attempt to solve new zeolite structures [44]. The unit cell parameters, *i.e.,* the size of the smallest repeat unit in the crystal, are obtained from the positions of the reflections (d-spacings) through an indexation of the powder X-ray data. This unit cell information determines the crystal class of the structure, *i.e.,* cubic, hexagonal, trigonal, tetragonal, orthorhombic, monoclinic, or triclinic, and together with an analysis of the systematic absences in the reflections, provides insight into the space group symmetry of the material. In addition to the information about the size and symmetry of the unit cell that is provided by the positions of the reflections in the powder X-ray data, the intensities of the reflections provide information regarding the arrangement of atoms within the unit cell.

The difficulty in solving a new zeolite structure from the powder X-ray data is that the 3 dimensions of information present in a single crystal data set (roughly the intensity for each hkl reflecting plane) is collapsed into one dimension. The one dimension of information in a powder X-ray data set is the d-spacing (given from Braggs law $2d\sin\Theta=\lambda$). As can be seen in Figure 10, if several reflecting planes with different Miller indices have similar d-spacings, then these reflections will overlap in the powder X-ray data. If the overlap is severe, it becomes difficult to deconvolute the contributions of the each of the overlapping reflecting planes and as a result, information about the arrangement of atoms within the unit cell is lost.

## Zeolite Structure Solution Techniques using Powder X-ray Diffraction Data

### Model Building

Several techniques are available to the zeolite crystallographer in order to overcome the loss of information that results from overlapping reflections in the powder X-ray data. One of the earliest and conceptually simplest techniques applied to solve zeolite structures from the powder X-ray data is that of model building [45-48], zeolite models that fit the specific unit cell parameters and space group information provided by the X-ray data are constructed and the powder X-ray pattern for the model is simulated. The simulated pattern is then compared to the experimental pattern and the process is iteratively continued until a rough match is found. The process is considerably simplified if the material contains a 1-dimensional pore system and if high-resolution TEMs viewed down the channel system can be obtained (as seen for example in Figure 11).

### Direct Methods

If the overlap in the powder X-ray data is not severe, it is possible to extract the integrated intensities from the data and use this data as a pseudo single crystal data set with a direct methods program similar to those used in single crystal analysis. The interested reader is directed to the work of McCusker on Sigma-2 (SGT) in which a direct methods structure solution is obtained from powder X-ray data [49]. While in principle this technique is quite powerful, it typically relies on the material possessing high symmetry and/or small unit cell parameters so that the number of intensities that overlap is small.

### Fourier Recylcing (FOCUS)

More recently, Grosse-Kunstleve together with coworkers McCusker and Baerlocher have developed a computational approach to dealing with powder X-ray

data with extensively overlapping intensities [50]. The powder X-ray data is initially indexed and the space group is established as outlined above. The intensities are extracted and the overlapping intensities are partitioned among the reflecting planes in the overlapping group. The pseudo-single crystal data set is then subjected to a Fourier recycling and topology search followed by a sorting of the topologies.

The Fourier recycling step is initiated by generating a random set of starting phases that is combined with the experimental intensities. The phases and intensities are then Fourier transformed to produce an electron density map. Peaks in the electron density map are then selected based on their "chemical sensibility", that is, peaks that are within a predetermined distance of each other, *e.g.*, corresponding the distance of a Si-Si bond, and that possess the correct coordination, or number of neighboring peaks within a given distance. Tetrahedral coordination is presumed in aluminosilicate and high-silica zeolites. The chemically sensible peaks are then back Fourier transformed to produce a new phase set, and this new phase set is then recombined with the experimental intensities. The Fourier transform is again performed to generate a new electron density map and the process outlined above is repeated. As the phase set converges, a structural model is obtained. The topology generated is filtered based on its connectivity (to account for identical structures with different crystallographic origins) and after the phase convergence the original process is repeated with a new random set of phases. Ultimately a histogram of topologies is obtained and the most commonly occurring structure has typically been found to be the correct structure. This powerful technique has recently been applied to solve the structures of a number of previously unknown zeolite structures [51-53].

Simulated Annealing

Another computational, zeolite structure solution technique is simulated annealing and this method is capable of obtaining the zeolite structure solution in real space[54]. Preceding the structure solution process, the unit cell parameters and the space group information are required. In addition, the porosity or density information is required and can be obtained from adsorption or indirectly from solid-state NMR that can provide information about the number of unique T-sites within the crystal[55]. Next, atoms are randomly placed within the unit cell and a figure of merit for the configuration is calculated. The figure of merit is a weighted sum of a number of contributors including the T-T distance the T-T-T angle, the average T-T-T angle, the coordination of the T-atoms, and the match between the simulated X-ray powder pattern from the atom distribution and the experimental powder X-ray data. In order to minimize this figure of merit as a function of the atomic configuration, simulated annealing is employed; simulated annealing is a very effective technique for minimizing multidimensional functions. The positions of the atoms in the unit cell are allowed to vary. Each atom is allowed to move within a sphere centered about its current position (the size of the sphere of potential movement is defined by the temperature). The zeolite figure of merit is then recalculated for the new configuration and if the new figure of merit is lower than the old figure of merit the configuration is accepted. However, if the new figure of merit is greater than the present figure of merit then the move is accepted only if $e^{-(\Delta H/T)}$ is greater than a random number between 0 and 1 (where $\Delta H$ is the difference between the new figure of merit and the old figure of merit). At high temperatures most new configurations are accepted and as the temperature is reduced fewer moves to configurations with higher figures of merit are allowed. As the annealing progresses the final configuration should be near the global minimum in the figure

of merit. Using this technique zeolites with up to 6 atoms in the asymmetric unit are capable of being solved and in a test of 64 structures with 6 or fewer unique T-atoms the technique was successful for 57 of the cases, and has been used recently to solve a number of unknown zeolite structures[56-58].

More recently, Falcioni and Deem have modified the Monte Carlo code to include a parallel tempering minimization routine together with the simulated annealing and found that this technique is better able to minimize the zeolite figure of merit as a function of the atomic configurations [59]. The code was tested on 118 reported zeolite structures. Simulated powder X-ray data were generated from these zeolite structures for the profile range of $5° < 2\Theta < 35°$ ($\lambda$=1.54056) with a peak resolution of $\Delta 2\Theta = 0.06°$, and the match of the models generated by the code to these simulated patterns contributed to the figure of merit. Using this parallel tempering/Monte Carlo technique, Falconi and Deem were able achieve remarkable success solving most of the 118 zeolite structures. However the code is limited to materials that contains no extra framework material and that are connected tetrahedrally in 3 dimensions. The most complex zeolite solved using their method is NES (NU-87) that contains 17 unique T-atoms (although their program did encounter difficulty with MWW that contains only 8 unique T-atoms).

Structural Refinement

Once the initial zeolite model is obtained, the final step of the structural verification is the refinement. The Rietveld refinement technique is most commonly applied to powder X-ray and neutron data sets for refining the crystal structure and instrumental parameters in order to fit a calculated powder X-ray pattern to the experimental powder X-ray data[60]. The size of the unit cell and the

wavelength of the radiation determines the positions of the reflections for the calculated powder pattern and the positions of the atoms in the unit cell provide the initial reflection intensities. These initial reflection profiles are then modified by parameters that model sample effects such as crystallite size, microstrain, preferred orientation and the presence of impurities. Instrumental effects that contribute to aberrations in the experimental diffraction profile in the form of peak asymmetries are also modeled and include axial divergence, flat specimen geometry, and specimen transparency in addition to modeling the peak broadening contributions from the x-ray source and the receiving slit geometry.

The final intensity model is a convolution of the previously mentioned effects in addition to the multiplicity of the reflections due to symmetry, the Lorentz-polariztion factor, and the scale factor (which scales the calculated intensity to the experimental intensity) and is represented by the following function:

$$y_i = s\sum_{hkl} L_{hkl}M_{hkl}|F_{hkl}|^2P_{hkl}\Phi(2\theta_i-2\theta_{hkl})+b_i$$

where $y_i$ is the calculated intensity, s is the scale factor, $L_{hkl}$ is the Lorentz-polarization factor, $M_{hkl}$ is the multiplicity factor, $F_{hkl}$ is the structure factor, $P_{hkl}$ accounts for preferred orientation of the crystals in the sample holder, $\Phi$ represents the profile function and b is the background function.

A weighted difference of this calculated intensity and the observed intensity is the function that is minimized in the Rietveld refinement:

$$S_y = \sum_i w_i(y_i(obs)-y_i(calc))^2$$

where y is the intensity, and $w_i$ is equal to $1/\sigma^2$ ($\sigma$ is the standard deviation for the observation).

Once the approximate atomic coordinates, the unit cell parameters and the space group are determined, the structure factors $|F_{hkl}|$ are calculated using the following equation:

$$|F_{hkl}| = \{[\sum\sum f_N \cos 2\pi(hx_N+ky_n+lz_N)]^2 + [\sum\sum f_N \sin 2\pi(hx_N+ky_n+lz_N)]^2\}^{1/2}$$

where $f_N$ is the atomic scattering factor, (hkl) are the Miller indices and $x_N$, $y_N$, $z_N$ are the coordinates of the atoms in the unit cell. One summation is over atoms of a particular type, and the other is over all atoms of that type in the unit cell. The square of this structure factor is proportional to the intensity observed in the experimental pattern.

The atomic positions are one set of parameters that can be refined to optimize the calculated intensity. However, the atomic positions can also be restrained in the refinement. These restraints are termed soft constraints. The constraints can be either bond lengths or bond angles where the weight given to the constraints can be varied. The constraints are given a high weight at the initial stages of the refinement in order to prevent the bond lengths or angle from assuming chemically unreasonable values. As the refinement proceeds the weight given to the bond length and angles can be lessened until they are finally removed. The constraints are imposed according to the following equations:

$$S_y = \sum_i w_i(y_i(obs)-y_i(calc))^2$$

$$S_c = \sum_i w_i(r_{i0} - r_i)^2$$

$$S = S_y + c_w S_c$$

where $S_y$ is defined as above, $r_{i0}$ is the value for the restrained bond length or angle and $r_i$ is the calculated bond length or angle. S is the function to be minimized and $c_w$ is the variable weight given to the constraint.

The profile function $\Phi$ discussed above accounts for the shape of the reflection. As mentioned previously, the shape of the intensity profile is determined by both sample and instrumental effects. Sample effects that influence peak shape include crystallite size, microstrain and crystal defects such as faulting or twinning. Peak asymmetries are instrumental effects that arise from axial divergence, flat specimen geometry, and specimen transparency. Instrumental effects also contribute to peak broadening as a result of the receiving slit geometry and the x-ray source. A variety of peak shape functions are available with the typical Rieveld refinement programs such as GSAS[61]. Most of these peak shape functions allow the modeling of the fraction and degree of asymmetry in the peak profile along with variables that account for sample shift, peak width, and sample transparency.

The background parameter $b_i$ is used to model the non-Bragg scattering intensity observed in the data. It is important to correctly account for the background profile because an incorrectly modeled background can lead to refinement errors resulting from poor fits to the observed intensities. The background parameter $b_i$ can be obtained either by fitting the background with a predefined function or it can be obtained by interpolation between a set of points.

Often, the background is interpolated between a set of points because of the difficulty in correctly modeling the amorphous scattering profile common for zeolites. For silicate materials this diffuse amorphous scattering peaks at a d spacing of about 3 Å which corresponds to the inter-atomic bond distance for a Si-O-Si bond (~3.2Å).

The Rietveld refinement is an attempt to model a calculated intensity to an observed intensity using a variety of the parameters previously mentioned. The quality of the fit can be determined using a residual; two of the more common are defined as follows:

$$R_p = \Sigma|y_i(obs)-y_i(calc)|/\Sigma y_i(obs)$$

$$R_{wp} = \{\Sigma(w_i(y_i(obs)-y_i(calc))^2/\Sigma(w_i y_i(obs))^2\}^{1/2}$$

The refinement is carried out in order to minimize the value of these residuals.

Many problems can arise in a refinement that will result in high values of the residuals (indicates a poor fit of the model to the experimental data). An important aspect of the Rietveld refinement is the order of the parameter refinement. Different parameters in the refinement can behave quite differently. A poor choice in the order of the parameter refinement can lead to a diverging rather than converging model; a situation in which the residuals would get larger with successive cycles in the refinement rather than getting smaller.

It is also possible to reduce the residual values to a local rather than to a global minimum. Many times this can be avoided by varying the starting model significantly and re-refining the model to determine if the same residual is obtained. Problems in the refinement also arise when more parameters are refined than the

data can support. This may occur for a structure which has a very high degree of peak overlap. Typically there is enough data to support the refinement. In general there are 5-6 times as many observations as parameters to refine in a powder data set, compared to orders of magnitude more observations than parameters in a single crystal analysis. Additionally, simultaneous refinement of site occupancy and temperature factors has been found to cause divergence of the refinement. Both the site occupancy and the temperature factors influence the scattering intensity, and as a result if the refined intensity model is a poor fit to the experimental data these parameters can couple to compensate for the mismatch in the observed intensity.

The refinement may proceed by first modeling the background, together with the scale factor, and zero offset. Next, the lattice parameters are refined, after which the profile parameters that account for the peak asymmetries can be refined. Finally the atomic positions are refined subject to highly weighted initial constraints that can be reduced as the refinement proceeds as long as the bond angles and distances remain within chemically reasonable ranges. Finally the temperature factors are refined. Over the course of the refinement one should monitor the convergence of the calculated pattern to the experimental data (R-values), and the parameter shifts. Caution must be exercised in the initial stages of the refinement to prevent too many variables to be adjusted simultaneously; in particular the scale factor, the temperature factors and the population parameters tend to be highly correlated and may lead to a diverging fit if one is not careful. As a final check of the refined model, a Fourier difference map is calculated and examined for electron density peaks that are not accounted for in the initial starting model. The final Fourier difference map should be relatively flat with peak heights below ~1 $e^-/Å^2$ for aluminophosphate and zeolitic materials.

Zeolite Structures

Microporous materials are typically composed of tetrahedrally coordinated atoms that are three dimensionally connected through bridging oxygen atoms, *e.g.*, aluminosilicate zeolites and the most of the phosphate based microporous materials. The framework density of these microporous materials (defined as the number of T-atoms per 1000 $Å^3$) is less than 21 T-atoms/1000 $Å^3$ and materials with framework densities above 21 T-atoms/1000 $Å^3$ are considered to be dense phase materials. Brunner and Meier reported an interesting correlation between the framework density and the size of the smallest T-atom ring within the tetrahedrally connected network[62]. The Brunner-Meier correlation is pictured in Figure 12 and reveals that the smaller the ring size contained within the structure the lower the potential framework density. The implication of this correlation is that the lowest possible framework density material (and potentially the greatest porosity) would consist of 3 MRs. While no microporous MINR=3 (not all T-atoms contained in 3 membered rings) material has been synthesized to date, recent synthetic work has produced a number of MINR=3+ materials (containing but not entirely composed of 3 MRs) [52, 63, 64]. Efforts towards synthesizing a MINR-3 microporous material appears to offer significant potential for producing a new class of valuable, extra-large pore crystalline materials.

In order to understand the three-dimensional zeolite crystal structures it is often helpful to view the material as being composed of basic building units (BBU), i.e., a group of atoms organized into a structural subunit. A number of different basic building units are pictured in Figure 13 along with the zeolite structures that are composed of these BBUs. A notable example is the double six ring basic building unit that is contained in the FAU structure as well as a number of the

aluminophosphate microporous materials. These basic building units are combined together to form the overall crystal structure of the microporous material that can contain cages or pores of varying sizes. It must be emphasized that the use of BBUs is to understand the structural features of zeolites and is not necessarily related to how the zeolites form during their synthesis.

The pore sizes of microporous materials range from ~3 Å to greater than 13 Å (-CLO) [65], with unit cell sizes typically on the order of tens of angstroms. The pore mouth of a molecular sieve may open into a larger cage that is only accessible through constricted widows, for example, LTA contains 8 MR window openings of approximately 5 Å that open into large cages with cage diameters of approximately 12 Å. Table 2 lists the pore sizes and channel interconnections for the microporous materials reported to the International Zeolite Association as of 1996. The International Zeolite Associations' Structure Committee is responsible for verifying the structure solution of new microporous materials and assigning a three letter code to the new structure types. To date 121 new microporous materials have been verified and assigned a code (detailed information on the structures of these materials can be found in the Zeolite Atlas published by the International Zeolite Association)[3] .

## Conclusions

The field of microporous materials is burgeoning both in the number of new materials that have been synthesized recently and also in the understanding of the complex variables leading to the formation of new microporous materials. Outlined here are some recent advances in our understanding of the zeolite nucleation and crystallization from USAX/SAX/WAX studies that indicates that the size of primary organic/inorganic composite particles that form in the initial synthesis mixture is

related to the unit cell size of the material and is unique for the zeolitic phase that forms (ranging from ~1.5nm-3 nm in the systems studied) and is independent of the particular organic molecule or the synthesis parameters for a particular zeolite phase. Experimental results suggest that the primary particles agglomerate to form larger ~10nm aggregates that can become viable nuclei from which the crystallization proceeds. NMR work on zeolite formation from SDAs with similar geometries and volumes but with different hydrophobicities suggests that the early stages of organic/inorganic interaction occurs through the replacement of the ordered hydrophobic hydration sphere about the organic molecules with silica that is both enthalpically and entropically driven. Molecular modeling work corroborates experimental crystallization studies that indicate that the non-bonded van der Waals interactions of the organic molecules with the silicate framework is a controlling factor in the formation of high-silica zeolites. These insights into the features that influence zeolite formation help the understanding of the critical parameters that need to be controlled in order to eventually tailor new microporous frameworks for specific applications

Additionally, several significant advances in the structure solution of zeolites from the powder X-ray data have been outlined. The reduction in the turn around time between the synthesis of a new material and its structure solution allows directed modifications on the synthesis parameters to be conducted in a timely manner in order to systematically develop more desirable materials. The accelerated access to the knowledge of the zeolite structures that these techniques afford is crucial to the advancement of our understanding of the interconnections between the organic structure directing agent and the zeolitic framework that forms.

As illustrated from the entries in Table 1, a large number of new structures have been reported to the International Zeolite Association Structure Committee recently that possess a wide range of channel systems and pore sizes. However, there are still many desirable framework structures yet to be synthesized, *e.g.*, the chiral zeolite beta topology that could have tremendous applications for chiral catalysis and separations. The recent advances in the understanding of zeolite structures and the fundamentals of zeolite formation that are outlined in this article are helping to move zeolite science towards the eventual rational design of desirable new molecular sieves.

Objectives

The objectives of this thesis are twofold: 1) to present the development and application of techniques for solving crystal structures of materials that form as crystals too small for single crystal X-ray analysis, with a particular emphasis on the structure solution of microporous materials, and 2) to utilize the structural information, acquired using these techniques, to study the organic/inorganic interactions that lead to zeolite synthesis phase selectivity.

Chapters 2 and 3 present examples of the current techniques available for solving structures of micro- and nanocrystals from powder X-ray data. In Chapter 2 the technique of model building for solving the structure of the first ordered, high-silica zeolite to contain pores circumscribed by 14 tetradral atoms is outlined. Chapter 3 details the first application of a new computational technique for solving high silica zeolite structures from powder X-ray data, and Chapter 4 outlines the development and application of electron diffraction methods for solving the structure of a molecular sieve from submicron-sized crystals.

The advent of these powerful techniques for solving the crystal structure of microporous materials has dramatically decreased the time between synthesis and structure solution from years to days. As a result, the zeolite chemist can now have rapid feedback on the results of modifications to the organic structure directing agent (SDA) or the synthesis reaction on the product zeolite. Obtaining detailed structural information of the organic SDA/zeolite composite assists the design efforts of the zeolite chemist by providing insights into the organic/inorganic interactions that lead to zeolite phase selectivity.

A long-standing goal of zeolite science has been the *a priori* design of novel zeolite structures, however, before this goal can be achieved a greater understanding of the factors that influence zeolite formation is required. Chapters 5 and 6 present investigations into the organic/inorganic zeolite composites using molecular modeling to correlate the calculated non-bonded SDA/zeolite interaction energy with the observed zeolite phase selectivity from a particular SDA and provide significant insights into the factors that effect zeolite formation.

References


1. Cronstedt, A.F., Akad. Handl. Stockholm, 1756(18): p. 120-130.
2. Huppertz, H. and W. Schnick, Angew. Chem. Int. Ed. Eng., 1997. **36**(23): p. 2651-2652.
3. Meier, W.M., D.H. Olson, and C. Baerlocher, eds. *Atlas of Zeolite Structure Types*. 4 ed. 1996, Elsevier.
4. Smart, M., R. Willhalm, and M. Shoiiro, *Chemical Economics Handbook*, 1998, SRI Consulting. p. 599.
5. Townsend, R.P., in *Introduction to Zeolite Science and Practice*, H. van Bekkum, E.M. Flanigen, and J.C. Jansen, Editors. 1991, Elsevier.
6. Kurzendorfer, C.P., *et al.*, Colloid and Polymer Sci., 1987. **265**: p. 542-547.
7. Baerlocher, C. and W.M. Meier, *GIS*. Z. Kristallogr., 1972. **135**: p. 339.
8. Upadek, A. and P. Krings, in *Zeoliytes as Catalysts, Sorbents, and Detergent Builders*, H.G. Karger and J. Weitkamp, Editors. 1989, Elsevier: London. p. 701-709.
9. Bellussi, G. and V. Fattore, Stud. Surf. Sci. Catal., 1991. **69**: p. 79.
10. Roffia, P., *et al.*, Chim. Ind., 1990. **72**: p. 598.
11. Arpe, H.-J. and K. Weissermal, *Industial Organic Chemistry*. 3 ed. 1997: VCH.
12. Flanigen, E.M., *et al.*, Pure and Applied Chem., 1986. **58**: p. 1351.
13. Maxwell, I.E. and W.H.J. Stork, in *Introduction to Zeolite Science and Practice*, H. van Bekkum, E.M. Flanigen, and J.C. Jansen, Editors. 1991, Elsevier.
14. Chen, N.Y., *et al.*, Oil Gas J., 1977. **75**: p. 165-170.
15. Miller, S.J.,. Microporous Mater., 1994. **2**: p. 439-449.

16. Kirner, J.F., *Nitrogen Adsorption with Highly Li exchanged X-Zeolites with Low Si/Al Ratio*, . 1993: U.S. 5 258 058

17. Gaffney, T.R., Solid State and Mater. Sci., 1996. **1**(1): p. 69-75.

18. Barrer, R.M., *Hydrothermal Chemistry of Zeolites*. 1982: Academic Press.

19. Barrer, R.M., J. Chem. Soc., 1948: p. 127.

20. Milton, R.M., . 1959: U.S. 2882243

21. Barrer, R.M. and P.J. Denny, J. Amer. Chem. Soc., 1961: p. 971.

22. Kerr, G.T. and G. Kokotailo, J. Amer. Chem. Soc., 1961. **83**: p. 4675.

23. Baerlocher, C. and W.M. Meier, Helv. Chim. Acta., 1970. **53**: p. 1285.

24. Newsam, J.M., *et al.*, Proc. R. Soc. Lond. A, 1988. **420**: p. 375.

25. Kokotailo, G.T., *et al.*, Nature, 1978. **272**: p. 437.

26. Kokotailo, G.T., *et al.*, Nature, 1978. **275**: p. 119.

27. Kubota, Y., *et al.*, Microporous Mater., 1996. **6**: p. 213-229.

28. Goretsky, A.V., *et al.*, submitted to Microporous Mater, 1998.

29. Burkett, S.L. and M.E. Davis, J. Phys. Chem., 1994. **98**: p. 4647-4653.

30. Frank, H.S. and M.W. Evans, J. Chem. Phys., 1945. **13**: p. 507.

31. McMullan, R. and G.A. Jeffrey, J. Chem. Phys., 1959. **31**: p. 1231.

32. Bissert, G. and F. Liebau, Zeitshrift fur Kristallographie, 1987. **179**: p. 357-371.

33. de Moor, P.-P.E.A., *et al.*, J. Phys. Chem. B, 1997. **101**: p. 11077-11086.

34. de Moor, P.-P.E.A., T.P.M. Beelen, and R.A. van Santen, submitted to J. Phys. Chem.

35. de Moor, P.-P.E.A., *et al.*, Microporous Mater., 1997. **9**: p. 117-130.

36. de Moor, P.P.E.A., *et al.*, Chemistry Eur. J . *in press*.

37. de Moor, P.-P.E.A., *et al.*, Chem. Mater., 1999, **11**:p. 36-43.

38. Lawton, S.L. and W.J. Rohrbaugh, Science, 1990. **247**: p. 1319.

39. Lobo, R.F. and M.E. Davis, Chem. Mater., 1992. **4**: p. 756-768.

40. van Koningsveld, H., H. van Bekkum, and J.C. Jansen, Acta. Cryst., 1987. **B43**: p. 127-132.

41. Harris, T.V. and S.I. Zones, in *Proceedings of the 10th International Zeolite Conference*. 1994, Elsevier. p. 29-36.

42. Franklin, K.R. and B.M. Lowe, Stud, Surf. Sci. Catal., 1988. **49**: p. 174.

43. McCusker, L.B., Stud. Surf. Sci., 1994. **84**: p. 341.

44. Baerlocher, C. and L.B. McCusker, in *Advanced Zeolite Science and Applications*, J.C. Jansen, *et al.*, Editors. 1994, Elsevier. p. 391-427.

45. Leonowicz, M.E., *et al.*, Science, 1994. **264**.

46. Wagner, P., *et al.*, Chem. Comm., 1997. **22**: p. 2179.

47. Lobo, R.F., *et al.*, J. Am Chem. Soc., 1997. **119**: p. 8474.

48. Freyhardt, C.C., *et al.*, J. Am. Chem. Soc., 1996. **118**: p. 7299.

49. McCusker, L.B., J. Appl. Cryst., 1988. **21**: p. 305-310.

50. Grosse-Kunstleve, R.W., L.B. McCusker, and C. Baerlocher, J. Appl. Cryst., 1997. **30**: p. 985-995.

51. Wagner, P., *et al.*, Angew. Chem. Int. Ed. Eng., 1999 *in press*.

52. McCusker, L.B., *et al.*, Microporous Mater, 1996. **6**: p. 295.

53. Shantz, D., A. Burton, and R.F. Lobo, Micropor. Mesopor. Mater., 1998.

54. Deem, M.W. and M. Newsome, J. Am. Che. Soc., 1992. **114**: p. 7189.

55. Engelhardt, G. and D. Michel, *High-Resolution Solid-State NMR of Silicates and Zeolites*. 1987: Wiley and Sons.

56. Akporiaye, D.E., *et al.*, Chem Commun, 1996. **13**: p. 1553.

57. Campbell, B.J., *et al.*, Chem Commun, 1998: p. 1725.

58. Nenoff, T.M., *et al.*, Zeolites, 1993. **13**: p. 506.

59. Falcioni, M. and M.W. Deem, J. Chem. Phys. 1999, **110**: p. 1754.

60. Rietveld, H.M., J. Appl. Cryst., 1969. **2**: p. 65-71.

61. Larson, A.C. and R.B. Von Dreele, *GSAS - Generalized Crystal Structure Analysis Program*, 1987.

62. Brunner, G.O. and W.M. Meier, Nature, 1989. **337**: p. 146.

63. Rohrig, C. and H. Gies, Angew. Chem. Int. Ed. Engl., 1995. **34**: p. 63.

64. Annen, M.J., *et al.*, Chem. Commun, 1991: p. 1175.

65. Estermann, M., *et al.*, Nature, 1991. **352**: p. 320.

66 Sie, S. T. in *Advanced Zeolite Science and Applications*, J.C. Jansen, *et al.*, Editors. 1994, Elsevier 587.

67. Miller, S.J., *SAPO-11 isodewaxing*. Microporous Mater., 1994. **2**: p. 439-449.

68. Mooiweer, H.H., *et al.*, *FER-olefin isomerization*, in *Zeolites and Related Microporous Materials: State of the Art 1994*, J. Weitkamp, H.G. Karge, and W. Hoelderich, Editors. 1994, Elsevier: Amsterdam. p. 2327-2334.

69. Meima, G.R., *et al.*, *MOR cumene production*, in *Proc. 9th Int. Zeolite Conf.*,R.von Ballmoos, Editor. 1992, Butterworth-Heineman: Montreal. p. 327-334.

**Table 1.1** Pore size and channel system dimensionality for the reported zeolite structures.

| | | |
|---|---|---|
| | | **14-, 18-, & 20-Ring Structures** |
| **-CLO** | **Cloverite** | <100> **20** 13.2 x 4.0*** ⊥ <100> **8** 3.8*** |
| **VFI** | **VPI-5** | [001] **18** 12.1* |
| **AET** | **$AlPO_4$-8** | [001] **14** 7.9 x 8.7* |
| | | **12-Ring Structures** |
| **AFI** | **$AlPO_4$-5** | [001] **12** 7.3* |
| **AFR** | **SAPO-40** | [100] **12** 6.7 x 6.9* ↔ [010] **8** 3.7* |
| **AFS** | **MAPSO-46** | [001] **12** 6.3* ↔ ⊥ [001] **8** 4.0 x 4.0** |
| **AFY** | **CoAPO-50** | [001] **12** 6.1* ↔ ⊥ [001] **8** 4.0 x 4.3** |
| **ATO** | **$AlPO_4$-31** | [001] **12** 5.4* |
| **ATS** | **MAPO-36** | [001] **12** 6.5 x 7.5* |
| ***BEA** | **Beta** | [001] **12** 5.5 x 5.5* ↔ <100> **12** 7.6 x 6.4** |
| **BOG** | **Boggsite** | [100] **12** 7.0 x 7.0* ↔ [010] **10** 5.2 x 5.8* |
| **BPH** | **Beryllophosphate-H** | [001] **12** 6.2 x 6.7* ↔ ⊥ [001] **8** 3.0 x 3.2** |
| **CAN** | **Cancrinite** | [001] **12** 5.9* |
| **CON** | **CIT-1** | [001] **12** 6.4 x 7.0* ↔ [100] **12** 6.8* ↔ [010] **10** 5.1 x 5.1* |
| **DFO** | **DAF-1** | {[001] **12** 7.3 ↔ ⊥ [001] **8** 3.4 x 5.6}*** ↔ {[001] **12** 6.0 ↔ ⊥ [001] **10** 5.4 x 6.4}*** |
| **EMT** | **EMC-2** | [001] **12** 7.4 x 7.6* ↔ ⊥ [001] **12** 6.6 x 6.7** |
| **FAU** | **Faujasite** | <111> **12** 7.4*** |
| **GME** | **Gmelinite** | [001] **12** 7.0* ↔ ⊥ [001] **8** 3.6 x 3.9** |
| **LTL** | **Linde Type L** | [001] **12** 7.1* |
| **MAZ** | **Mazzite** | [001] **12** 7.4* ⊥ **8** [001] 3.4 x 5.6* |
| **MEI** | **ZSM-18** | [001] **12** 6.9* ↔ ⊥ [001] **7** 3.2 x 3.5** |
| **MOR** | **Mordenite** | [001] **12** 6.5 x 7.0* ↔ [010] **8** 2.6 x 5.7* |
| **MTW** | **ZSM-12** | [010] **12** 5.5 x 5.9* |
| **OFF** | **Offretite** | [001] **12** 6.7* ↔ ⊥ [001] **8** 3.6 x 4.9** |
| **-RON** | **Roggianite** | [001] **12** 4.2* |
| **VET** | **VPI-8** | [001] **12** 5.9* |

Table 1.1 (cont'd)

## 10-Ring Structures

| | | |
|---|---|---|
| **AEL** | **$AlPO_4$-11** | [100] **10** 3.9 x 6.3* |
| **AFO** | **$AlPO_4$-41** | [001] **10** 4.3 x 7.0* |
| **AHT** | **$AlPO_4$-H2** | [001] **10** 3.3 x 6.8* |
| **DAC** | **Dachiardite** | [010] **10** 3.4 x 5.3* ↔ [001] **8** 3.7 x 4.8* |
| **EPI** | **Epistilbite** | [100] **10** 3.4 x 5.6* ↔ [001] **8** 3.7 x 5.2* |
| **EUO** | **EU-1** | [100] **10** 4.1 x 5.7* with large side pockets |
| **FER** | **Ferrierite** | [001] **10** 4.2 x 5.4* ↔ [010] **8** 3.5 x 4.8* |
| **HEU** | **Heulandite** | {[001] **10** 3.0 x 7.6* + 8 3.3 x 4.6*} ↔ [100] **8** 2.6 x 4.7* |
| **LAU** | **Laumontite** | [100] **10** 4.0 x 5.3* |
| **MEL** | **ZSM-11** | <100> **10** 5.3 x 5.4*** |
| **MFI** | **ZSM-5** | {[010] **10** 5.3 x 5.6 ↔ [100] **10** 5.1 x 5.5}*** |
| **MFS** | **ZSM-57** | [100] **10** 5.1 x 5.4* ↔ [010] **8** 3.3 x 4.8* |
| **MTT** | **ZSM-23** | [001] **10** 4.5 x 5.2* |
| **NES** | **NU-87** | [100] **10** 4.7 x 6.0** |
| **-PAR** | **Partheite** | [001] **10** 3.5 x 6.9* |
| **STI** | **Stilbite** | [100] **10** 4.9 x 6.1 ↔ [101] **8** 2.7 x 5.6* |
| **TON** | **Theta-1** | [001] **10** 4.4 x 5.5* |
| **WEI** | **Weinebeneite** | [001] **10** 3.1 x 5.4* ↔ [100] **8** 3.3 x 5.1* |
| **-WEN** | **Wenkite** | <100> **10** 2.6 x 4.9** ↔ [001] **8** 2.2 x 2.7* |

## 9-Ring Structures

| | | |
|---|---|---|
| **-CHI** | **Chiavennite** | [001] **9** 3.9 x 4.3* |
| **LOV** | **Lovdarite** | [010] **9** 3.2 x 4.4* ↔ [001] **9** 3.2 x 3.7* ↔ [100] **8** 3.6 x 3.7* |
| **RSN** | **RUB-17** | [100] **9** 3.3 x 4.4* ↔ [001] **9** 3.1 x 4.3*↔ [010] **8** 3.4 x 4.1* |
| **VSV** | **VPI-7** | [011] **9** 3.3 x 4.5* ↔ [01$\bar{1}$] **9** 3.3 x 4.5*↔ [10$\bar{1}$] **8** 3.7 x 3.7* |

## 8-Ring Structures

| | | |
|---|---|---|
| **ABW** | **Li-A** (Barrer and White) | [001] **8** 3.4 x 3.8* |
| **AEI** | **$AlPO_4$-18** | [001] **8** ~3.8 x 3.8* ↔ ⊥ [001] **8** ~3.8 x 3.8** |
| **AFT** | **$AlPO_4$-52** | ⊥ [001] **8** 2.8 x 4.4*** |
| **AFX** | **SAPO-56** | ⊥ [001] **8** 3.4 x 3.6*** |
| **APC** | **$AlPO_4$-C** | [001] **8** 3.4 x 3.7* ↔ [100] **8** 2.9 x 5.7* |

Table 1.1 (cont'd)

| | | 8-Ring Structures (continued) |
|---|---|---|
| **APD** | **$AlPO_4$-D** | [010] 8 2.1 x 6.3* ↔ [001] 8 1.3 x 5.8* |
| **ATN** | **MAPO-39** | [001] 8 4.0* |
| **ATT** | **$AlPO_4$-12-TAMU** | [100] 8 4.2 x 4.6* ↔ [010] 8 3.8 x 3.8* |
| **ATV** | **$AlPO_4$-25** | [001] 8 3.0 x 4.9* |
| **AWW** | **$AlPO_4$-22** | [001] 8 3.9* |
| **BIK** | **Bikitaite** | [001] 8 2.8 x 3.7* |
| **BRE** | **Brewsterite** | [100] 8 2.3 x 5.0* ↔ [001] 8 2.8 x 4.1* |
| **CAS** | **Cesium Aluminosilicate** (Araki) | [100] 8 4.7 x 2.2* |
| **CHA** | **Chabazite** | ⊥ [001] 8 3.8 x 3.8*** |
| **DDR** | **Deca-dodecasil 3R** | ⊥ [001] 8 3.6 x 4.4** |
| **EAB** | **TMA-E** | ⊥ [001] 8 3.7 x 5.1** |
| **EDI** | **Edingtonite** | [110] 8 2.8 x 3.8** ↔ [001] 8 variable* |
| **ERI** | **Erionite** | ⊥ [001] 8 3.6 x 5.1*** |
| **GIS** | **Gismondine** | {[100] 8 3.1 x 4.5 ↔ [010] 8 2.8 x 4.8}*** |
| **GOO** | **Goosecreekite** | [100] 8 2.8 x 4.0* ↔ [010] 8 2.7 x 4.1* ↔ [001] 8 2.9 x 4.7* |
| **JBW** | **NaJ** (Barrer and White) | [100] 8 3.7 x 4.8* |
| **KFI** | **ZK-5** | <100> 8 3.9*** I <100> 8 3.9*** |
| **LEV** | **Levyne** | ⊥ [001] 8 3.6 x 4.8** |
| **LTA** | **Linde Type A** | <100> 8 4.1*** |
| **MER** | **Merlinoite** | [100] 8 3.1 x 3.5* ↔ [010] 8 2.7 x 3.6* ↔ [001]{ 8 3.4 x 5.1* + 8 3.3 x 3.3*} |
| **MON** | **Montesommaite** | [100] 8 3.2 x 4.4* ↔ [001] 8 3.6 x 3.6* |
| **NAT** | **Natrolite** | <100> 8 2.6 x 3.9** ↔ [001] 8 variable* |
| **PAU** | **Paulingite** | <100> 8 3.8*** I <100> 8 3.8*** |
| **PHI** | **Phillilpsite** | [100] 8 3.6* ↔ [010] 8 3.0 x 4.3* ↔ [001] 8 3.2 x 3.3* |
| **RHO** | **Rho** | <100> 8 3.6*** I <100> 8 3.6*** |
| **RTE** | **RUB-3** | [001] 8 3.7 x 4.4* |
| **RTH** | **RUB-13** | [100] 8 3.8 x 4.1* ↔ [001] 8 2.5 x 5.6* |
| **THO** | **Thomsonite** | [101] 8 2.3 x 3.9* ↔ [010] 8 2.2 x 4.0* ↔ [001] 8 variable |
| **VNI** | **VPI-9** | ⊥ [001]{<110> 8 3.5 x 4.0 ↔ [001] 8 3.5 x .3.5 }** |
| **YUG** | **Yugawaralite** | [100] 8 2.8 x 3.6* ↔ [001] 8 3.1 x 5.0* |
| **ZON** | **ZAPO-M1** | [100] 8 2.5 x 5.1* ↔ [010] 8 3.7 x 4.4* |

**Table 1.2**. Zeolites used in the petrochemical industry and their applications

| Zeolite | Dimensionality | Pore Size (Å) | Application |
|---|---|---|---|
| FAU | 3 | 7.4 | Fluid Catalytic Cracking |
| MFI | 2 | 5.3 x 5.6<br>5.1 x 5.5 | Hydrocracking,cracking additive, methanol-to-gasoline (MTG) |
| LTL | 1 | 7.1 | n-hexane to benzene |
| AEL (SAPO-11) | 1 | 3.9 x 6.3 | Isodewaxing |
| FER | 2 | 4.2 x 5.4<br>3.5 x 4.8 | Isomerization of C4 olefins for methyl-tert-butyl ether synthsesis |
| MOR | 2 | 6.5 x 7.0<br>2.6 x 5.7 | Cumene synthesis |

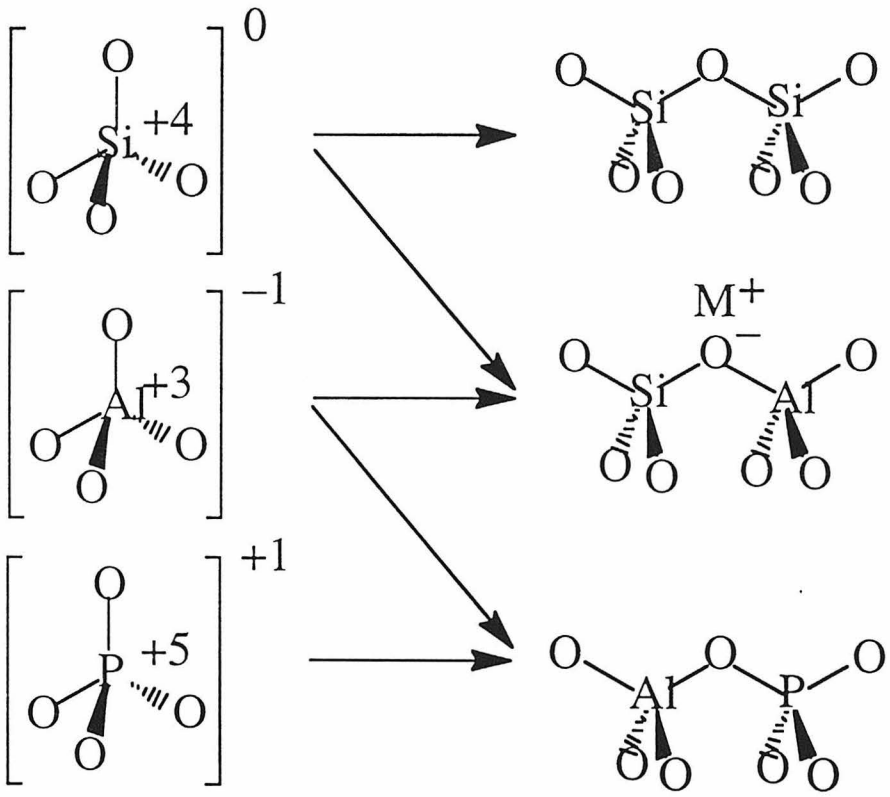


**Figure 1.1** Condensed, tetrahedrally coordinated silicon results in an electroneutral framework ($Si^{+4}$). Aluminum has a +3 valence and therefore the alumina tetrahedra impart a -1 charge to the silicate framework. Phosphorous has a +5 valence and therefore the phosphorous oxide tetrahedra has a +1 charge and forms an electroneutral aluminophosphate framework with a Al/P = 1.

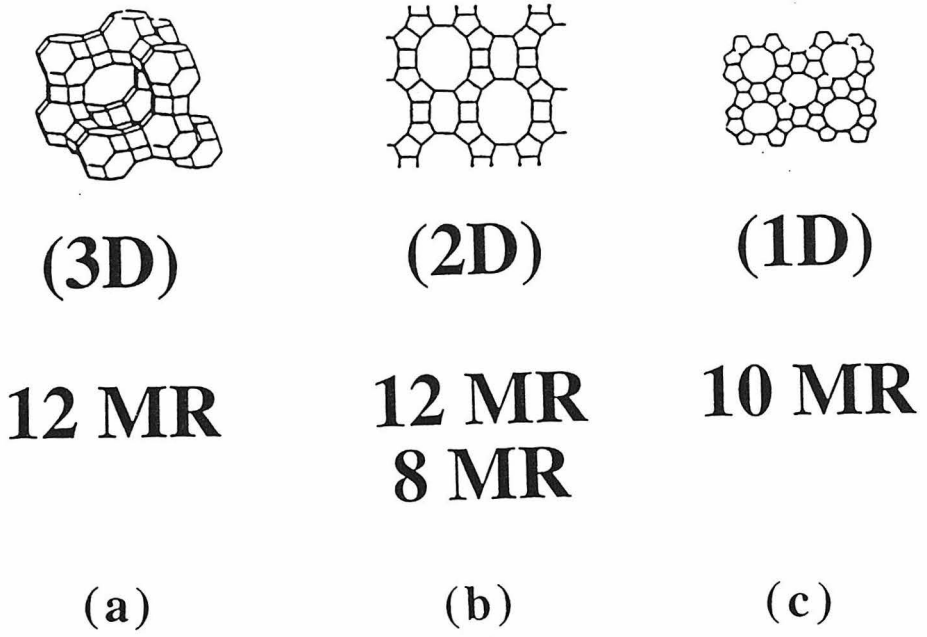


**Figure 1.2**. (a) FAU that possesses a three dimensional pore system (b) MOR that possesses a two dimensional pore system and (c) TON that possesses a 1-dimensional pore system in which the pore do not interconnect with each other.

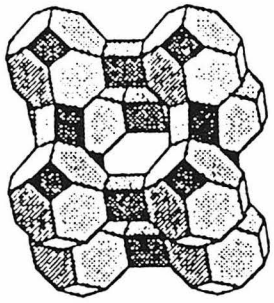

**Figure 1.3.** Zeolite A (LTA) that is widely used as a builder in detergents.

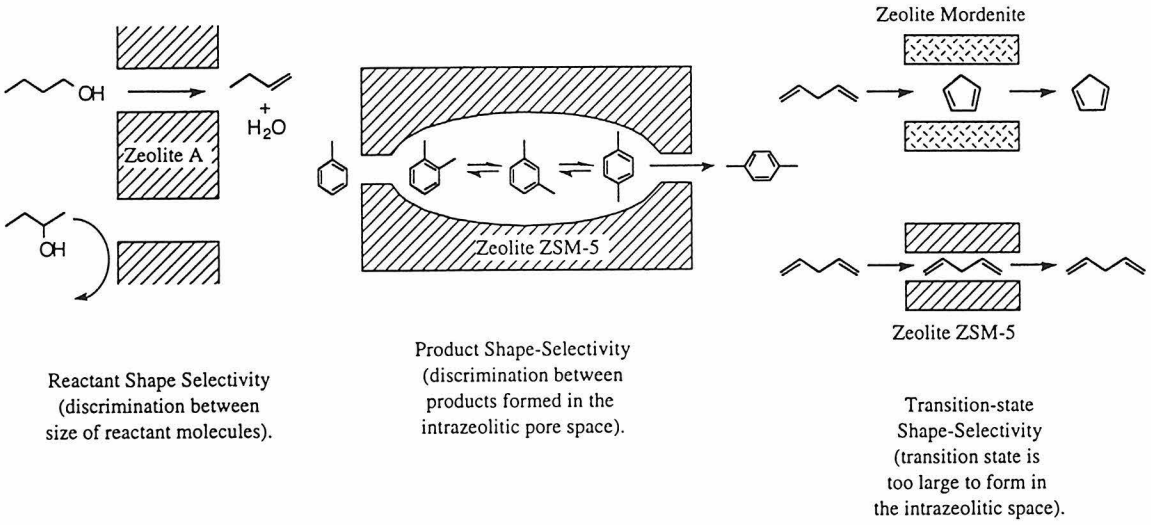


**Figure 1.4**. Zeolite shape selectivity can be based on (1) reactant selectivity in which certain reactant molecules are prevented from entering the pores and reacting due to their size, (2) product selectivity in which a product that is too large to diffuse out of the pore is trapped and (3) transition-state selectivity in which a transition-state that is to large for the pore syustem is prevented from forming.

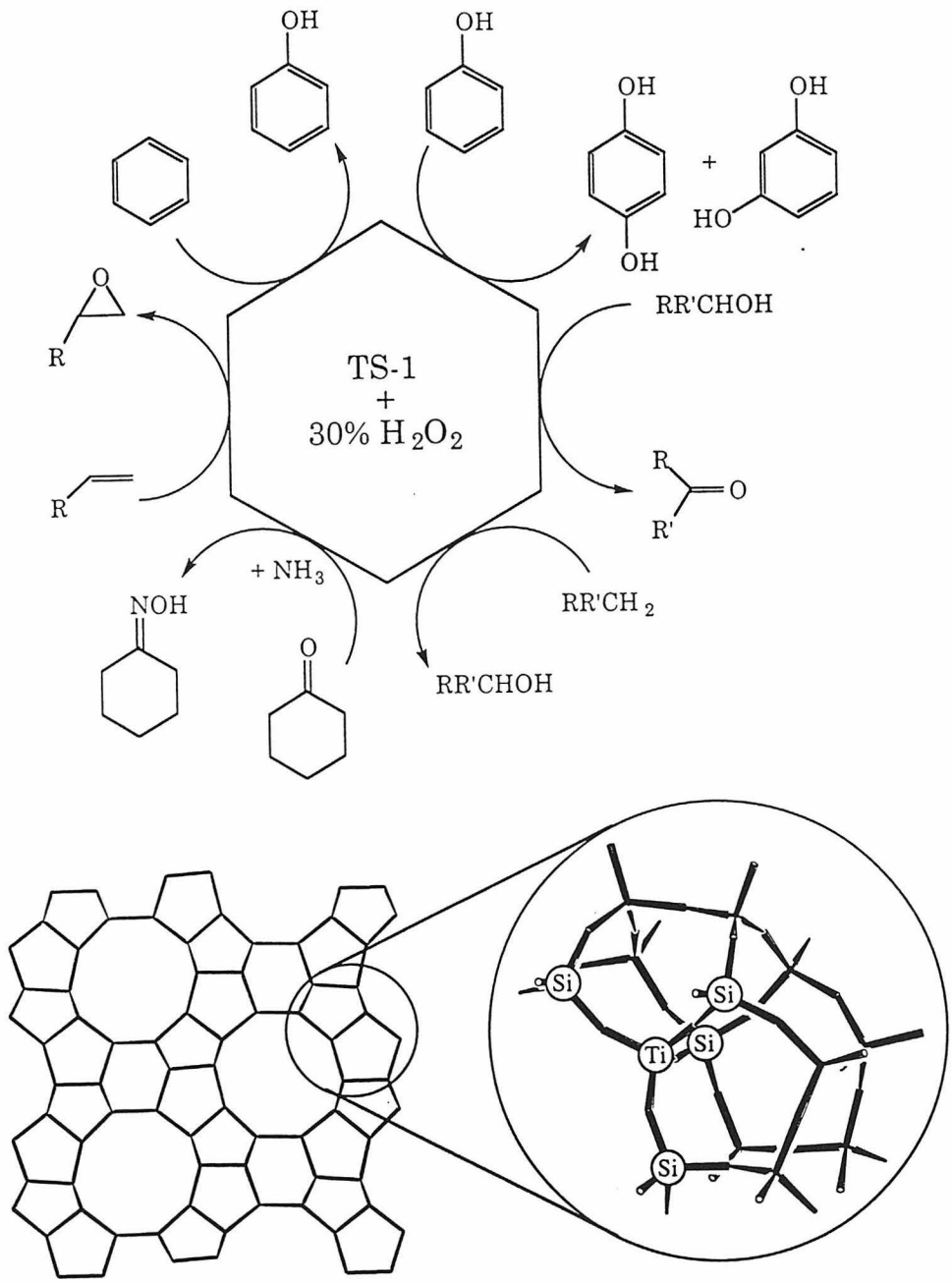


**Figure 1.5**. Examples of the oxidation reactions that can be carried out over TS-1 (Ti-ZSM-5).

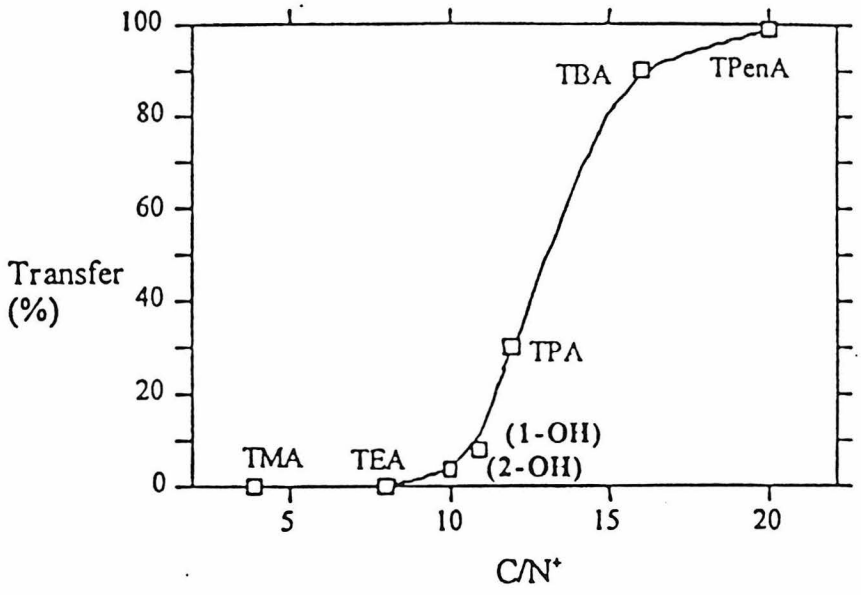


**Figure 1.6.** Partioning of quaternized amines between water and chloroform ( TMA-tetramethylammonium, TEA-tetraethylammonium, 2-OH-diethanoldipropylammonium, 1-OH ethanoltripropylammonium, TPA-tetrapropylammonium, TBA tetrabutylammounium, TPenA Tetrapenylammonium).

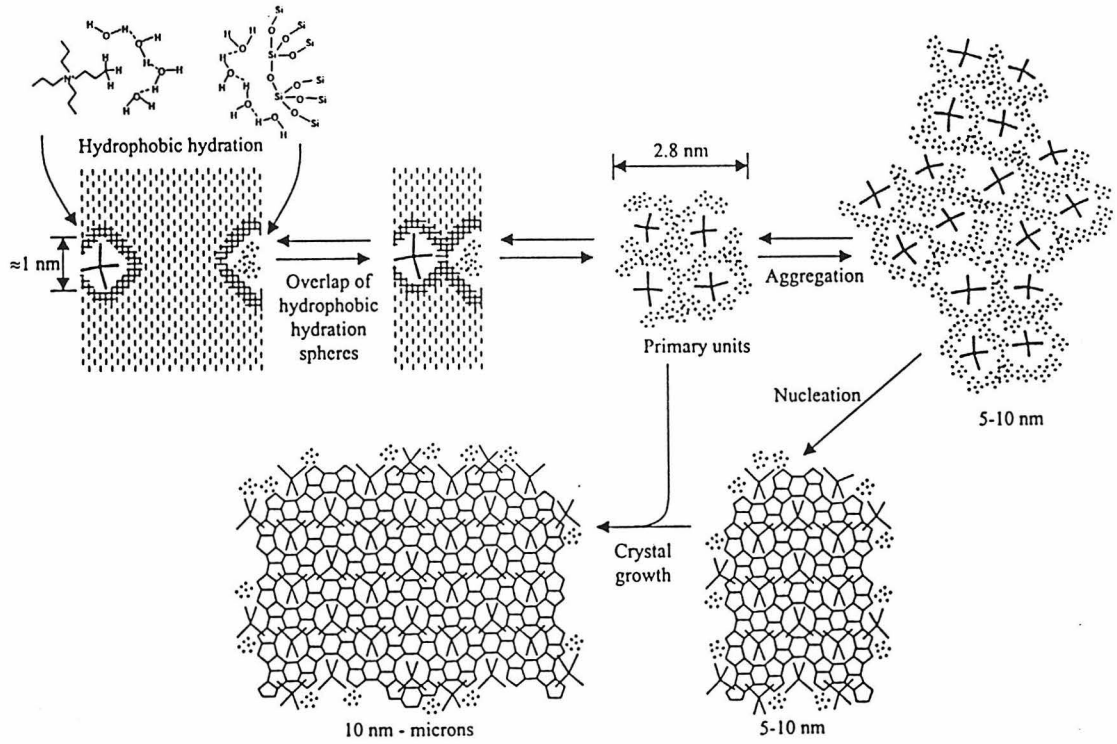


**Figure 1.7.** Zeolite nucleation and crystallization model in which the organic molecules hydrophobic hydration sphere of partially ordered water is replaced by silica. The silica/organic composites form primary particles that are unique for the particular zeolite phase. The primary particles aggregate into 10 nm particles, and a portion of the 10nm particles can become viable nuclei for crystal growth.

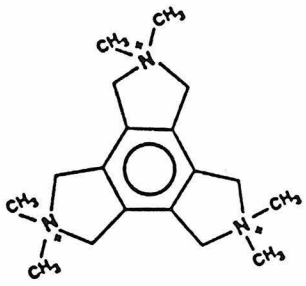

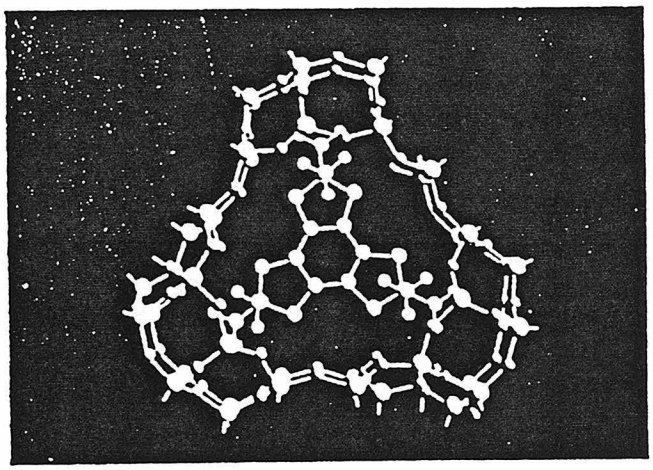

**Figure 1.8.** Tri-quat that forms ZSM-18 (MEI) together with the results of molecular modeling of the triquat in the ZSM-18 pores showing that the organic amine templates the framework and has restricted motion within the pore that possess similar symmetry to the organic.

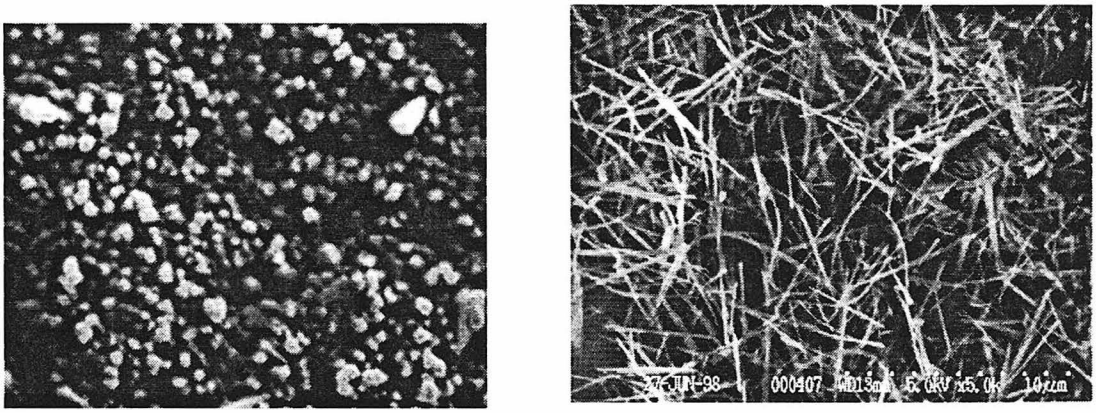


**Figure 1.9** Scanning Electron Micrographs (SEMs) of MFI (left) and SSZ-48 (right)

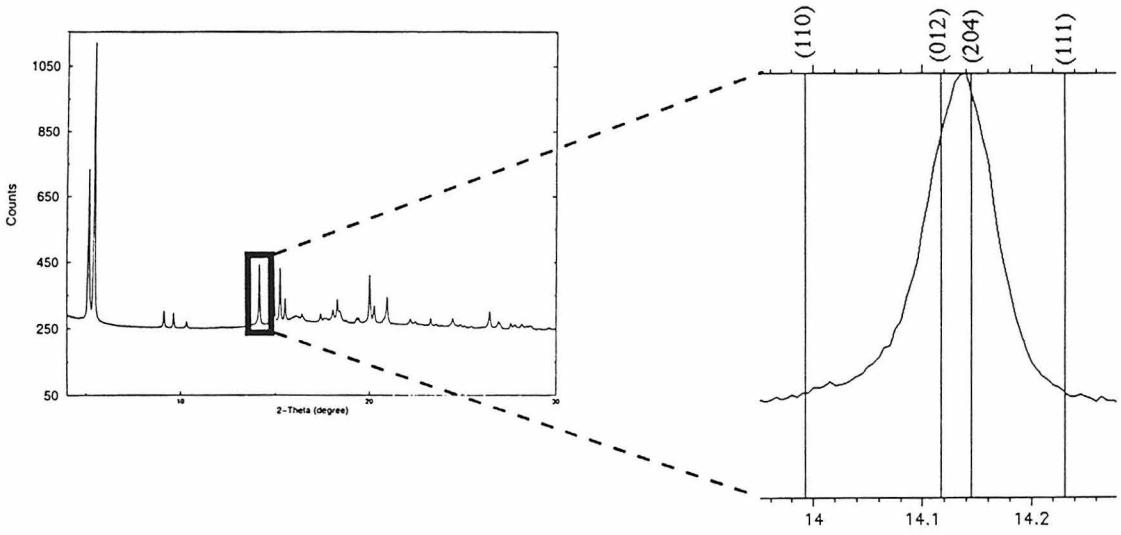


**Figure 1.10.** X-ray powder pattern of CIT-5 (CFI) showing the overlapping reflections in the indexation.

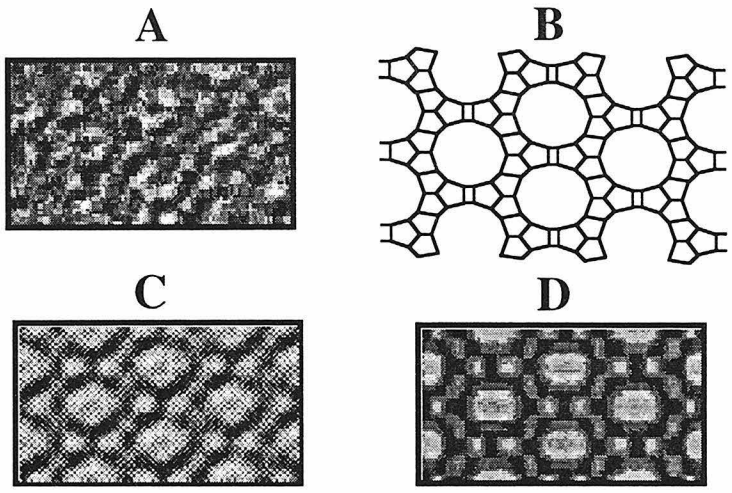


**Figure 1.11.** High Resolution Transmission Electron Micrographs of CIT-5 (a) experimental, (b) framework topology of CFI, (c) processed experimental image (d) simulated HRTEM

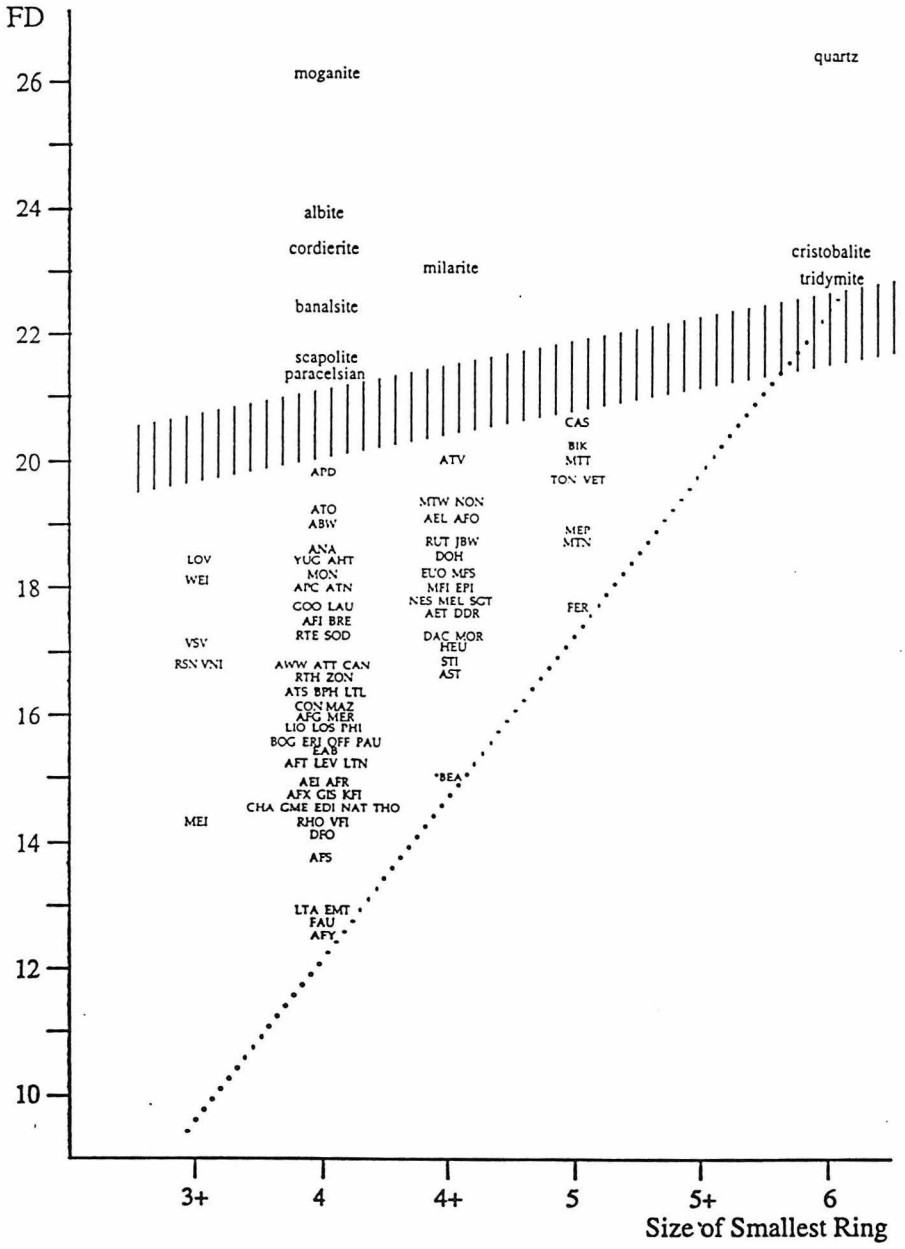


**Figure 1.12.** Brunner-Meier Correlation illustrating the relationship between the framework density and the smallest ring size in the material.

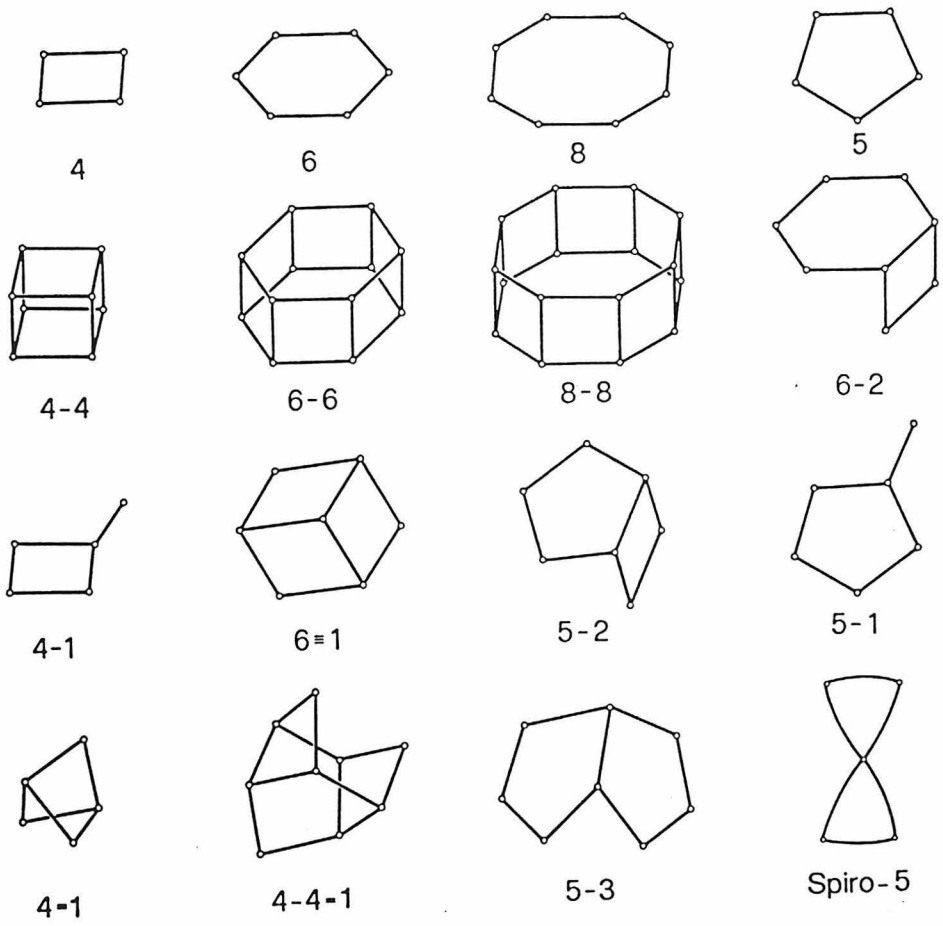


**Figure 1.13.** Examples of the Basic Building Units that can be connected to compose the zeolite structures.

# CHAPTER TWO

# Zeolite Structure Solution Model Building : CIT-5

Reprinted with permission from:

[M Yoshikawa, P. Wagner, M. Lovallo, K. Truji, T. Takewaki, C. Y. Chen, L. Beck, C. Jones, M. Tsapatsis, S. I. Zones, M. E. Davis "Synthesis, Characterization, and Structure Solution of CIT-5, a New, High-Silica, Extra-Large-Pore Molecular Sieve"; *J Phys. Chem. B*, **1998**, 102, 7139-7147]

Abstract

The synthesis, structure solution and characterization of the high-silica molecular sieve, CIT-5 (California Institute of Technology Number 5), is described. CIT-5 is synthesized at hydrothermal conditions in the presence of N(16) methylsparteinium and preferrably lithium cations. The structural solution of CIT-5 shows that it contains one-dimensional pores circumscribed by 14 tetrahedral-atoms (14 MR). Rietveld refinement of the synchrotron X-ray powder data gives a symmetry and space group assignment for the structure of $Pmn2_1$ (No. 31) with refined unit cell parameters of a=13.6738(8) Å, b=5.0216(3) Å and c=25.4883(7) Å (V=1750.1 $Å^3$). Electron diffraction (ED) and transmission electron microscopy (TEM) confirm the space group and the topology of the structure viewed along the [010] direction. Solid-state $^{29}Si$ NMR spectroscopy results are consistent with the space group assignment. The thermal/hydrothermal stability of CIT-5 compares well to that of other large and extra-large pore, high-silica molecular sieves. The acid form of CIT-5 is able to perform hydrocarbon reactions such as cracking and alkylation and shows behaviors that are different from other zeolites.

Introduction

Molecular sieves with 12 tetrahedral atoms (T-atoms) circumscribing the pores have been denoted as large-pore materials and have pore diameters of approximately 6-8 Å. Commercially useful zeolites such as NaY, L and beta are large pore materials. Pore systems that contain rings circumscribed by more than 12 -T atoms are classified as extra-large pores[1]. For many years, extra-large pore materials have been aggressively pursued both in industry and in academia[2-8]. The demand for these materials is led by a desire to perform shape-selective adsorption and catalysis on molecules that are greater than 8 Å in size. Provided these extra-large pore

materials can retain their pore structures under the thermal or hydrothermal conditions required, they should find applications as catalysts in the petrochemical industry and show potential for use in the fine chemicals and pharmaceuticals industries as well.

The first extra-large pore material, VPI-5[9] (an aluminophosphate material), was synthesized in 1987, and since that time numerous other phosphate-based extra-large pore materials have been prepared[3,10-14] . These phosphate-based materials suffer from poor thermal and hydrothermal stability that limits their usefulness.

Recently, the high-silica molecular sieve, UTD-1, has been characterized in detail and was shown to possess large, one-dimensional pores[15,16]. UTD-1 has the high thermal and hydrothermal stability characteristics of other high-silica molecular sieves and is the first high-silica molecular sieve to contain pores circumscribed by 14 tetrahedral atoms (14MR). The synthesis of UTD-1 requires an organometallic structure directing agent that can only be removed from the pores through calcination and acid treatment. Additionally, aluminum framework substitution (needed for acid catalysis) requires post-synthetic treatments.

Here, we report on the syntheses, characterization and structural solution of CIT-5, a new, high-silica molecular sieve with 14-ring pores that is synthesized using an organic structure directing agent. A preliminary report on the topology of CIT-5 has appeared and here we provide the complete structure solution[17]. CIT-5 and UTD-1 are the only high-silica molecular sieves to contain these extra-large pores. The high thermal and hydrothermal stabilities of UTD-1 and CIT-5 confirm that extra-large pore materials can have the stability required for industrial use. The direct incorporation of heteroatom substitutes such as aluminum into the framework of CIT-5 and the ease of removal of the structure directing agent through calcination make this material an appealing catalyst for large molecules.

Experimental Section

Synthesis

CIT-5 was synthesized at hydrothermal conditions within a temperature range of 423 K to 448 K. The syntheses were carried out in both sealed quartz tubes (75 mm x 15 mm I.D.) and in Teflon-lined Parr reaction vessels. CIT-5 can be prepared from the following composition:

$$1\ SiO_2 : 0.1\ MOH : 0.2\ MeSPAOH : x\ W : 40\ H_2O$$

where W can include the following: $Ga(NO_3)_3$ (Aldrich), $H_3BO_3$ (J.T. Baker) or $Al(NO_3)_3$ (J.T. Baker) (x can be varied from 0-0.02) and MOH can be either LiOH (Fisher) alone, or a mixture of LiOH together with either NaOH (Aldrich) or KOH (Aldrich). As discussed below, CIT-5 can be formed in the absence of $Li^+$ cations if the alkali metal cation ($K^+$ or $Na^+$) is present in very low concentration ( $[MOH]/[SiO_2]$ less than 0.05) when the total $[OH^-]/[SiO_2]$ ratio is held constant at 0.3. The synthesis of the organic structure directing agent, N(16) methylsparteinium hydroxide (**I**) (MeSPAOH), has been previously described[18].

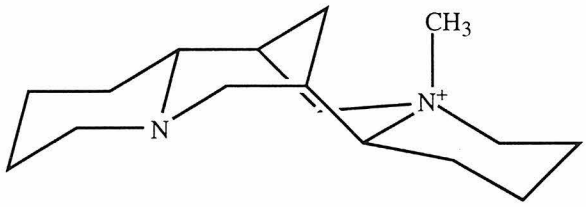


**I**

In a typical synthesis preparation of pure-silica CIT-5, 0.019g LiOH is added to a solution of 4.21g of distilled, deionized water and 0.85g of a 50.0 wt % solution of N(16) methylsparteinium hydroxide. 1.60g of the colloidal silica source (HS-30 DuPont) is added and the mixture is stirred for 30 min. The resulting synthesis

mixture is charged into quartz tubes that are heat sealed and placed in a convection oven at 175°C for 3-7 days. The recovered solid is washed with distilled, deionized water, and allowed to air dry.

Analytical

*X-ray Diffraction.* Synchrotron powder X-ray diffraction (SPXRD) patterns were collected on the X7A synchrotron beam line at Brookhaven National Laboratory. The CIT-5 sample was prepared for data collection by first calcining the material at 923 K (heating from room temperature at 5 K/min). The calcined sample was then packed into a 1 mm glass capillary and the synchrotron data were collected at ambient conditions with a step size of 0.005° from 4° to 50° 2-θ at a wavelength of 1.14798 Å. Powder X-ray diffraction patterns were also obtained on a Scintag XDS 2000 diffractometer using $CuK_\alpha$ radiation ( $\lambda$ = 1.54184 Å) with a liquid-nitrogen cooled solid-state germanium detector in a Bragg-Brentano configuration. The diffraction data were collected in continuous scanning mode over the range $2° < 2\text{-}\theta < 51°$ with a scanning rate of 0.2°/sec. National Institute of Standards and Technology Standard Reference Material 675 (flourophologopite mica) was used as the external standard.

The thermal and hydrothermal stability of CIT-5 were studied by *in situ*, temperature programmed powder X-ray diffraction. The samples were mounted as thin films on a platinum-rhodium alloy heater filament inside an Edmund Buhler high-temperature X-ray diffraction chamber. The sample thickness of the calcined CIT-5 powder on the filament varied from 0.5 mm to 1 mm. The chamber was evacuated and refilled with the flow gas and a steady flow of 0.5 l/min was then

maintained during data collection. The flow gas for the thermal stability studies was dry nitrogen, while dry nitrogen bubbled through distilled water held at room temperature was used as the flow gas for the hydrothermal stability studies. The samples were heated at a rate of 10 K/min and held at the designated temperature for 15 minutes prior to data collection. The X-ray diffraction scans were collected as continuous scans from 2-51° 2-θ at a scan rate of 5°/minute .

*Physisorption studies.* Argon physisorption measurements were carried out on a Coulter Omnisorp 100CX adsorption instrument . Argon adsorption isotherms were measured at 87 K by both static and continuous flow techniques. Prior to the adsorption experiments the calcined samples were degassed under vacuum ($<10^{-6}$ Torr) at 573 K for two hours. Approximately 1000 data points were obtained from the continuous flow experiments with argon pressures ranging between $10^{-6}$ Torr and 550 Torr. Sample sizes were ~100 mg and the argon flow rate was low enough to require between one and two hours to admit enough argon to fill the sample micropores. The equilibration times for the static adsorption experiments were ten minutes for each data point. Doses were small enough so that between five and ten hours were required to admit enough argon to fill the micropores. Micropore volumes and external areas were estimated from alpha-plot analyses of the adsorption isotherms, using alpha values obtained from a silica standard (CPG-75). The adsorption capacities of zeolites for vapor phase hydrocarbons were measured at room temperature using a Cahn C-2000 balance coupled with a computer via an ATI-Cahn digital interface. The adsorbates studied were n-hexane, 2,2-dimethylbutane, cyclohexane, and 1,3,5-triisopropylbenzene. The vapor of the adsorbate was delivered from the liquid phase. The relative vapor pressure $P/P_o$ was maintained at ~0.3 by controlling the temperature of the liquid adsorbate using a

cooling circulator. Prior to the adsorption experiments, the calcined zeolites were dehydrated at 623 K under a vacuum of $10^{-3}$ Torr for 5 h. The adsorption capacities are reported in milliliters of liquid per gram of dry zeolite, assuming bulk liquid density for the adsorbate in the micropores.

*Catalytic Studies.* Three catalytic test reactions are reported using the acid form of CIT-5: cracking of C6 isomers, m-xylene isomerization, and hydrocracking of n-hexadecane. The CIT-5 material was synthesized as previously described, with the exception that highly dealuminated Y zeolite (TOSOH HUA 390) was used as the silica source[19]. The syntheses were carried out in Teflon-lined Parr reactors heated to 433 K while rotating, for a period of between 6 and 10 days.

The active CIT-5 catalyst was prepared by calcining the as-synthesized CIT-5 to 873 K in air followed by ion-exchanging the calcined material with ammonium nitrate. The ion-exchange was carried out by heating 1 gram of the calcined zeolite with 1 gram of ammonium nitrate in 50 ml of water at 363 K for 2 hours, followed by filtration, washing with water, and finally air-dried The ammonium-exchanged zeolite was then packed into the catalytic reactor and converted to the acid form by heating to 813 K *in situ.* The acid form of CIT-5 was used for the cracking of C6 isomers and for the isomerization of m-xylene. The test reaction involving the hydrocracking of n-hexadecane (a model compound), utilized an acid/palladium form of the zeolite (as described below).

The cracking of C6 isomers was carried out as follows: 500 mg of ammonium-exchanged CIT-5 (20-40 mesh after pelleting at 3kpsi and breaking the pellet) was calcined to 813 K for 4 hours and cooled under a flow of nitrogen. The catalyst was then placed in a 3/8 inch stainless steel reactor with a bed of alundum packed on either side of the catalyst. Helium was passed through the reactor at 10 cc/min while the reactor tube is heated by a Lindburg furnace. At a reactor tube temperature of

645 K a 50/50 (w/w) feed of n-hexane and 3-methylpentane was introduced by a downflow (controlled using a Brownlee pump) of 8 μL/min. On-line sampling via a Valco, 6-way valve was started after 10 minutes of feed delivery. The data were collected on a Hewlett-Packard 5880 gas chromatograph with product peaks assigned using standards.

The m-xylene isomerization test reactions were conducted using two CIT-5 samples as catalysts. Sample A had a silica to alumina ratio (SAR) of 200 and sample B a silica to galia ratio (SGR) of 100. Sample A was syntheszied using a dealuminated Y zeolite as the silicon source, while samples B was synthesized using colloidal silica as the silicon source. After conversion of the CIT-5 material to the acid form (mesh size 35-70), between 100 and 400 mg of the catalyst were added to a downflow reactor. Under a helium flow of 50ml/min the following temperature program was carried out: the reactor is heated to 448 K over 2 hours and is held at this temperature for an additional 2 hours, the temperature was then increased from 448 K to 623 K over 1.5 hours and held at 623 K for 3 hours, finally, the temperature of the reactor is reduced to 590 K over 25 minutes. Once the helium flow rate had been reduced to 20ml/min, the feed was introduced by passing the helium flow gas through a saturator with m-xylene at 283 K. The products were analyzed on-line as previously described.

The catalyst used in the hydrocracking experiments was prepared by ion-exchanging palladium cations into the ammonium-exchanged material. Palladium tetraamine dinitrate was dissolved in a solution containing 2 ml of 0.156 N $NH_4OH$ in 9 ml $H_2O$ (the quantity of palladium tetraamine dinitrate dissolved was such that if all the palladium were to exchange into the zeolite there would be 0.5 wt % Pd in the catalyst). 990 mg of the zeolite was introduced into the solution which was then

aged statically at room temperature for 3 days. The zeolite was filtered, washed with 200-300 ml of water and then calcined to 755 K in air using the following program: the catalyst was heated to 393 K and held at this temperature for 2 hours, the temperature was then ramped to 755 K at 1 K/min and held at 755 K for three hours. The material is then pelleted, broken and meshed to 20-40 and jacketed by quartz chips of the same mesh size. The packed zeolite catalyst was dried *in-situ* , and the reactor temperature was reduced to 588 K. The inert carrier gas was replaced with a hydrogen atmosphere at 1200 psi. The n-hexadecane was introduced at a flow rate of 1μl/min. The temperature of the catalyst was gradually increased to promote a higher conversion of the feed. After 167 hours on-stream at 622 K, a 96% conversion of n-hexadecane to isomers and lighter products was achieved.

*NMR Studies.* Solid-state NMR spectra were collected on a Bruker AM 300 spectrometer. Samples were packed into 7 mm or 4 mm $ZrO_2$ rotors and spun in air. $^{29}Si$ (59.63 MHz) NMR spectra were obtained using magic angle spinning (MAS) at spinning rates of 3-4 kHz, pulse widths of 6 ms, and recycle delays of 30-60 seconds. Tetrakis-(trimethylsilyl)silane was used as the external reference material for $^{29}Si$ and $^{13}C$ NMR chemical shift determination. All chemical shifts are reported in ppm relative to TMS. $^{27}Al$ NMR spectra were recorded at a frequency of 78.2 MHz on samples packed into a 4 mm $ZrO_2$ rotor spinning at 8-9 kHz. A pulse width of 4 ms corresponding to a flip angle of $\pi/2$ along with a recycle delay of 1 second were used. $^{27}Al$ NMR chemical shifts are referenced to a 1.0 M $Al(NO_3)_3$ solution ( = 0.00 ppm), and are not corrected for second-order quadrupolar effects. $^{13}C$ (75.45 MHz) NMR spectra were measured using cross -polarization with a 1 H-90° pulse of 6.5 ms with a recycle delay of 1 second. $^{13}C$ NMR chemical shifts are referenced to adamantane (downfield resonance at 38.4 relative to TMS).

Spectral deconvolution and simulation were performed using both the Bruker Linesim and the MacFID software packages.

*TEM Studies.* Samples for transmission electron microscopy (TEM) were prepared both by microtomy and by dispersion. The samples prepared by dispersion were first crushed and then sonicated in ethanol. A drop of this dispersion was transferred to a carbon coated Cu grid and allowed to dry. The samples prepared by microtomy were embedded in an epoxy (LR White) which was subsequently cured at 363 K for two hours. Slices from the hardened epoxy sample were prepared using a diamond knife mounted on an ultra-microtome. The samples were dried in a desiccator over night prior to mounting in the TEM specimen holder. The TEM, ED and HREM images were taken on a JEOL 2000 FX operating at 200 kV, a JEOL 100CX operating at 100 kV, and a Phillips 430 operating at 200 kV respectively. Image analysis was performed using the "Image" software for Macintosh.

*Additional characterization studies.* Scanning electron micrographs were collected on a Camscan Series 2-LV electron microscope operating at an acceleration voltage of 15 kV. A DuPont 951 thermogravimetric analyzer was used to carry out the thermogravimetric analysis using a constant heating rate of 5 K/min. The elemental analyses were performed by Galbraith Laboratories (Knoxville, TN, USA).

## Results and Discussion

### Synthesis

Pure-silica CIT-5 is formed from the following synthesis mixture (mole ratio):

$$1\ SiO_2 : 0.1\ LiOH : 0.2\ MeSPAOH : 40\ H_2O$$

at a temperature of 448 K upon heating for 5 days. The optimal synthesis conditions include $Li^+$ cations ([LiOH]/[ $SiO_2$] = 0.1), however, ratios of $Li^+$ /$M^+$ (where $M^+$ can be either $Na^+$ or $K^+$) as low as 3/1 do not hinder the formation of CIT-5 (Table 1). As the $Li^+/M^+$ ratio is decreased to 1/1, CIT-5 is not formed and the synthesis results in the production of a previously reported, high-silica phase, SSZ-24[18,20,21] (International Zeolite Association code: AFI)[22]. CIT-5 can be formed without $Li^+$ present in the synthesis mixture at much longer crystallization times (>20 days), provided an alkali cation ($K^+$ or $Na^+$) is present in low concentrations ([MOH]/[$SiO_2$] ratios less than 0.05) and the ratio of [$OH^-$]/ [$SiO_2$] is held constant at 0.3 (synthesis results are summarized in Table 1). As the concentration of $Na^+$ is increased at constant [$OH^-$] ([NaOH]/[$SiO_2$] ratio increased from 0.05 to 0.1), SSZ-24 is formed to the exclusion of CIT-5.

These synthesis results indicate that the organic methyl spartienium cation weakly structure directs CIT-5. The presence of $Li^+$ cations serves to accelerate the crystallization times, while the presence of other alkali metal cations ($Na^+$ or $K^+$ ) at low concentrations also weakly assist in the crystallization of CIT-5. At higher concentrations, the presence of the $Na^+$ cations dominate the structure direction towards SSZ-24, presumably by affecting the silica dissolution kinetics or stabilizing species in solution prior to nucleation leading to the stabilization of SSZ-24 growth units. The organic methyl sparteinium cations may then serve to further stabilize the forming SSZ-24 structure by filling the pore system.

CIT-5 has also been synthesized in the presence of various atoms that can substitute for silicon, e.g., gallium, boron, and aluminum. The elemental analyses results for the aluminum containing CIT-5 (Al-CIT-5), indicate a silicon to aluminum ratio of 95. The chemical shift of the $^{27}Al$ resonance in the $^{27}Al$ MAS NMR spectrum from the as-synthesized Al-CIT-5 and the catalytic data for the Al-

CIT-5 material both confirm the presence of tetrahedrally coordinated aluminum and the Bronsted acid site formed from the framework aluminum (both results will be discussed in greater detail below).

Scanning electron micrographs (SEMs) show the CIT-5 crystallites to have a thin flat plate morphology (Fig. 1). TEM/ED analysis of the flat plate crystals reveal the (301) lattice fringes (Fig. 2) running along the long axis of the crystals and indicates that the b-axis (parallel to the channel direction) coincides with the long axis of the crystals.

Structure Solution of CIT-5

Synchrotron powder X-ray data (SPXRD) were collected from a sample of the calcined pure-silica CIT-5. Indexation of the SPXRD revealed an orthorhombic crystal class for the pure-silica CIT-5 sample with refined unit cell parameters of a=13.6738(8)Å, b=5.0216(3)Å and c=25.4883(7)Å (V=1750.1 $Å^3$)[23]. Initial analysis of the systematic absences in the SPXRD data indicate body centering consistent with 6 possible space groups.

The starting model for Rietveld refinement[24] was obtained by an iterative process of model building, distance least squares (DLS[25]) refinement of the atomic positions for the model, and comparison of the simulated powder X-ray pattern (CERIUS[26]) to the experimental pattern. The model with the closest match between the simulated X-ray powder pattern and the experimental XRD was found to have maximal topological symmetry of space group *Imma* (No. 74, standard setting), consistent with the systematic absences. However, initial Rietveld refinement of the starting model in this space group indicated an unacceptably large variation in the Si-O bond distances, and the O-Si-O bond angles[17].

In order to obtain a reasonable refinement of the SPXRD data it was necessary to reduce the topological symmetry of the space group within the orthorhombic crystal class. Distance least squares (DLS) refinement was used as a guide for indicating reasonable structural parameters for the starting model in a given space group. The DLS residual values for the six orthorhombic sub-groups of *Imma* (*Imm2, $I2_12_12_1$, Pmma, Pnma, Pnna and Pmna*) are summerized in Table 2. Although the space group *Pmna* gives the lowest DLS R-value (0.0050), it is high in comparison to other high-silica zeolite and indicates distortions in the structural parameters. As a result, the four orthorhombic sub-groups of *Pmna* were also evaluated using DLS as a guide. Of these sub-groups, space group $Pmn2_1$ was found to give the lowest R-value (0.0032).

Initial Rietveld refinements were carried out in the space group *Pmna* and in each of its four orthorhombic subgroups (*Pnc2, $P222_1$, Pma2*, and $Pmn2_1$). The atomic coordinates obtained from the DLS refinements were input as starting models for the Rietveld refinements. The initial Rietveld refinement procedures were carried out similarly for each of the space groups and the results are summarized in Table 2. Examination of the DLS R-values and the initial Rietveld $wR_p$, $R_p$ and reduced $\chi^2$ values led to the selection of space group $Pmn2_1$ for further refinements of the CIT-5 starting model.

The initial atomic positions for the Rietveld refinement of CIT-5 in space group $Pmn2_1$ (No. 31, standard setting) were obtained from the DLS-refinement. During the initial stages of the refinement, the scale factor and zero shift were refined along with a 15 parameter shifted Chebyshev function[24] for background subtraction. The lattice parameters and the peakshape function parameters[27] were then refined until convergence of the R-values was obtained. Soft geometric constraints for the Si-O

bond distances (d(Si-O)=1.610(10) Å) and interatomic O-O distances (d(O-O)=2.610(10) Å) were employed for the initial stages of the atomic position refinement. The weighting factor for the soft geometric constraints was gradually reduced. However, complete elimination of the soft constraints caused slight distortions in the Si-O bond distances and O-Si-O angles.

Table 3 provides a summary of the refinement details. All structural parameters are within reasonable ranges for silicate materials[28]. The average bond distance, d(Si-O), is 1.591 Å with a range of 1.555-1.641 Å. The average Si-O-Si angle is 149.4° with a maximum of 168.7° and a minimum of 140.6°, and the average O-Si-O angle is 109.4° with a maximum value of 113.8° and a minimum value of 104.2°. The low Rietveld residuals values ($wR_p$=7.09%, $R_p$=5.40%) indicate a close fit between the calculated and the experimental pattern (Fig 3). This solution has been accepted by the International Zeolite Association Structure Commision and the code CFI has been established for CIT-5.

The structure of CIT-5 viewed down the b-axis (Fig.4) is composed of one-dimensional, extra-large pores of nearly circular cross section (center of oxygen to center of oxygen distance 9.91Å x 9.87Å) circumscribed by 14 T-atoms. The asymmetric unit contains 10 T-atoms and 19 oxygen atoms resulting in a unit cell content of $[Si_{32}O_{64}]$, a framework density of 18.3 T-atoms/1000 $Å^3$ and a density of 1.821 $g/cm^3$. Table 4 contains the final atomic positional parameters obtained from the Rietveld refinement.

TEM/ED Studies

The simulated, experimental and image processed experimental high-resolution transmission electron micrographs (HRTEM) of CIT-5 viewed down the 14-MR pores are shown in Fig. 5. Comparison of the experimental image to the simulated

image confirms the proposed topology. The CIT-5 topology consists of zigzag ladders of 4-rings with pendant 5-rings. These units are interconnected through single zigzag chains to produce the pseudo-body centered structure. Electron diffraction patterns from the principle axes (Fig. 6) of pure-silica CIT-5 crystals contain considerable dynamical diffraction effects, however they show no signs of streaking indicating that the crystals are neither faulted or disordered.

NMR Studies

Comparison of the liquid $^{13}C$ NMR of N(16) methylsparteinium hydroxide with the MAS $^{13}C$ NMR of the as-synthesized CIT-5 (shown in Fig. 7) indicates that the structure directing agent occluded in the pores of CIT-5 is intact and has not decomposed under the synthesis conditions. The $^{29}Si$ MAS NMR spectrum of the as-made and calcined CIT-5 are shown in Figures 8a and b. The $^{29}Si$ NMR resonances from -107 to -115 ppm lie within the typical $Q^4$ range reported for other high-silica zeolites[29] . The NMR spectra of the calcined material has been deconvoluted into five peaks -107.8 (11.4%), -108.3 (25.7%), -112.9 (26.7%), -113.2 (25.9%), and -114.9 (10.3%) (Fig. 8c).

The basis set for the CIT-5 model in space group $Pmn2_1$ contains ten T-atoms. However, half of the T-atoms in the asymmetric unit are related by a pseudo 2-fold symmetry operation at ( 1/4,1/4,z ) that exists in the highest maximal topology. The similarities in the chemical environments of these T-atoms and the resolution limitations in the NMR intrumentation reasonably account for the observed deconvolution of the $^{29}Si$ MAS NMR of the calcined Si-CIT-5 sample. The site populations for the CIT-5 model in space group $Pmn2_1$ [Si2 + Si8 (4), Si1 + Si6 (8), Si3 + Si10 (8), Si5 + Si7 (8), Si4 + Si9 (4)] corresponds to a relative intensity ratio of 1:2:2:2:1 consistent with the observed deconvolution.

The $^{27}$Al MAS NMR spectrum of the as-synthesized Al-CIT-5 shows a single peak at 54 ppm. This peak is assigned to tetrahedrally coordinated aluminum and is a strong indication that the aluminum present in the material has been incorporated into the framework.

Adsorption and Thermal Gravimetric Studies

The adsorption capacities of various organic molecules in CIT-5 are reported in Table 5. The adsorption capacity of 1,3,5-triisopropylbenzene is consistent with the presence of extra-large, one-dimensional pores in CIT-5. The adsorption capacities of the other organic molecules listed in Table 5 for CIT-5 are similar to those reported for other large and extra-large pore zeolites,*e.g.*, UTD-1[16], and SSZ-24[19,20]. While the pore-mouth opening of CIT-5 and SSZ-24 are similar, the CIT-5 topology contains side pockets within the pore system (parallel to the c direction) that results in a maximum free pore diameter of 10.72 Å, and explains the differences in the uptake of large organic molecules such as 1,3,5-triisopropylbenzene (~8.5 Å kinetic diamter). The calculated geometric void volume for CIT-5 is 0.13 ml/g and compares well to the argon physisorption results reporting 0.11 ml/g. In addition, the thermal gravimetric analysis shows an 11.2 wt % loss from the SDA, N(16) methylsparteinium. This amount of organic corresponds to 1 SDA molecule per unit cell resulting in a pore volume of 0.13 ml/g, consistent with the argon physisorption and the calculated geometric void volume.

Thermal/Hydrothermal Stability

Thermal and hydrothermal studies were conducted using *in situ* X-ray diffraction to determine the crystallinity of pure-silica CIT-5 samples as a function of temperature. To investigate the thermal stability of CIT-5 a dry nitrogen atmosphere

was maintained inside the diffraction chamber while the sample temperature was increased from room temperature to 973 K in 100 K increments as previously described. A water/nitrogen atmosphere was maintained in the chamber during the hydrothermal stability studies.

The pure-silica CIT-5 samples are found to be both thermally and hydrothermally stable to over 923 K. These results are consistent with the thermal/hydrothermal stabilities of other large and extra-large pore high-silica zeolites and, together with the previously reported stability studies of UTD-1[16], indicate that extra-large pore materials can have the thermal and hydrothermal stability required for industrial application.

Catalytic Studies

Table 6 summarizes the results from the cracking of C6 isomers (n-hexane and 3-methylpentane). The values for the constraint index ( CI = log(fraction n-hexane remaining)/log(fraction 3-methylpentane remaining)[30] ) calculated for the C6 cracking over CIT-5 indicate that the cracking activity is consistent with the extra-large pores of CIT-5 (CI < 1, indicating no shape-selective preference for the linear hydrocarbon). Other large pore zeolites such as SSZ-24 (CI=0.35, 73% conversion), SSZ-31 (CI=1.20, 50% conversion), USY (CI=0.25, 50% conversion) and UTD-1 (CI=0.35, 78% conversion) show similar results. ZSM-5 (CI=5.0, 70% conversion) and ZSM-12 (CI=1.8, 20% conversion), which both have smaller pores, show some shape-selectivity (CI > 1). As can be observed from the data shown in Table 6, the catalyst does steadily deactivate. However, during the decline in activity the ratios reported are unaffected by the gradual coking. These results indicate that there exist acid sites within the material that are strong enough to crack alkanes and additionally, that there is no selective narrowing of the

pores or change in the reaction site as has been seen for zeolites beta and MCM-22[31].

The acidic forms of Al-substituted (sample A) and Ga-substituted (sample B) CIT-5 were used in m-xylene reactions. Both samples showed similar product selectivities and activities. The results described below are from sample B.

M-xylene isomerization selectivity of CIT-5 and other zeolites is shown Table 7. The large pore diameter of CIT-5 is evident by the low ratio of para to ortho xylene isomers (p/o ratio). The p/o ratio from CIT-5 is similar to the ratio of products from reaction over 1-dimensional large and extra-large pore zeolites SSZ-31, SSZ-24 and UTD-1. Zeolites with smaller pore sizes, such as ZSM-12 show a higher p/o ratio, indicating some shape-selectivity. As with C6 cracking, CIT-5 steadily deactivates when accomplishing the m-xylene conversions, but the p/o ratio does not change with time on stream. In contrast, the p/o ratio from reaction over UTD-1 steadily increases with time on stream, indicative of a selective narrowing of the pores by coking.

In addition to isomerization, m-xylene can disproportionate into trimethylbenzenes (TMB's) and toluene. The distribution of trimethylbenzene isomers reflects important structural features such as pore size and shape[32]. Larger pore zeolites tend to have a trimethylbenzene distribution that approaches equilibrium. However, structures with smaller sized void spaces tend to suppress the formation of the bulky 1,2,3 and 1,3,5 isomers. The data in Table 8 illustrate the TMB selectivity of CIT-5 and several other zeolites. Reaction of m-xylene over CIT-5 produces trimethylbenzenes with a low abundence of the bulky 1,3,5 isomer relative to equilibrium or reaction over the larger pore UTD-1. Similar results are observed for the reaction over SSZ-24 as might be expected.

For the experimental modeling of hydrocracking reactions, the n-hexadecane feed was carried out at 96% conversion (for comparison to other catalysts tested previously). Santilli and co-workers[33] described an *inverse* shape-selective phenomenon in which isomerized cracked products are preferred over straight chain hydrocarbons as the pore wall dimensions more closely match the kinetic diameters of the potential products. This behavior was shown to be particularly effective in the promotion of dimethylbutane products from n-hexadecane hydrocracking via the SSZ-24 catalyst with a pore diameter near 7.3 Å[33]. When comparing the ratio of the formed dimethylbutanes to n-hexane versus pore diameter, a bell-shaped curve is observed where the ratio is low for pore systems below 6 Å (the dimethylbutanes would be hindered from diffusing out of the constricted pores), higher values are achieved for 12-ring zeolites and then for larger pores the effect of the inverse shape-selectivity is lost and the values drop again for this ratio. This ratio for several zeolites and CIT-5 is presented in Table 9 along with the nominal pore size data. A particularly interesting case is SSZ-31[34] that has an elliptical, one-dimensional pore which reaches 8.8 Å in diameter across the major axis of the ellipse but is limited to 5.5 Å in diameter across the minor axis. In this case the smaller cross-section determines the product distribution. SAPO-11, another molecular sieve with elliptical pores and has the diameter across the major axis greater than 6Å also shows this restrictive behavior. Although the pore aperature is 7.3Å, CIT-5 does not give a ratio near the maximum of the bell-shaped curve as SSZ-24 does. Instead, the hydrocracking over CIT-5 yields a lower ratio, which can be attributed to small side pockets that give a maximum free pore diameter of 10.7Å. The reaction data when taken in total, show that CIT-5 provides for unique reaction behavior when compared to other zeolites. This is not unexpected from the fact that it contains a unique pore system.

## Conclusions

The structure of CIT-5, a new high-silica molecular sieve, has been determined and the material is shown to contain extra-large pores circumscribed by 14 T-atoms. Rietveld refinement of the synchrotron X-ray powder data gives the symmetry and space group assignment for the structure of $Pmn2_1$ (No. 31) with refined unit cell parameters of a=13.6738(8) Å, b=5.0216(3) Å and c=25.4883(7) Å (V=1750.1 $Å^3$). All Si-O-Si and O-Si-O bond angles and Si-O bond distances calculated from the final atomic coordinates are within reasonable ranges for silicate materials. TEM/ED indicates that the 1-dimensional pore material does not contain faulting defects and that the pores run along the long axis of the crystals. Both the adsorption (1,3,5 triisopropylbenzene uptake) and the catalytic results (p/o ratio from m-xylene isomerization and the dimethylbutane/n-hexane product ratio from the hydrocracking of n-hexadecane) support the structure assignment. CIT-5 is synthesized hydrothermally in the presence of the organic, N(16) methylsparteinium, and lithium cations. MAS $^{13}C$ NMR indicates the organic is intact in the pores of the as-synthesized material and has not degraded under synthesis conditions. Stability studies reveal that CIT-5 retains its pore structure under both high thermal and hydrothermal conditions. CIT-5 together with UTD-1 are the only extra-large pore, high-silica molecular sieves that have high thermal/hydrothermal stability.

## Acknowledgments

We gratefully acknowledge Dr. John Higgins of Air Products and Chemicals Inc, and Dr. D. E. Cox for their assistance in collecting the synchrotron powder XRD data. The data were collected at the X7A beamline at the National Synchrotron

Light Source at Brookhaven National Laboratory (Upton, NY), that is supported by the Department of Energy, Division of Material Science and Division of Chemical Sciences. Dr. Chuck Kibby of Chevron is thanked for the collection of argon isotherms, Dr. Ronald C. Medrud of Chevron is thanked for synchrotron powder XRD data collection, and Drs. Tom Harris and Bowman Lee also of Chevron are thanked for the experimental hydrocracking and cracking data. MT and ML acknowledge support from the David and Lucile Packard Foundation. PW thanks Air Products and Chemicals for financial support. Additional financial support for this work was provided by Chevron.

References

(1) Davis, M. E. *Chem. Eur. J.* **1997**, *3*, 1745-1750.

(2) Davis, M. E. *Chem. Ind. London* **1992**, *4*, 137.

(3) Estermann, M.; McCusker, L. B.; Baerlocher, Ch.; Merrouche, A.; Kessler, H. *Nature* **1991**, *352*, 320-323.

(4) Davis, M. E. *Nature* **1991,** *352*, 281.

(5) Davis, M. E. *Nature* **1989**, *337*, 117.

(6) Barrer, R. M.; Villiger, H. *Z. Kristallogr.* **1963**, *128*, 352.

(7) Smith, J. V.; Dytrych, W. J. *Nature* **1984**, *309*, 607.

(8) Brunner, G. O.; Meier, W. M. *Nature* **1989**, *337*, 147.

(9) Davis, M. E.; Saldarriaga, C.; Montes, C.; Garces, J.; Crowder, C. *Nature* **1988**, *331*, 698.

(10) Jones, R. H.; Thomas, J. M.; Chen, J. S.; Xu, R. R.; Hou, Q. S.; Li, S.G.; Ma, Z. *J. Sol. St. Chem.* **1993**, *102*, 202-208.

(11) Loiseau, T.; Ferrey, G. *J. Sol. St. Chem.* **1994**, *111*, 403-415.

(12) Loiseau, T.; Ferrey, G. *J. Mat. Chem.* **1996**, *6*, 1073-1074.

(13) Kahn, M. I.; Meyer, L. M.; Haushalter, R. C. *Chem. Mater.* **1996**, *8,* 43-53.

(14) Schindler, M.; Joswig, W.; Bauer, W. H. *Anorg. Allg. Chem.* **1997**, *623*, 45-54.

(15) Freyhardt, C. C.; Tsapatsis, M.; Lobo, R. F.; Balkus, K. J.; Davis, M. E. *Nature* **1996**, *381*, 295.

(16) Lobo, R. F.; Tsapatsis, M.; Freyhardt, C. C.; Khodabandeh, S.; Wagner, P.; Chen, C. Y.; Balkus K. J.; Zones, S.; Davis, M. E. *J. Am. Chem. Soc.* **1997**, *119* , 8474-8484.

(17) Wagner, P.; Yoshikawa, M.; Lovallo, M.; Tsuji, K.; Tsapatsis, M.; Davis, M. E. *Chem. Comm.* **1997**, 2179-2180.

(18) Lobo, R. F.; Davis, M. E. *Microporous Mater.* **1994**, *3*, 61.

(19) Zones, S. I.; Nakagawa, Y. US Patent 5,225,179; 1993.

(20) Bialek, R.; Meier, W.M.; Davis. M.E.; Annen, M. J. *Zeolites* **1991**, *11*, 438-442.

(21) Richardson, J. W.; Smith, J. V.; Han, S. X. *J. Chem. Soc., Faraday Trans.* **1990**, *86*, 2341.

(22) Meier, W. M.; Olson, D. H.; Baerlocher, Ch. *Atlas of Zeolite Structure Types*, 4th ed.; Elsevier; London, **1996**.

(23) Werner, P. E.; Erikson, L.; Westdahl, M. *J. Appl. Cryst.* **1985** , *18*, 367.

(24) Larson A. C.; Von Dreele, R. B. *Los Alamos Laboratory Report*, 1987, No. LA-UR-86-748.

(25) Baerlocher, Ch.; Hepp, A. ; Meier, W. M. *DLS-76: A Fortran Program for the Simulation of Crystal Structures by Geometric Refinement,* **1977**, Institute fur Kristallographie, ETH: Zurich, Switzerland.

(26) CERIUS Version 3.2, Molecular Simulations, Cambridge, UK, **1993**.

(27) Thompson, P.; Cox, D. E.; Hastings. J. B. *J. Appl. Cryst.* **1987**, *15*, 615-620.

(28) Lewis, J.; Freyhardt, C. F.; Davis, M.E. *J. Phys. Chem.* **1996**, *100*, 5045-5049.

(29) Englehardt, G.; Michel, D. *High-resolution solid-state NMR of silicates and zeolites*; Wiley: New York, 1987.

(30) van Bekkum, H.; Flanigen, E.M.; Jansen, J.C. *Introduntion to Zeolite Science and Practice*; Elsevier;Amsterdam, 1991.

(31) Yuen, L. T.; Geilfuss, J.; Zones, S. I. *Microporous Mater.* **1997**, *12*, 229.

(32) Martens, J. A.; Perez-Pariente, J.; Sastre, E.; Corma, A.; Jacobs, P. A.; *Applied Catalysis A.*, 45, **1988**, 85-101.

(33) Santilli, D. S.; Harris, T. V.; Zones, S. I. *Microporous Mater* . **1993**, *1*, 329-341.

(34) Lobo, R. F.; Tsapatsis, M.; Freyhardt, C. F.; Chan, I. Y.; Chen, C. Y.; Zones, S.I.; Davis, M. E. *J. Am. Chem. Soc.* **1997**, *119*, 3732-3744.

**Table 2.1.** Synthesis of CIT-5[a].

| $SiO_2$ | MOH | MeSPAOH | W | $H_2O$ | Temperature (°C) | Time (days) | Phase (Silicon/Y)[b] |
|---|---|---|---|---|---|---|---|
| 1 | 0.1 LiOH | 0.2 | – | 40 | 175 | 5 | CIT-5 |
| 1 | 0.05 KOH | 0.25 | – | 40 | 175 | 60 | CIT-5 + AFI |
| 1 | 0.05 NaOH | 0.25 | – | 40 | 175 | 18 | CIT-5 |
| 1 | 0.1 NaOH | 0.2 | – | 40 | 175 | 7 | AFI |
| 1 | 0.075 LiOH, 0.025 NaOH | 0.2 | 0.01 $H_3BO_3$ | 40 | 175 | 5 | CIT-5 |
| 1 | 0.050 LiOH, 0.050 NaOH | 0.2 | 0.01 $H_3BO_3$ | 40 | 175 | 5 | AFI |
| 1 | 0.075 LiOH, 0.025 KOH | 0.2 | 0.01 $H_3BO_3$ | 40 | 175 | 5 | CIT-5 |
| 1 | 0.1 LiOH | 0.2 | 0.01 $H_3BO_3$ | 40 | 175 | 7 | CIT-5 (63) |
| 1 | 0.1 LiOH | 0.2 | 0.01 $Al(NO_3)_3$ | 40 | 175 | 11 | CIT-5 (95) |
| 1 | 0.1 LiOH | 0.2 | 0.01 $Ga(NO_3)_3$ | 40 | 175 | 7 | CIT-5 (109) |

a) Values for reactants in table are given as mole ratios.

b) Values in parenthesis are the molar Si/Y ratios (Y: Ga,Al,B) measured by elemental analysis.

**Table 2.2.** CIT-5 Space Group Analysis.

| Space Group | DLS R-value* | Preliminary Rietveld Refinement | | |
|---|---|---|---|---|
| | | $wR_p$ | $R_p$ | reduced $\chi^2$ |
| *Imma* | 0.0171 | ----- | ----- | |
| Orthorhombic Sub-Groups of *Imma* | | | | |
| *Imm2* | 0.0150 | ----- | ----- | |
| $I2_12_12_1$ | 0.0088 | ----- | ----- | |
| *Pmma* | 0.0153 | ----- | ----- | |
| *Pnma* | 0.0096 | ----- | ----- | |
| *Pnna* | 0.0076 | ----- | ----- | |
| *Pmna* | 0.0050 | 0.1107 | 0.0853 | 91.23 |
| Orthorhombic Sub-Groups of *Pmna* | | | | |
| *Pnc2* | 0.0047 | 0.1040 | 0.0771 | 80.08 |
| $P222_1$ | 0.0049 | 0.1186 | 0.0859 | 102.90 |
| *Pma2* | 0.0036 | 0.1051 | 0.0784 | 80.95 |
| $Pmn2_1$ | 0.0032 | 0.1028 | 0.0762 | 77.33 |

* DLS refinements carried out using following orthorhombic unit cell parameters (Å) : 5.021, 13.697, 25.497.

**Table 2.3.** Crystallographic and Refinement Data.

| | |
|---|---|
| Space Group | $P\,m\,n\,2_1$ (No. 31) |
| *a* | 13.67388(40) Å |
| *b* | 5.02163(12) Å |
| *c* | 25.48837(95) Å |
| wavelength | 1.14798 Å |
| data collection temp. | 298 K |
| profile range | 4.0-50.0° |
| no. observables | 9200 |
| step scan increments | 0.005 ° |
| no. variables | 131 |
| no. reflections | 449 |
| wRp | 7.09 % |
| Rp | 5.40 % |
| ave. d(Si-O) | 1.591(3) Å |
| min | 1.555(0) Å |
| max | 1.641(0) Å |
| ave. Si-O-Si angle | 149.4(5)° |
| min | 140.6(0)° |
| max | 168.7(0)° |
| ave. O-Si-O angle | 109.4(5)° |
| min | 104.2(0)° |
| max | 113.8(0)° |

**Table 2.4.** Refined Atomic Positional Parameters (fractional coordinates) in Space Group $Pmn2_1$ (No. 31) and Isothermal Temperature Factors (esd in parentheses).

| Atom | a | b | c | $U_{iso}(Å^2)$ |
|---|---|---|---|---|
| Si1 | 0.1100(10) | 0.2980(4) | 0.0318(6) | 0.019(1) |
| Si2 | 0.000000(0) | 0.7300(5) | 0.2702(7) | 0.048(9) |
| Si3 | 0.2868(9) | 0.733(33) | 0.1883(5) | 0.010(3) |
| Si4 | 0.000000(0) | 0.2360(4) | 0.2055(6) | 0.041(2) |
| Si5 | 0.1956(20) | 0.250(4) | 0.1414(5) | 0.017(2) |
| Si6 | 0.3884(9) | 0.2082(34) | 0.4634(5) | 0.027(5) |
| Si7 | 0.3001(12) | 0.300(4) | 0.3523(6) | 0.034(8) |
| Si8 | 0.500000(0) | 0.764(4) | 0.2248(5) | 0.016(7) |
| Si9 | 0.500000(0) | 0.264(5) | 0.2912(7) | 0.009(6) |
| Si10 | 0.2064(12) | 0.789(4) | 0.3076(6) | 0.038(8) |
| O11 | 0.1258(22) | 0.091(32) | -0.0139(6) | 0.027(8) |
| O12 | 0.1834(7) | 0.242(4) | 0.0794(33) | -0.025(6) |
| O13 | 0.1391(20) | 0.5933(32) | 0.0092(7) | 0.013(5) |
| O14 | 0.000000(0) | 0.303(9) | 0.0518(10) | 0.041(9) |
| O15 | 0.000000(0) | 0.425(4) | 0.2541(7) | 0.039(5) |
| O16 | 0.0926(6) | 0.782(4) | 0.3075(7) | 0.049(7) |
| O17 | 0.000000(0) | -0.071(4) | 0.2216(7) | 0.005(5) |
| O18 | 0.2742(13) | 0.465(5) | 0.1581(8) | 0.029(2) |
| O19 | 0.4029(5) | 0.796(4) | 0.1906(6) | 0.003(5) |
| O20 | 0.2337(14) | -0.036(4) | 0.1584(8) | 0.008(4) |
| O21 | 0.2433(16) | 0.728(5) | 0.2476(5) | 0.023(6) |
| O22 | 0.9053(6) | 0.3024(34) | 0.1694(5) | 0.006(6) |
| O23 | 0.3164(13) | 0.238(5) | 0.4141(5) | 0.065(5) |
| O24 | 0.500000(0) | 0.241(8) | 0.4453(10) | 0.017(9) |
| O25 | 0.2333(14) | 0.083(4) | 0.3260(8) | 0.037(2) |
| O26 | 0.4043(6) | 0.303(5) | 0.3256(6) | 0.044(0) |
| O27 | 0.2529(15) | 0.584(4) | 0.3468(7) | 0.039(3) |
| O28 | 0.500000(0) | -0.037(5) | 0.2716(8) | 0.057(7) |
| O29 | 0.500000(0) | 0.464(4) | 0.2446(8) | 0.003(1) |

**Table 2.5.** Comparison of adsorption capacities for CIT-5 and other large and extra-large pore molecular sieves.

| Adsorbate | Kinetic Diameter (Å) | Adsorption Capacity (ml/g) | | |
|---|---|---|---|---|
| | | CIT-5 | SSZ-24[a] | UTD-1[a] |
| argon | 3.0 | 0.108 | 0.109 | 0.110 |
| n-hexane | 4.4 | 0.092 | 0.101 | 0.121 |
| cyclohexane | 6.0 | 0.090 | 0.114 | 0.111 |
| 2,2-dimethyl butane | 6.2 | 0.093 | 0.128 | 0.119 |
| 1,3,5-triisopropyl benzene | 8.5 | 0.041 | 0.011 | 0.111 |

a) Data from ref. 16

**Table 2.6.** Constraint Index conversion data (C6 cracking) for CIT-5 (SAR = 200) at 427°C.

| | Conversion After 10 minutes On-Stream | Converstion After 430 minutes On-Stream |
|---|---|---|
| Feed conversion | 38% | 19.7% |
| 3-methylpentane | 52% | 27% |
| n-hexane | 24.3% | 12.5% |
| Constraint Index | 0.38 | 0.42 |
| Product distribution: | | |
| C6 isomerization[a] | 10.1% | 12.9% |
| C5 minus cracking[b] | 84.1% | 83.3% |
| Aromatics[c] | 3.2% | 1.1% |
| Dehydrogenation[d] | 1.4% | 1.3% |

a) C6 products other than hexane and 3-methylpentane
b) C5 and lower hydrocarbons from cracking (paraffins and olefins)
c) e.g., benzene, toluene, etc.
d) C6 olefins

**Table 2.7.** Meta-Xylene Isomerization for CIT-5 (selectivities extrapolated to zero time on stream).

| Molecular Sieve | Pore Size (nm)* | Initial Para-Xylene/Ortho-Xylene Selectivity |
|---|---|---|
| CIT-5 | 0.73 | 0.60 |
| SSZ-24 | 0.73 | 0.77 |
| UTD-1 | 0.875 | 0.66 |
| SSZ-31 | 0.715 | 0.75 |
| ZSM-12 | 0.57 | 1.27 |
| USY | 0.74 + mesopores | 1.12 |
| ZSM-5 | 0.545 | 2.68 |

*Pore diameter of the largest pore. If pore is not circular, the average is used.

**Table 2.8.** Trimethylbenzene selectivities for CIT-5 and other zeolites.

| Zeolite | Trimethylbenzene isomer (%) | | |
|---|---|---|---|
| | 1,2,3 | 1,2,4 | 1,3,5 |
| CIT-5 | 8 | 83.5 | 8.5 |
| ZSM-12 | 0 | 100 | 0 |
| UTD-1 | 7 | 71 | 22 |
| USY | 6.5 | 66 | 27.5 |
| SSZ-24 | 9 | 83.5 | 7.5 |
| SSZ-31 | 7 | 76 | 17 |
| ZSM-5 | 0 | 100 | 0 |
| Equilibrium at 350°C | 8 | 68 | 24 |

**Table 2.9.** Hydrocracking of n-hexadecane. Comparison of dimethylbutanes to n-hexane product ratios with pore diameters.

| Molecular Sieve | Dimensionality | Diameter (Å) | dimethylbutane/n-hexane |
|---|---|---|---|
| ZSM-12 | 1 | 6.0 | 0.08 |
| SSZ-31 | 1 | 8.8 x 5.5 | 0.50 |
| SSZ-24 | 1 | 7.3 | 0.80 |
| CIT-5 | 1 | 7.3** | 0.33 |
| UTD-1 | 1 | 10.0 x 7.7 | 0.20 |
| LTL | 1 | 10* | 0.20 |
| FAU | 3 | 13* | 0.15 |

* Multidimensional channel system

**Small side pockets within pores give maximum free pore diameter of 10.7 Å

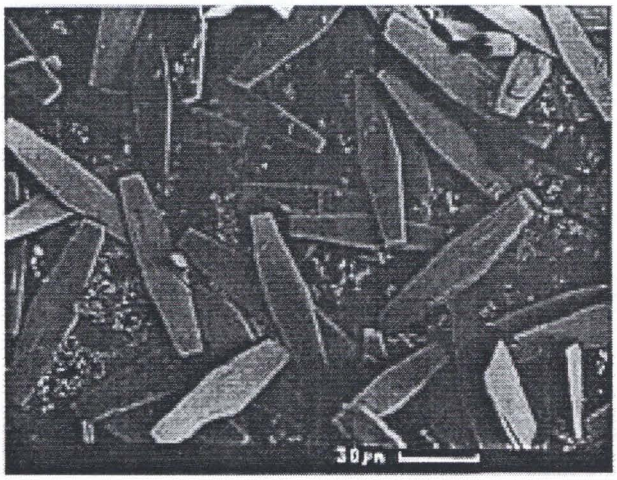


**Figure 2.1.** Scanning electron micrograph of CIT-5 crystallites.

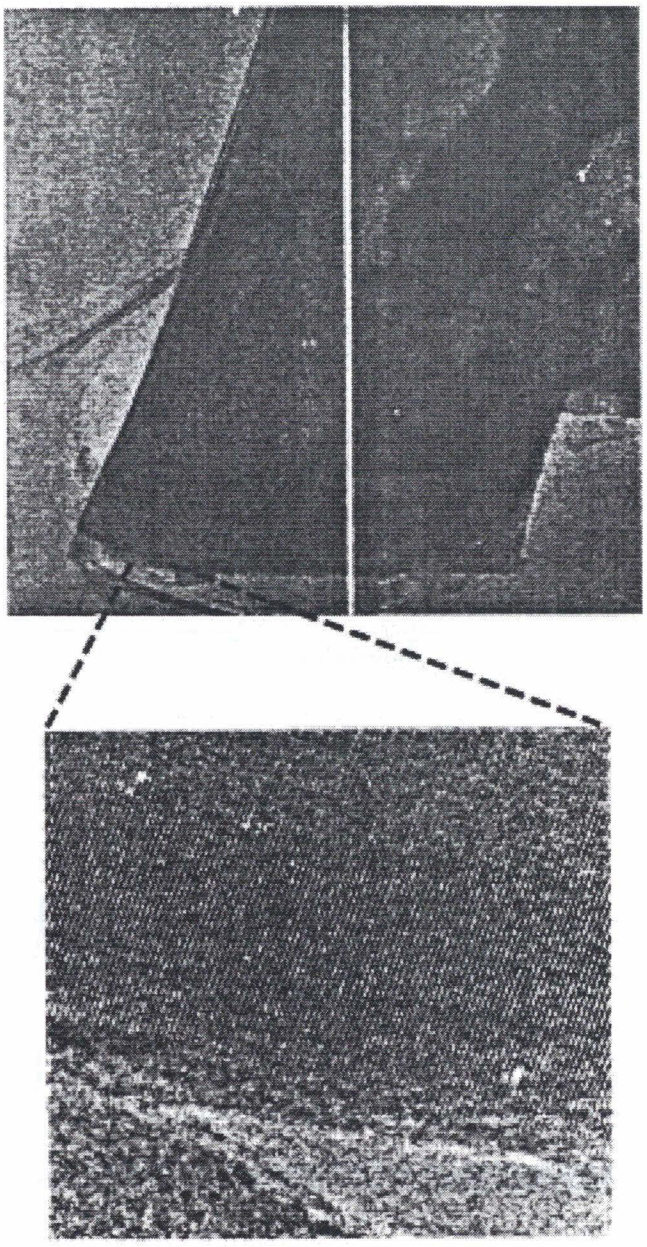

**Figure 2.2.** Transmission electron micrograph of pure-silica CIT-5 crystallite showing (301) lattice fringes indicting pore direction parallel to the long axis of the crystallite.

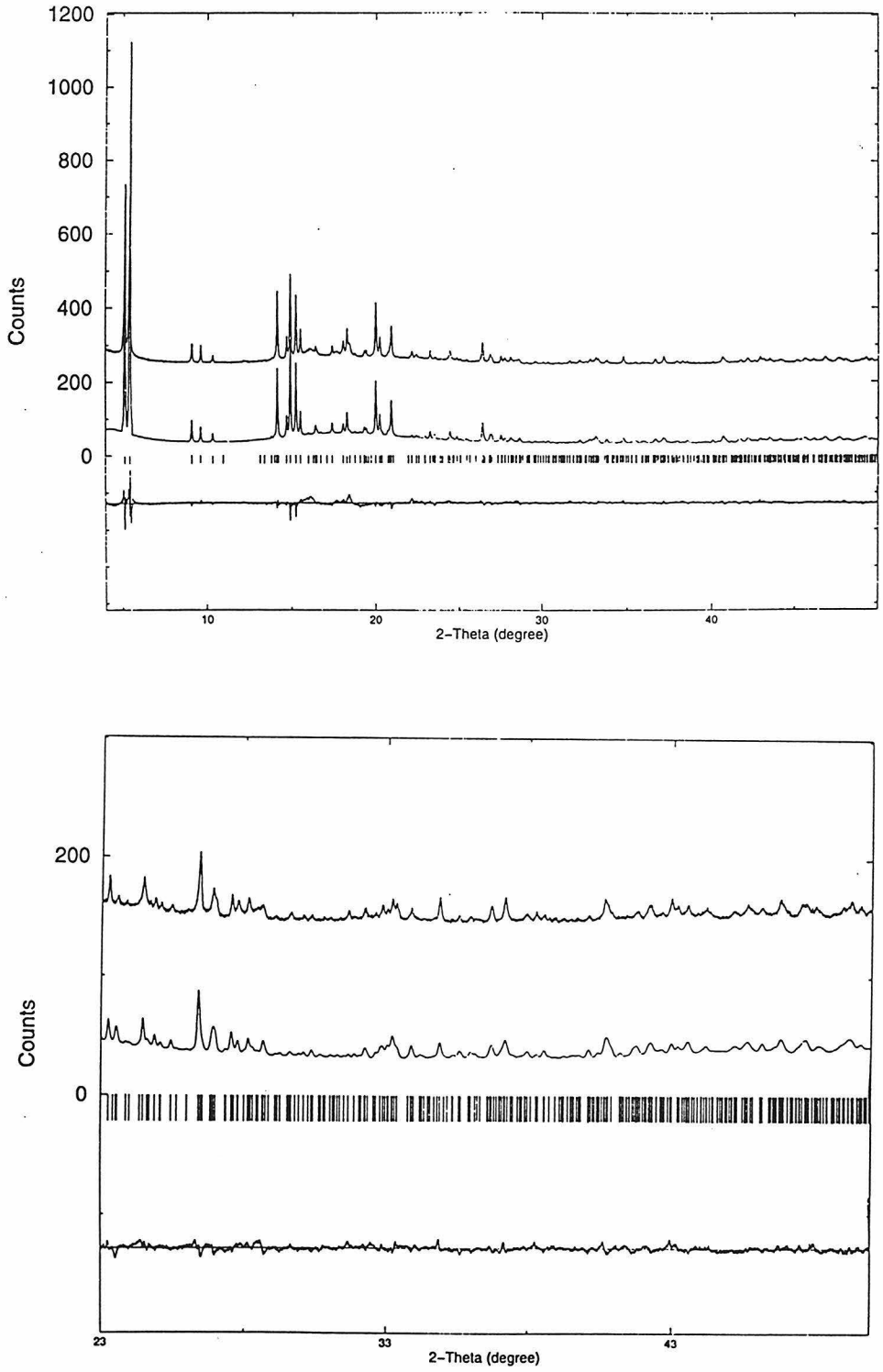


**Figure 2.3.** Comparison of experimental synchrotron pattern (upper) calculated (middle) and difference profile (lower) for the Rietveld refinement of CIT-5 ($\lambda$ = 1.147 98 Å).

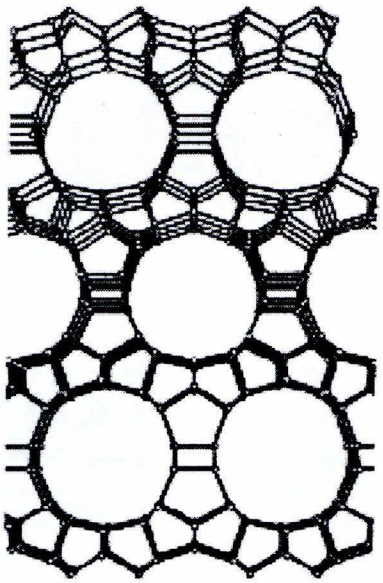

**Figure 2.4.** CIT-5 framework structure (bridging oxygen atoms omitted) viewed down 14 MR pores ([010] zone).

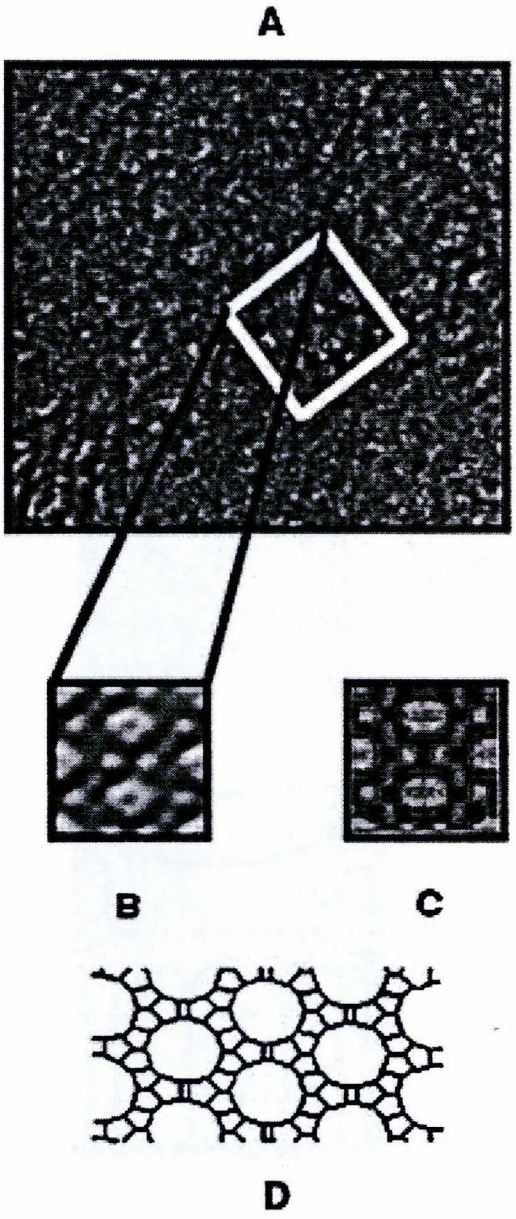


**Figure 2.5.** Transmission electron micrographs (TEMs) of CIT-5: (a) experimental image, (b) experimental averaged image, (c) simulated TEM image of CIT-5 topology, and (d) CIT-5 topology.

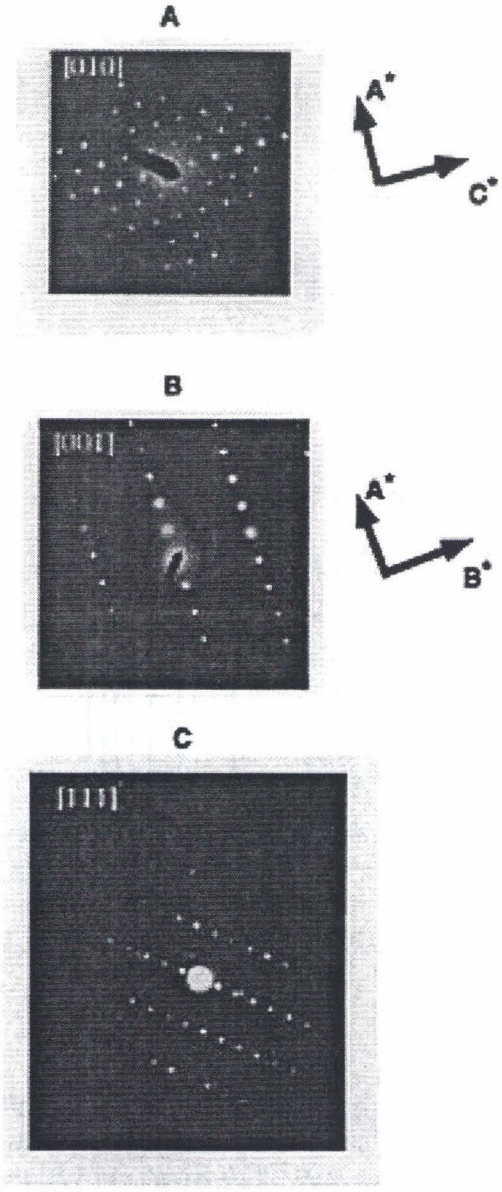


**Figure 2.6.** Electron diffraction patterns from pure-silica CIT-5: (a) [010], (b) [001], and (c) [111]. The reciprocal lattice vectors are shown for the principal zone axes [010] and [001].

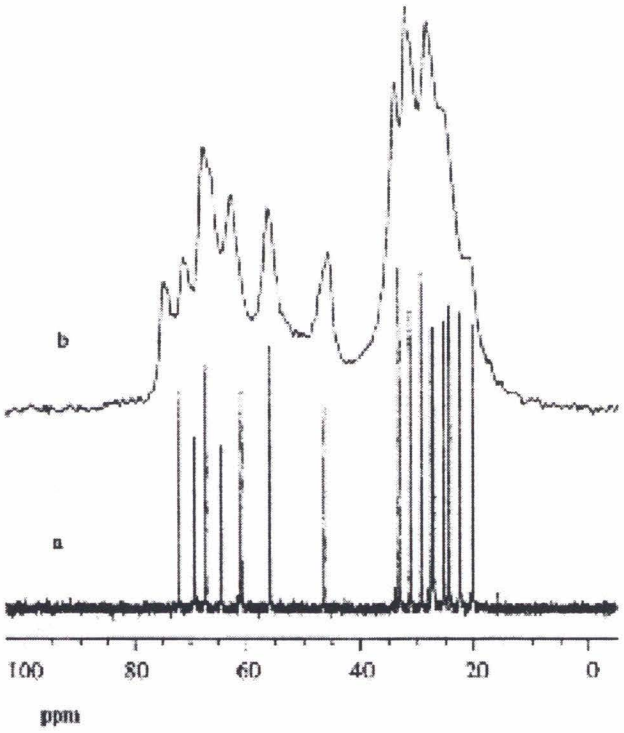


**Figure 2.7.** 13 C NMR of organic SDA, N(16)-methylspartienium: (a) 13 C MAS NMR of as-synthesized pure-silica CIT-5 with SDA occluded in pores and (b) liquid 13 C NMR of N(16)-methylspartienium bromide.

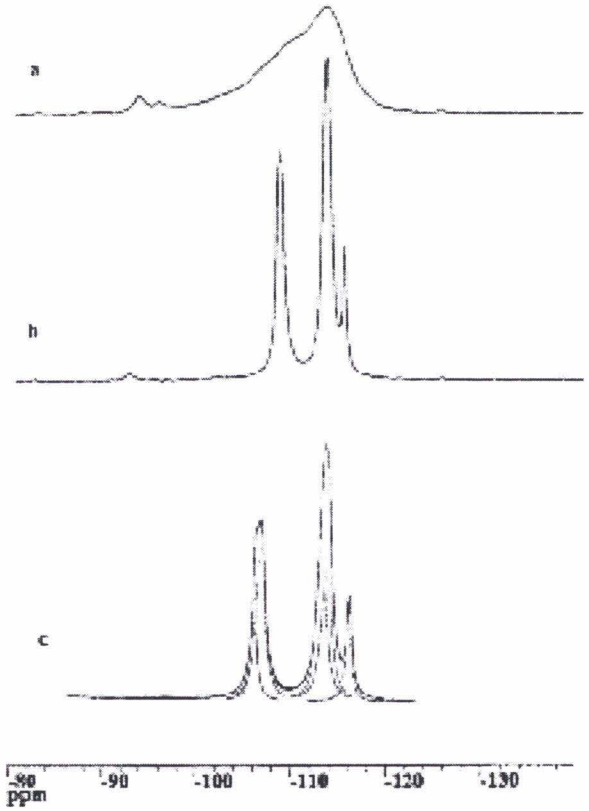


**Figure 2.8.** 29 Si MAS NMR of (a) as-synthesized pure-silica CIT-5, (b) calcined pure-silica CIT-5, and (c) simulated spectra.

# CHAPTER THREE

# Zeolite Structure Solution Fourier Recycling : SSZ-35/SSZ-44

Reprinted with permission from:

[P. Wagner, S. I. Zones, M. E. Davis, R. C. Medrud "SSZ-35 and SSZ-44: Two Related Zeolites Containing Pores Circumscribed by Rings of 10- and 18-Tetrahedral-Atoms"; *Angew. Chem Int. Ed* . in press]

Abstract

The structures of two high-silica molecular sieves, SSZ-44 and SSZ-35 are described. Both materials contain unusual 1-dimensional pores circumscribed by 10 and 18 membered-rings, and are the first high-silica zeolites found that possess pores containing greater than 14 membered-rings. Structure solution and Rietveld refinement from synchrotron powder X-ray data reveal that the two materials are the pure end-member polymorphs of a new fault series and contain similar layer-like units. The SSZ-44 structure is formed by an AB stacking of the layers while the SSZ-35 structure is formed through a ABC stacking of the layer unit.

Introduction

Large and extra-large pore high-silica, microporous materials are in demand as catalysts in the petrochemical and pharmaceutical industries because of their combined properties of shape selectivity, acid strength and high thermal stability.[1-3] Important insights into the catalytic properties of microporous materials are gained through a knowledge of their crystal structures, and these insights can in turn lead to the design of new materials with desirable properties.

Here we present the structure solution of two related high-silica molecular sieves SSZ-44[4,5] and SSZ-35[4,6] with unusual 1-dimensional straight channels containing pore openings that alternate between rings of ten and eighteen tetrahedral-atoms (ten- and eighteen-membered rings, 10 MR and 18 MR). SSZ-35 and SSZ-44 are the first high-silica zeolites that possess pores containing rings larger than 14 MR (during the review of this paper the structure of a clathrate ,*i.e.* nonporous silicate, was reported[7] that is composed of cages that also contain 18 MR). The experimental micropore volumes obtained for SSZ-44 (0.185 cc/g)[5] and SSZ-35 (0.197 cc/g)[6] are significantly larger than any other known 1-dimensional high-silica zeolite including the 14MR zeolites UTD-1[2] and CIT-5[3] that both have micropore volumes less than 0.14

cc/g. SSZ-35 and SSZ-44 demonstrate the potential for dramatically increasing the pore size of thermally stable high-silica zeolites beyond the currently available 14 MR materials. These extra-large pore zeolites are highly desired because they permit catalysis and adsorption to be carried out on large molecules (greater than 8 Å) that are of interest to the pharmaceutical and fine chemicals industries, as well as the petrochemical industry. In addition to possessing unique, large pores, SSZ-35 and SSZ-44 are also the pure end-member polymorphs of a new fault series and allow the complex relationship between the organic structure-directing agent (SDA) and the stacking fault probability of the zeolite framework to be investigated.

The structure of SSZ-44 (Figure 1a) was solved by applying the FOCUS[8] Fourier recycling algorithm to the synchrotron powder X-ray data (SPXRD) and confirmed from the Rietveld refinement[9] of the SPXRD (Figure 2). The SSZ-44 structure is seen to possess mirror plane symmetries parallel to the pore direction [001] that separate two layer-like units related by AB stacking. These layer units are composed of basic building units (BBU) that contain five membered rings (pictured in Figure 1b). The BBUs are combined by stacking along the [001] pore direction and offsetting the units to form staircase-like columns (Figure 1c). These columns are then interconnected as shown in Figure 1d to create the layer-like unit.

Replacement of the mirror plane symmetries possessed by the SSZ-44 structure with inversion centers generates a new topology composed of the same layer-like units found in SSZ-44. This new topology contains an ABC stacking of the layers but still contains a 1-dimensional pore system similar to that found in SSZ-44. The distance least squares (DLS[10]) refinement indicated reasonable structural parameters for this ABC stacking topology.

Similarities between the catalytic activity of SSZ-35 and SSZ-44 led to the identification of SSZ-35 as a potential candidate for the ABC stacking polymorph of SSZ-44. Comparison of the simulated powder X-ray data[11] for the ABC stacking

polymorph to the experimental SPXRD for SSZ-35 and the subsequent Rietveld refinement (Figure 3) have confirmed that SSZ-35 (Figure 1e) is the ABC stacking polymorph of SSZ-44. During the review of this paper a silicate material with the SSZ-35 structure[4] was reported[12] that was synthesized using N,N-dimethyl-6-azonium-1,3,3-trimethylbicyclo(3.2.1) octane[13] as the organic SDA.

SSZ-44 and SSZ-35 both possess an unusual 1-dimensional straight channel system with a pore diameter that alternates between a 10MR and a contorted 18MR (Figure 4). This alternating pore diameter of the straight channels can also be viewed as arising from the stacking of cages that contain 10MR portals at the top and bottom of the cages. The cage structures of the two related materials SSZ-44 and SSZ-35 differ from each other in their unique arrangements of 4, 5 and 6 membered rings circumscribing the internal walls of the cage as seen in Figure 4. The 10 MR of the SSZ-35 material has a free diameter of 5.5 Å x 6.1 Å, while the 18 MR has a free diameter of 12.5 Å x 9 Å. The 10 MRs contained in the SSZ-44 material are nearly circular (free diameter of 5.8 Å) while the 18 MRs possess a slightly larger free diameter (12.9 Å x 9 Å) than those in the SSZ-35 material. For comparison, the only two known extra-large pore, 14 MR zeolites, UTD-1 and CIT-5 contain pores with free diameters of 10 Å x 7.5 Å, and 7.4 Å respectively.

As previously observed, SSZ-35 and SSZ-44 are related to each other through the orientation of the successively stacked layer-like unit that is contained in both structures (Figure 1d). The SSZ-44 topology results if the layers are related through mirror planes and the SSZ-35 topology results if these layers are related through inversion centers (Figure 1a and e). However, the Rietveld refinements indicate that these materials are the pure end-member polymorphs *i.e.*, they are neither faulted or intergrown. This is surprising as there exist numerous examples of faulted or intergrown zeolites that are also composed of similarly related layers with varying stacking probabilities (*e.g.*, FAU/EMT[14], CON/SSZ-33/SSZ-26[15], and zeolite

beta[16]). These faulted intermediates are encountered frequently as a result of the poor specificity of the structure directing agent for a particular end-member polymorph.

Often the pure end-member polymorphs are highly desired for properties that are unique from the faulted intermediates. One notable example is that of the chiral end-member of the zeolite beta fault series that could have tremendous utility in the catalysis and separations of chiral molecules. However, the designed synthesis of pure end-member zeolite polymorphs from the observed faulted intermediates has met with only limited success due to the poor understanding between the properties of the organic structure directing agent or template and the stacking probability of the resulting zeolite framework. Although studies of the EMT/FAU fault series using crown ether SDAs have provided some insight into the effects of the SDA on the FAU/EMT fault probability [17,18], a greater understanding of the factors that influence zeolite faulting is needed.

The SSZ-35 and SSZ-44 materials allow the complex relationship between the SDA and resulting inorganic framework to be investigated by probing the synthetic and structural parameters that determine the stacking probabilities between these end-members[19]. Determining the pertinent factors that govern zeolite faulting will open the possibility of eventually designing fault- and intergrowth-free microporous materials that are of great industrial and academic interest such as chiral zeolite beta.

In addition to being the pure end-member polymorphs of a new fault series these materials are also the first high-silica zeolites found to possess 18-MR containing pores and illustrate the potential for synthesizing thermally stable zeolites with pores larger than 14 MR. Such extra-large pore zeolites are in great demand industrially for catalytic applications on large molecules.

Experimental Procedure

Organic Structure Directing Agent (SDA) Synthesis: The quaternary ammonium compound for use in the SSZ-44 reaction, *N,N*-diethyl 2,6-cis-dimethylpiperidinium (SDA I), is prepared by exhaustive ethylation of 2,6 cis-dimethylpiperidine by ethyl iodide in the presence of potassium bicarbonate in methanol. A more detailed procedure can be found in the analogous description for the 3,5 dimethylpiperdine derivative published by Nakagawa[20]. *N*-ethyl, *N*-methyl 2,6-cis-dimethylpiperidinium (SDA II), that is used to synthesize SSZ-35, is prepared by a sequential alkylation of the 2,6 cis-dimethylpiperidine with ethyl iodide in methanol, removal of HI with potassium bicarbonate, and subsequent reaction of the tertiary base product with methyl iodide, again using methanol for solvent. Note that a large number of other organic SDAs can also be used to crystallize SSZ-35[21]

Each of the SDAs are converted to their $OH^-$ forms from the iodide salts via treatment with AG1-X8 hydroxide ion-exchange resin from BioRad. The exchange can be carried out by running the compound through the resin in a column, or by simply stirring the components overnight. The molarity of the SDA solution is determined by titration.

Zeolite Synthesis: Either zeolite can be synthesized from the appropriate SDA using the following reaction quantities. 5.1 grams of a 0.58 M solution of SDA (SDA I is employed to crystallize SSZ-44 or SDA II for SSZ-35) is measured into the Teflon cup of a Parr 23 ml reactor bomb. 1.5 grams of 1.0 N KOH and 4.4 grams of water are also added. 0.04 grams of Reheis F-2000, hydrated alumina ( ~ 53 wt % $Al_2O_3$ ) is dissolved in the solution. Finally 0.90 grams of Cabosil-M5 ( 97% fumed $SiO_2$) is added to the synthesis mixture and the mixture is stirred. The teflon cup containing the synthesis mixture is closed and sealed in a Parr autoclave. The autoclave is rotated at 43 RPM while heating to 160°C. After 6-11 days of heating the crystalline zeolite

product is obtained. The solids are filtered, washed with approximately 100 times the water volume of the reaction and air dried.

The high-silica materials were prepared for synchrotron powder X-ray data (SPXRD) collection by calcining to 550°C then heating the sample under vacuum in a capillary tube to 350°C and sealing the capillary tube while under vacuum. The data were collected at the X7A beamline at the National Synchrotron Light Source at Brookhaven Laboratory (Upton, NY).

For the Rietveld refinements of SSZ-35 and SSZ-44 from the SPXRD, the background parameters (shifted Chebyshev function), the scale factor, and the zero shift were first refined, followed by the refinement of the lattice parameters and the profile parameters (Simpson's rule integration of the pseudovoight function), and finally the atomic positions and the isotropic temperature factors were refined.

Structure and Refinement Details for SSZ-44: The initial unit cell parameters for the calcined SSZ-44 material were obtained from the indexation of the SPXRD and refined to a=11.48534(26) Å, b=21.94579(49) Å, c=7.38811(14) Å and β=94.7016(3)° (V=1855.9 $Å^3$). Analysis of the systematic absences indicated symmetry consistent with space group $P\,2_1/m$ (no. 11). The observed structure factors were extracted using the LeBail extraction technique[22] and normalized using the scale factor obtained from the Wilson plot of the data. Reflections with d-spacings larger than 1.3 Å were used as a psuedo single crystal data set for input into the Fourier recycling algorithm, FOCUS[8], for structure solution. At the 1.3 Å resolution limit employed, the reflection overlap (defined here as $\theta_1 - \theta_2 < [FWHM_1+FWHM_2)/2]*0.15$) is approximately 80%.

For the Rietveld refinement of SSZ-44, 136 variables were refined over a profile range of 3.0°-50° ($\lambda$=1.20106 Å, step sizes=0.005° resulting in 9400 observables) containing 731 reflections. 82 soft constraints were employed (32: d(Si-O)=1.61(01) Å, 50 d(O-O)=2.61(01) Å) resulting in an average d(Si-O) of 1.597(15) Å with a max.=1.627 Å and min.=1.568 Å. The average O-Si-O angle was 109.47° with a maximum of 112.4° and a minimum of 106.2°, and the average Si-O-Si angle was 151.4° with a maximum of 165.5° and a minimum of 133.0°. The weighting for the soft constraints was reduced but elimination of the constraints caused slight bond angle and distance distortions. The final residual values were $wR_p$=10.58 % and an $R_p$=8.92%. The Fourier difference map showed maximum peaks heights all less than 0.5 $e^-$/Å. The atomic positions together with the isotropic temperature factors are presented in Table 1. This structure solution has been accepted by the International Zeolite Association Structure Committee and the code SFF has been assigned for SSZ-44.

Structure and Refinement Details for SSZ-35: The highest maximal topology of the pure-silica SSZ-35 framework and the symmetry of the as-made SSZ-35 material is monoclinic (*C 2/m*) with unit cell parameters of a=13.9 Å, b=18.2 Å, c=7.4 Å and b=99.4°. However upon calcination the interaxial angles of the monoclinic cell relax to $\alpha$ =90.924°, $\beta$=98.920°, and $\gamma$ =89.437° that lowers the symmetry to triclinic (space group symmetry to *P-1*). The refined unit cell parameters for the SSZ-35 reduced cell are a=11.411404(137) Å, b=11.526825(136) Å, c=7.376957(74) Å, $\alpha$=94.6607(7)° $\beta$=96.2055(8)° and $\gamma$=104.8919(6)° (V=926.244 $Å^3$).

For the Rietveld refinement of SSZ-35, 123 parameters were refined over the profile range 7°-80° ($\lambda$=1.20106 Å, step sizes=0.005° resulting in 14600 observables).

80 soft constraints were employed (32: d(Si-O)=1.61(01) Å, 48: d(O-O)=2.61(01) Å) resulting in an average d(Si-O)=1.599(11) Å (max. = 1.6165 Å, min. = 1.5765 Å), an average O-Si-O angle of 109.466° with a maximum of 111.77° and a minimum of 107.52°, and an average Si-O-Si bond angle of 152.33° with a minimum angle of 136.618° and a maximum of 162.62°. The weighting for the soft constraints was reduced but elimination of the constraints caused slight bond angle and distance distortions. The final refinement resulted in an $wR_p$=11.88% and an $R_p$=9.95%. The Fourier difference map showed maximum peaks heights all less than 0.6 $e^-$/Å. The atomic positions together with the isotropic temperature factors are presented in Table 2. This structure solution has been accepted by the International Zeolite Association Structure Committee and the code STF has been assigned for SSZ-35.

Further details of the crystal structure investigations may be obtained from the Fachinformationszentrum Karlsruhe, D-76344 Eggenstein-Leopoldshafen, Germany (fax: (+49) 7247-808-666; email: crysdata@fiz-karlsruhe.de) on quoting the depository numbers CSD-410595 for SSZ-35 and CSD-410596 for SSZ-44.

References

[1] M. E. Davis, *Chem. Ind. (London)* **1992**, 4, 137.

[2] C.C. Freyhardt, M. Tsaptsis, R. F. Lobo, K. J. Balkus, and M. E. Davis, *Nature* **1996**, *381*, 295.

[3] P. Wagner, M. Yoshikawa, M. Lovallo, K. Tsuji, M. Tsaptsis, M. E. Davis, *Chem. Comm.* **1997**, 2179-2180.

[4] P. Wagner, S. I. Zones, R. C. Medrud, M. E. Davis, *Abstr. Pap. 12th Int. Zeolite Conf.* (Baltimore, MD) July **1998**.

[5] Y. Nakagawa (Chevron Research and Technology Company) U.S. Patent No. 5,580,540 **1996.**

[6] Y. Nakagawa (Chevron Research and Technology Company) U.S. Patent No. 5,316,753 **1994**.

[7] R. Lobo, private communication.

[8] R. W. Grosse-Kunstleve, L. B. McCusker, and Ch. Baerlocher, *J. Appl. Cryst.* **1997**, *30*, 985-995.

[9] A. C. Larson and R. B. Von Dreele, Los Alamos Laboratory Report No. LA-UR-86-748 **1987**.

[10] C. Baerlocher, A. Hepp and W. M. Meier, DLS-76, Institute fur Kristallographie, ETH, Zurich, Switzerland, **1977**.

[11] CERIUS Version 3.2, Molecular Simulations, Cambridge, UK, **1993**.

[12] L. Villaescusa, P. A. Barrett and M. A. Camblor, *Chem. Commun.* **1998**, *21*, 2329-2330.

[13] P. Wagner, S. I. Zones, S. Elomari, Y. Nakagawa, M. E. Davis, *Abstr. Pap. 12th Int. Zeolite Conf.* (Baltimore, MD) July **1998**.

[14] M. W. Anderson, K. S. Pachis, F. Prebin, S. W. Carr, O. Terasaki, T. Ohsuna and V. Alfredsson, *J. Chem Soc Chem Commun.* **1991**, 1660-1664.

[15] R. F. Lobo, M. Pan, I. Chan, H. X. Li, R. C. Medrud, S. I. Zones, P. A. Crozier and M. E. Davis, *Science* **1993**, *262*, 1543-1546.

[16] J. M. Newsam, M. M. J. Treacy, W. T. Koetsier and C. B. de Gruyter, *Proc. R. Soc. Lond. A* **1988**,*420*, 375-405.

[17] T. Ohsuna, O. Terasaki, V. Alfredsson, J. O. Bovin, D. Watanabe, S. W. Carr, M. W. Anderson, *Proc. R. Soc. Lond. A* **1996**, *452*, 715-740.

[18] J. P. Arhancet, M. E. Davis, *Chem Mater.* **1991**, *3*, 567-569.

[19] P. Wagner, S. I. Zones, M. E. Davis in prep.

[20] Y. Nakagawa (Chevron Research and Technology Company) World Patent No. WO95/09812, **1995.**

[21] P. Wagner, Y. Nakagawa, G. S. Lee, S. Elomari, M. E. Davis, R. C. Medrud, S. I. Zones, submitted to JACS.

[22] A. LeBail, H. Duroy, J.L. Fourquet, *Mater. Res Bull.* **1988**, *23*, 447-452.

**Table 3.1.** Fractional Atomic Coordinates for SSZ-44, e.s.d's in parentheses, (monoclinic, *P* $2_1/m$, a=11.48534(26), b=21.94579(49), c=7.38811(14) Å and β =94.7016(3)°)

| Atom | a | b | c | U(iso) |
|---|---|---|---|---|
| SI | 0.27227(57) | 0.97791(29) | 0.93601(92) | -0.0044 |
| SI | 0.13548(63) | 0.62930(29) | 0.10193(97) | -0.0023 |
| SI | 0.23886(57) | 0.67904(28) | 0.47825(90) | 0.0142 |
| SI | 0.39323(60) | 0.56890(30) | 0.59794(84) | 0.0019 |
| SI | 0.03652(58) | 0.68184(27) | 0.74254(92) | 0.0161 |
| SI | 0.05149(61) | 0.04087(32) | 0.76211(88) | 0.0115 |
| SI | 0.11053(58) | 0.06798(30) | 0.36508(91) | -0.0059 |
| SI | 0.35948(58) | 0.02838(31) | 0.29204(89) | 0.0039 |
| O | 0.22578(82) | 0.91806(33) | 0.02742(13) | 0.0110 |
| O | 0.32885(84) | 0.96241(46) | 0.75474(103) | 0.0330 |
| O | 0.36382(71) | 0.01059(45) | 0.08089(86) | 0.0365 |
| O | 0.16115(66) | 0.02349(41) | 0.89856(12) | 0.0162 |
| O | 0.02146(73) | 0.59436(39) | 0.15514(13) | -0.0042 |
| O | 0.19913(84) | 0.66360(45) | 0.27348(97) | 0.0097 |
| O | 0.09682(88) | 0.67737(39) | 0.94529(100) | 0.0453 |
| O | 0.27877(107) | 0.7500 | 0.49498(185) | 0.0128 |
| O | 0.34544(77) | 0.63729(30) | 0.55819(136) | 0.0259 |
| O | 0.13244(80) | 0.66902(52) | 0.60239(139) | 0.0218 |
| O | 0.36967(107) | 0.53179(37) | 0.41218(103) | 0.0088 |
| O | 0.53084(53) | 0.57271(41) | 0.65389(140) | 0.0194 |
| O | 0.93509(70) | 0.63319(30) | 0.70903(128) | 0.0258 |
| O | 0.98407(103) | 0.7500 | 0.71105(177) | 0.0303 |
| O | 0.96479(79) | 0.98471(36) | 0.73380(146) | 0.0147 |
| O | 0.09791(92) | 0.06329(49) | 0.57827(89) | 0.0087 |
| O | 0.24371(53) | 0.06267(46) | 0.32726(144) | 0.0365 |

**Table 3.2**. Fractional Atomic Coordinates for SSZ-35, e.s.d's in parentheses, (triclinic, *P -1*, a=11.411404(137) Å, b=11.526825(136) Å, c=7.376957(74) Å, α=94.6607(7)°, β=96.2055(8)° and γ=104.8919(6)°)

| Atom | a | b | c | U(iso) |
|---|---|---|---|---|
| SI | 0.36019(35) | 0.35630(33) | 0.61106(50) | 0.01319 |
| SI | 0.41221(34) | 0.42852(33) | 0.21918(49) | 0.01888 |
| SI | 0.14209(37) | 0.64205(36) | 0.40966(53) | 0.02179 |
| SI | 0.36181(37) | 0.85678(37) | 0.57148(54) | 0.02607 |
| SI | 0.13396(37) | 0.44151(35) | 0.67151(54) | 0.01930 |
| SI | 0.23859(38) | 0.56731(36) | 0.04636(53) | 0.02242 |
| SI | 0.46001(38) | 0.75796(38) | 0.92351(53) | 0.02925 |
| SI | 0.55968(37) | 0.87468(35) | 0.30376(52) | 0.02226 |
| O | 0.36502(60) | 0.37709(37) | 0.40067(83) | 0.02369 |
| O | 0.23168(48) | 0.36461(47) | 0.67114(77) | 0.01125 |
| O | 0.47018(43) | 0.45770(45) | 0.73017(88) | 0.03990 |
| O | 0.37472(50) | 0.22510(37) | 0.64375(83) | 0.02625 |
| O | 0.30673(48) | 0.47043(48) | 0.10734(76) | 0.03288 |
| O | 0.44890(49) | 0.32523(47) | 0.09908(72) | 0.03153 |
| O | 0.22725(38) | 0.77005(38) | 0.50790(72) | 0.02335 |
| O | 0.16588(60) | 0.54074(44) | 0.53230(76) | 0.02545 |
| O | 0.17639(55) | 0.61558(53) | 0.20899(78) | 0.03111 |
| O | 0.00178(28) | 0.64477(50) | 0.39598(79) | 0.01427 |
| O | 0.43707(44) | 0.85788(66) | 0.39827(68) | 0.03808 |
| O | 0.35217(52) | 0.99191(30) | 0.62479(81) | 0.02041 |
| O | 0.43055(53) | 0.81119(54) | 0.73707(58) | 0.02927 |
| O | 0.13629(45) | 0.50548(50) | 0.87315(54) | 0.01517 |
| O | 0.33382(44) | 0.67945(46) | 0.98040(85) | 0.03128 |
| O | 0.52218(51) | 0.86584(43) | 0.08546(49) | 0.02315 |

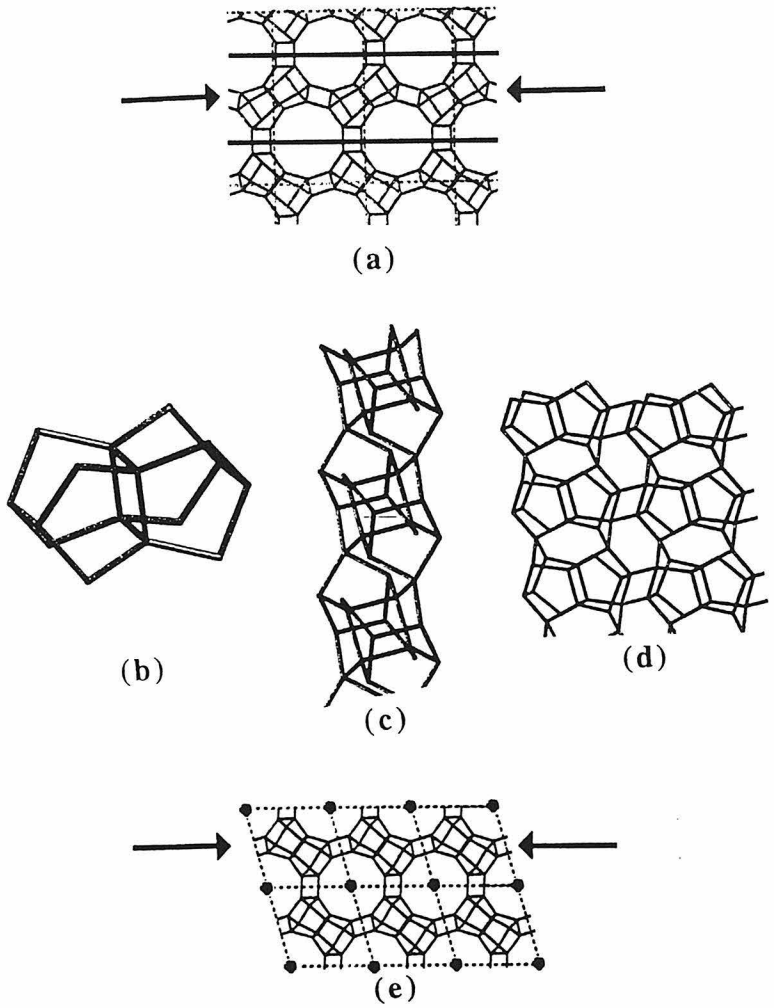


**Figure 3.1**. Framework topology of SSZ-44 viewed down the pores ([001] direction). The oxygen atoms have been omitted for clarity. Mirror planes are represented by solid lines separating layer-like building units (a). Arrows indicate layer-like unit common to both SSZ-44 and SSZ-35. Basic building unit (BBU) of SSZ-35 and SSZ-44 (b), Interconnection of BBUs along pore direction ([001] direction) to form stacked columns (c), Interconnection of stacked columns to form layer-like unit common to both SSZ-35 and SSZ-44 (d), Framework topology of SSZ-35 viewed down the pores ([001] direction). Inversion centers are represented by black dots separating layer-like building units (e).

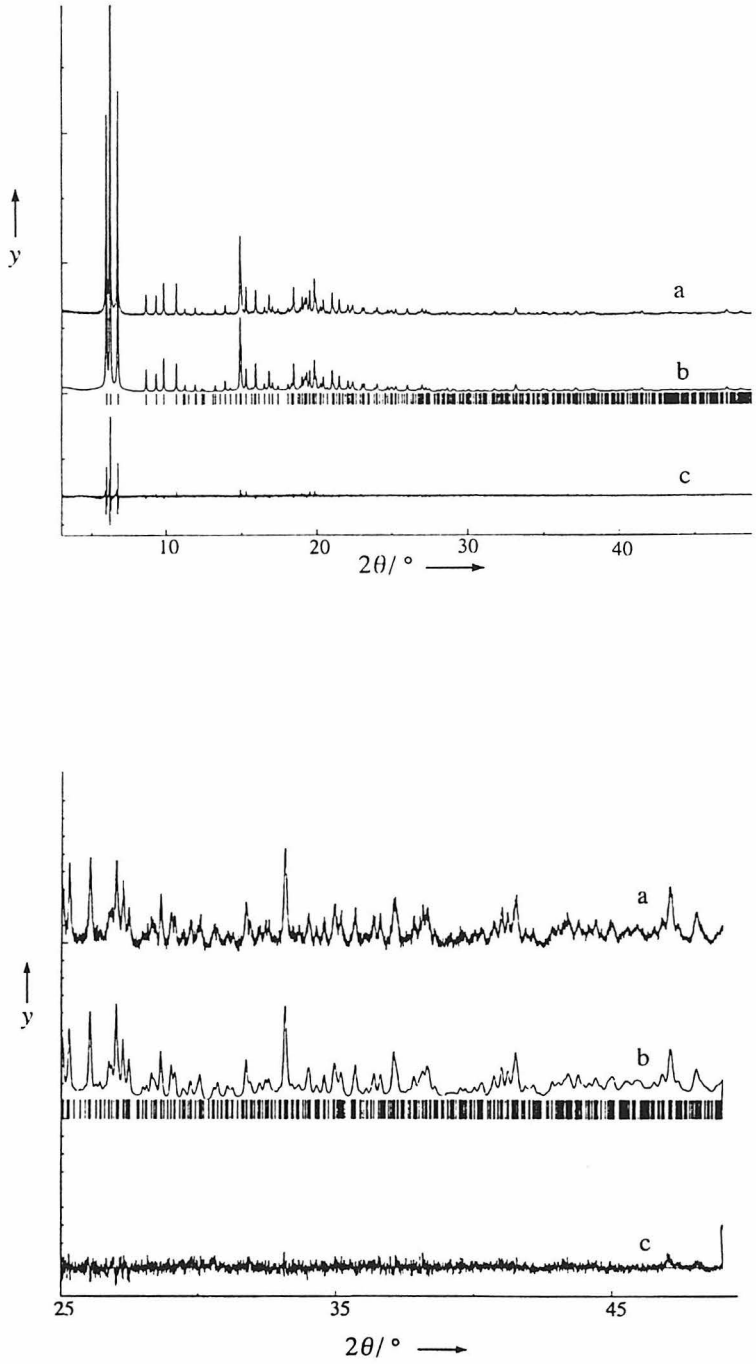


**Figure 3.2**. Synchrotron powder X-ray Rietveld refinement of SSZ-44 experimental (a), simulated (b) and difference (c) plots (plotted vs. relative intensity).

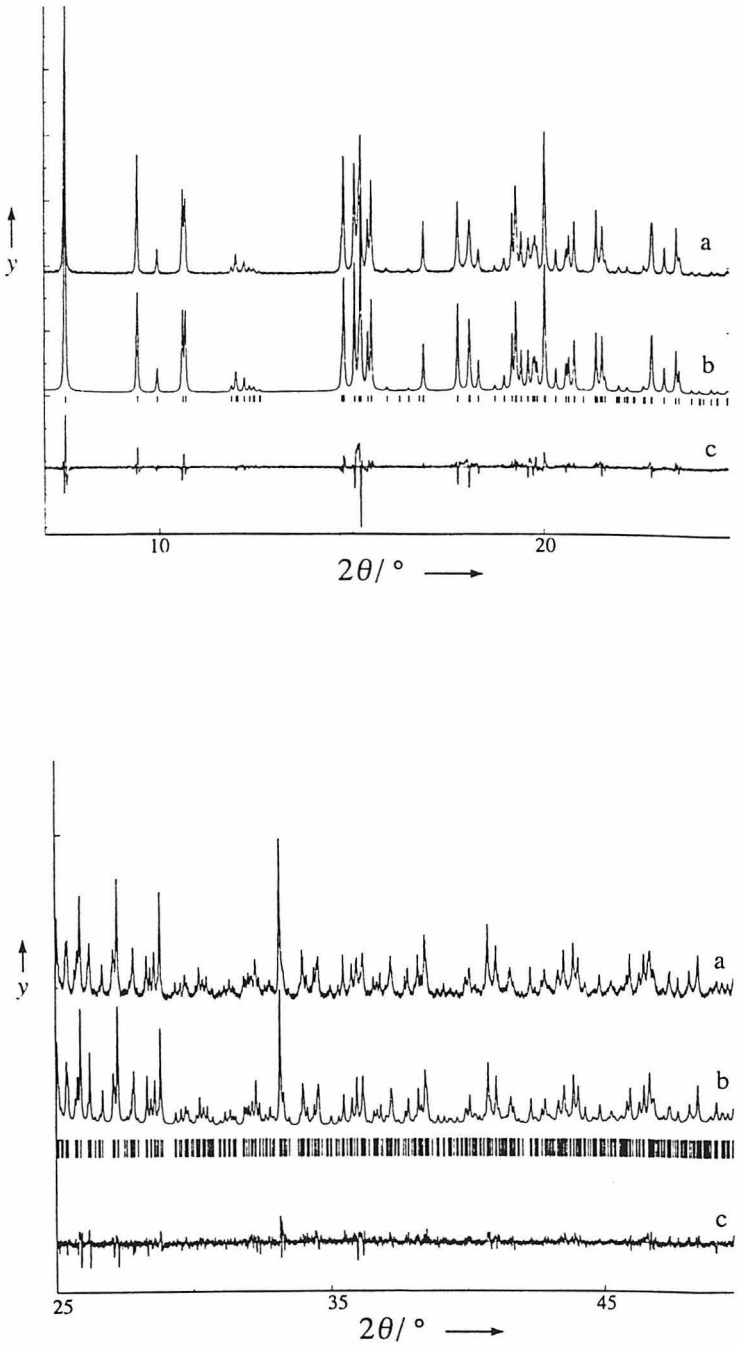


**Figure 3.3.** Synchrotron powder X-ray Rietveld refinement of SSZ-35 experimental (a), simulated (b) and difference (c) plots (plotted vs. relative intensity).

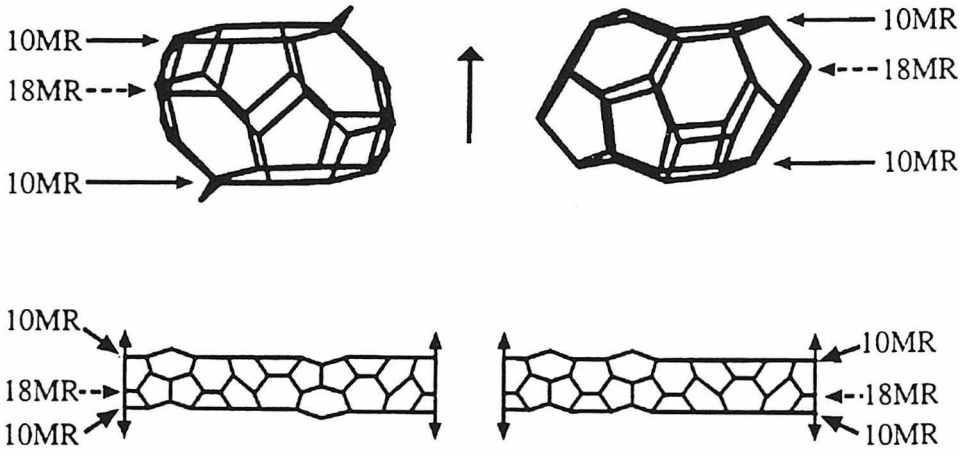


**Figure 3.4.** Illustration of the alternating 10MR-18MR pore diameter for the SSZ-35 (a) and SSZ-44 (b) structures. Pore direction ([001] direction) is parallel to central vertical arrow. Arrangement of the ring system circumscribing the internal pore surface is diagrammed below.

# CHAPTER FOUR

# Zeolite Structure Solution Electron Diffraction : SSZ-48

[P. Wagner, O. Terasaki, S. Ritsch, S. I. Zones, M. E. Davis, K. Hiraga "Electron Diffraction Structure Solution of a Nano-Crystalline Zeolite at Atomic Resolution" submitted to *J. Phys. Chem. B*]

Abstract

Here, we report the use of electron diffraction data to obtain the structure solution of a large-pore, high-silica zeolite, SSZ-48, containing an occluded organic structure directing agent. The structure is confirmed by electron diffraction refinement and by high resolution transmission electron microscopy and is found to contain a one-dimensional pore system circumscribed by 12 tetrahedral atoms (12 MR). SSZ-48 is the most complex three-dimensional material to be solved at atomic resolution using electron diffraction methods and illustrates the power of electron diffraction data for resolving the structures of materials that form crystals too small for standard single crystal X-ray analysis.

Introduction

Microporous materials (including zeolites) that contain molecular-sized pores and cavities have found wide-spread use in industry as molecular sieves for chemical separations, as ion-exchangers for detergents and as heterogeneous, shape-selective catalysts[1]. Knowledge of the crystal structure of these microporous materials can provide important insights into their properties and can lead to the design of desirable materials.

The structure solution of microporous materials can be challenging however, because these materials tend to form as micron or submicron sized crystals that are too small for single crystal X-ray analysis[2]. In the absence of single crystal data, the structure solution and refinement has typically required the use of powder X-ray data[3,4]. The difficulty in solving crystal structures from powder X-ray data is that the three dimensions of information available in a single crystal data set are collapsed into one dimension (d-spacing) in a powder X-ray data set. If the reflections in the powder X-ray data are significantly overlapping then solving the crystal structure from this data can be extremely difficult. While the techniques for solving complicated crystal

structures using powder X-ray data are continuing to advance[5-7], they are still far from routine, particularly for zeolites that may contain several hundred atoms in a unit cell.

Alternatively, electron microscopy may be utilized for solving the crystal structures of materials that form crystals too small for single crystal X-ray analysis. In particular, image reconstruction from high resolution transmission electron micrographs has been applied for solving structures from micro and nanocrystals[8-10]. However, materials that tend to be highly electron beam sensitive, *e.g.*, organic crystals[11,12] and crystalline microporous materials, may be easily destroyed by the electron beam under imaging conditions. In contrast, under optimal diffraction conditions, the electron beam is highly overfocused to obtain parralel illumination of the sample. Therefore, the use of electron diffraction analysis rather than image analysis for crystal structure elucidation can allow for higher resolution and higher dimensional information to be collected from a single crystal of an electron-beam sensitive material.

Electron diffraction data, obtained from a transmission electron microscope (TEM), also has inherent advantages over X-ray data for analyzing small crystals due to the stronger interaction between the electron beam and matter compared to X-rays[13]. This stronger interaction allows a single crystal diffraction data set to be obtained from much smaller crystals. Provided that the interaction of the incident electron beam with the crystal is nearly kinematical, *i.e.*, the diffraction intensity is proportional to the square of the structure factor indicating that there are few dynamical scatterings of the electrons within the crystal, direct methods can be used as a powerful tool for obtaining the phase information required to solve the crystal structure. High-silica microporous materials are particularly well suited to electron diffraction analysis[14,15] due to the low density of porous materials and the absence of heavy atoms.

To illustrate the feasibility of structure solution of complex crystal structures via electron diffraction data, we report here the structure solution of the new high-silica

molecular sieve, SSZ-48 containing an organic structure directing agent. The atomic resolution structure solution and refinement highlights the power of electron crystallography for resolving structures from micro- and nano-crystals that are too small for single crystal X-ray analysis.

Experimental

*Synthesis.* N,N-diethyldecahydroquinolinium cation, used as a structure directing agent (SDA) in the synthesis of the high silica zeolite SSZ-48, is synthesized by dissolving 24.8 grams of decahydroquinoline (Aldrich, mixture of isomers) and 26 grams of potassium bicarbonate in 170 ml of methanol. 67.4 grams of iodoethane are added dropwise to the solution over a 10-15 minute period. The solution is refluxed for 48 hours. The reaction mixture is cooled to room temperature, the methanol is evaporated and the remaining solids are treated with 250 ml of chloroform; the undisolved solids are filtered out. The chloroform fraction is evaporated and the solids are recrystallized from a minimum of hot isopropyl alocohol. The dried solids are then ion-exchanged to the hydroxide form by treatment with BioRad AG 1-X8 OH resin and the molarity is determined by titration.

The borosilicate zeolite SSZ-48 is synthesized by mixing 3 mmol of the N,N-diethyldecahydroquinolinium structure directing agent solution ( 5.33 grams, 0.562 mmol OH-/g) with 1.2 grams of 1.0 N NaOH and 5.4 grams of water. Sodium borate decahydrate (0.057 grams) is added to this solution and stirred until all of the solids have dissolved. Cabosil M-5 fumed silica (0.92 grams) is then added to the solution and the resulting mixture is heated at 160 °C and rotated at 43 rpm for 49 days. The precipitated product is filtered, washed and air dried.

*Analytical.* The as-synthesized SSZ-48 crystals were prepared for microscopy by embedding them in epoxy followed by ultramicrotomy. The resulting thinly sliced crystal-embedded epoxy wer then transferred onto a holey carbon foil supported by a

Cu-grid. Electron diffraction data were collected on a JEM-4000EX operating at 400 kV equipped with a slow-scan CCD detector (Gatan 694). HRTEM images were also collected on a JEM-4000EX operating at 400 kV (point resolution 1.7 Å) and were recorded on high-sensitivity photographic film. Image contrast calculation were performed according to the multislice algorithm with Mac Tempas software. All Fourier image filtering of the HRTEMs were performed with the Gatan DigitalMicrograph 2.5 software. SEMs of the as-made SSZ-48 crystals were collected on a Hitachi S-3200 scanning electron microscope operating at 5 kV.

Results and Discussion

Crystal Size Determination. Low resolution transmission electron micrographs and scanning electron micrographs are shown in Figure 1. These micorgraphs reveal that the typical crystal dimensions of SSZ-48 (synthesized as discussed previously) are 0.05 μm x 0.25 μm x 10 μm. While single crystal X-ray analyses have been carried out on high silica molecular sieves that are greater than 1 μm in size, the SSZ-48 crystals are well below the size restriction for standard single crystal X-ray analysis as seen from Figure 1.

Electron Diffraction Structure Solution of SSZ-48. The integrated intensities for 600 reflections (326 unique reflections) were extracted from 11 zones of selected area electron diffraction data that were collected to a resolution of 0.99 Å ( $-8 < h < 8$, $-4 < k < 4$, $-10 < l < 13$ ) and merged by normalizing the diffraction data between zones containing common reflections. The indexation of these reflections revealed a monoclinic crystal class having unit cell parameters of a=11.19 Å , b=4.99 Å, c=13.65 Å and beta = 100.7° (V=748.6 $Å^3$). The analysis of the reflections for systematic

absences indicated a space group consistent with $P\ 2_1$ (No. 4). The experimental electron diffraction data for the 3 principle zones axes is presented in Figure 2.

Electron atomic scattering factors[16], were used in the direct methods structure solution[17] and subsequent refinement[18]. The integrated diffraction intensities were not corrected for dynamical diffraction effects or curvature of the Ewald sphere. The temperature factor ($B_{iso}$ = 1.94 Å$^2$), obtained from the Wilson plot[19], provides additional support that the data is not seriously perturbed by dynamical diffraction effects.

Reflections with normalized structure factors between 0.65 and 10.0 were used in the direct methods structure solution, resulting in 157 reflections that were employed to calculate 2588 unique triple product relations. The phases obtained from the direct methods structure solution were used to generate a 3-dimensional potential map that easily revealed the 7 silicon atoms in the basis set of the framework structure for the high-silica molecular sieve, SSZ-48. The 3-dimensional potential map also contained the positions of 5 of the 14 oxygen atoms. Additional scattering material in the potential map was located within the channel system of the model and is attributed to the occluded organic structure directing agent (SDA), *N,N* - diethyldecahydroquinolinium. The 3-dimensional crystal potential calculated from the direct methods structure solution is shown in Figure 3 and the atomic coordinates of the asymmetric unit are presented in Table 1. The remaining oxygen atoms in the framework were located using distance least squares refinement (DLS[20]) to optimize Si-O bond distances and O-Si-O bond angles. The DLS refined model (DLS R-value=0.0028) contains 7 silicon and 14 oxygen atoms in the asymmetric unit.

Refinement of SSZ-48 Structure from Electron Diffraction Data. The silicon and oxygen atoms from the DLS refined structure, together with 3 carbon atoms (placed at the coordinates of the largest potential peaks inside the channel system) were input as

the starting model for the least squares refinement. The structural refinement was carried out in space group $P\,2_1$ (No. 4) with the unit cell parameters determined from the indexation of the diffraction pattern. The model was refined against $F_o^2$ with 600 experimentally measured reflections (326 unique reflections). The Fourier difference map revealed the positions of 4 additional scattering centers located within the channel system that were attributed to the carbon atoms of the organic SDA. All atomic positions were refined, however due to poor overdetermination (326 unique reflections and 94 variables), constraints were placed on the Si-O bond distances (d(Si-O)=1.61(01) Å) and on the O-Si-O bond angles (d(O-O)=2.61(01) Å; O-Si-O = 109.45°). The isothermal temperature factors were refined and constrained to the same values for Si and for O atom types. The isothermal temperature factors for the 7 carbon atoms within the pores were not constrained. The final $R_F$ value ($R_F = \Sigma|Fo-Fc| / \Sigma|Fo|$) was reduced to 0.3283, resulting in a refined model containing chemically reasonable Si-O bond distances (ave. = 1.601 Å), O-Si-O bond angles (ave. =109.47°), and Si-O-Si bond angles (ave. =147.3°). While the $R_F$ value is high compared to single crystal X-ray analyses, it is comparable to the $R_F$ values obtained in other electron diffraction studies[21].

The SSZ-48 framework structure contains a 1-dimensional, sinusoidal, pore system circumscribed by 12 tetrahedrally coordinated silicon atoms, (12 membered-rings, 12 MR). The pores are elliptical in shape with projected dimensions of 7.91 Å x 10.05 Å (center of oxygen to center of oxygen) and a maximum internal pore diameter of 11.19 Å x 13.65 Å (center of oxygen to center of oxygen). The asymmetric unit contains 7 tetrahedrally coordinated silicon atoms (T-atoms) and 14 oxygens resulting in a unit cell content of $[Si_{14}O_{28}]$. The framework density (FD) of the material is 18.7 T-atoms/1000 $Å^3$. Table 2 contains the atomic positional parameters for the refined model (shown in Figure 4).

The connectivity of the T-atoms in the SSZ-48 structure is similar to the connectivity of the T-atoms in the TON[22] structure that contains 10 MR pores (Figure 5a). Both structures are composed of columns of $[5^4.6^1]$ units as seen in Figure 5. Within these columns the connectivity is identical, however, in the SSZ-48 structure the columns are expanded by the insertion of rings of 4 T-atoms diagonally across the pore. This expansion can occur at the joining of any of the $[5^4.6^1]$ units, however the SSZ-48 material is neither disordered or faulted and indicates a strong specificity of the *N,N* -diethyldecahydroquinolinium SDA for the SSZ-48 structure. If the 4 T-atom rings are inserted at the joining of every $[5^4.6^1]$ unit, a new extra-large pore framework structure is generated that contains 14 T-atom pore openings and has a maximum internal pore diameter of 14.4 Å x 12.8 Å (Figure 5c). The detailed SSZ-48 crystal structure presented here, of the organic SDA within the pores of the SSZ-48 framework, provides valuable insights into the organic/inorganic interactions. Such information opens the possibility for rational zeolite design by modifying the SSZ-48 SDA to optimize the organic/inorganic interactions for the formation of the proposed extra-large pore 14 MR structure

Dynamical Scattering Refinement. In order to improve the match between the calculated and observed structure factors, dynamical diffraction effects were taken into account. The model used for the dynamical diffraction simulations was obtained by molecular modeling of the SDA in the high-silica framework. The organic SDA, *N,N*-diethyldecahydroquinolinium, was adjusted within the pores of the refined framework model to minimize the energy of the system using the Open Force Field module of Cerius[2] (Burchart 1.01-Universal 1.02 force field)[23]. The positions of the Si and O atoms in the framework and the unit cell parameters were fixed and the orientation and position of the organic SDA was allowed to vary in order to minimize the energy of the system.

The energy minimized model of the SDA occluded within the pores of the framework structure (Figure 6) was then used for simulations of electron diffraction intensities[24] for different crystal thicknesses that resulted in varying degrees of dynamical diffraction. Simulated diffraction intensities were obtained for the principle zone axes, [001], [010], and [100] and were quantitatively compared to the experimental data to determine the degree of dynamical diffraction by minimizing $R_F$ as a function of crystal thickness. As Table 3 indicates, the $R_F$ value for the 14 unique reflection of the [001] zone minimized to 0.224 at a thickness of 55 nm, the $R_F$ value for the 14 unique reflection of the [100] zone minimized to 0.199 at 67 nm, and the $R_F$ value for the 105 unique reflection of the [010] zone minimized to 0.241 at 25 nm. The overall $R_F$ calculated for all three zones, containing 133 reflections (structure factors located in Supplementary Material), is 0.232. As a reference, an R-value below 0.25 is an indication that the atomic positions of the structure are correct to within approximately 0.1 Å[25].

The comparison between the Fourier filtered experimental high resolution transmission electron micrographs and the simulated TEM images viewed parallel to the pore direction, [010], and perpendicular to the pore direction, [001], shown in Figure 7 provide additional confirmation of the structure. The simulated images are calculated using the model obtained from the electron diffraction structure solution and refinement (Figure 7).

## Conclusions

The atomic resolution, 3-dimensional structure that is elucidated here is the most complicated solved via electron diffraction methods. These results demonstrate the feasibility of single crystal electron diffraction analysis for elucidating complex crystal structures of electron-beam sensitive materials that tend to form as crystals too small for X-ray single crystal analysis. It is clearly demonstrated that electron diffraction

structure solution can be successfully applied to obtain the atomic level details of very complex materials with large unit cells.

References

1. Davis, M. E. *Chem Ind. (London)* **1992,** 4, 137.

2. Baerlocher, Ch. and McCusker L. B. *St. Surf. Sci* . **1994**, 85, 391-428.

3. Freyhardt, C. C.; Tsapatsis, M.; Lobo, R. F. ; Balkus, K. J. ; Davis, M. E. *Nature*, **1996**, 381, 295-298.

4. Wagner, P.; Yoshikawa, M.; Lovallo, M.; Tsuji, K.; Taspatsis, M.; Davis, M. E. *Chem. Commum.* **1997**, 22, 2179-2180.

5. Grosse-Kunstleve, R. W.; McCusker, L. B.; Baerlocher, Ch. *J. Appl. Crys.* **1997**, 30, 985-995.

6. Altomare, A.; Foadi, J.; Giacovazzo C.; Guagliardi, A.; Moliterni, A. *J. Appl. Crys.* **1996**,29, 674-681.

7. Deem, M. W. and Newsam, J. M. **1992**, 114, 7189.

8. Hu, J. J. ; Li, F. H. ; Fan, H. F. *Ultramicroscopy* **1992**, 41, 387-397.

9. Weirich, T. E. ; Ramlau, R.; Simon, A.; Hovmoller, S.; Zou, X. D. *Nature* **1996**, 382, 144-146.

10. Carlsson, A.; Oku, T.; Bovin, J. O.; Wallenberg R.; Malm J.O.; Schmid. G.; Kubicki T. *Angew. Chem. Int. Ed.* **1998**, 37.

11. Nicolopoulos S. Gonzalez-Calbet, J.; Valletregi, M.; Corma, A.; Correl, C.; Guil J.; Perez Pariente, J. *J. Am. Chem. Soc.* **1997**, 117, 8947-8956.

12. Dorset, D. L. and McCourt, M. P. *Microsc. Res.* **1997**, 36, 212-223.

13. Cowley, J. M. *Diffraction Physics* 2nd edn (North-Holland, Amsterdam, 1984).

14. Dorset, D. L. *Ultramicroscopy* **1992**, **45**, 357-364.

15. Dorset, D. L.;Tivol, W. F.; Turner, J. N. *Acta Crystallogr* **1992**, A48, 562-568.

16. Doyle,. P. A. andTurner, P. S. *Acta Crystallogr.* **1968**, A24, 390-397.

17. Sheldrick, G. *SHELXS-97* (1997).

18. Sheldrick, G. *SHELXL-97* (1997).

19. Wilson, A. J. *Nature* **1942**, 150, 151-152.

20. Baerlocher, Ch. ; Hepp, A. ; Meier, W. M. *DLS-76: A Fortran Program for the Simulation of Crystal Structures by Geometric Refinement*, Laboratorium fuer Kristallographie, ETH, Zurich, Switzerland (1977).

21. Dorset, D. L. *Structural Electron Crystallography* , Plenum Press (New York, 1995).

22. Meier, W. M. ;Olson, D. H.; Baerlocher, Ch. *Atlas of Zeolite Structure Types* (Elsevier, London, 1996)

23. Cerius2 v3.5, Molecular Simulations Inc. **1997**.

24. Stadelmann, P. *Ultramicroscopy* **1987**, 21, 131.

25. Stout, G. H. and Jensen, L. H. *X-ray Structure Determination : A Practical Guide*, John Wiley and Sons (New York, 1989).

**Table 4.1.** Atomic positions (fractional coordinates) from the 3-dimensional crystal potential obtained from structure solution. Space group $P\,2_1$, a=11.19 Å, b= 4.99 Å, c=13.65 Å , and beta=100.7°

| Atom Type | a | b | c |
|---|---|---|---|
| Si | 0.26370 | 0.37680 | 0.18050 |
| Si | 0.38860 | 0.36240 | 0.37170 |
| Si | 0.44340 | 0.23520 | 0.62170 |
| Si | 0.58230 | 0.34610 | 0.87400 |
| Si | 0.32030 | 0.25080 | 0.77750 |
| Si | 0.76410 | 0.16000 | 0.11450 |
| Si | 0.96020 | 0.18460 | 0.03870 |
| O | 0.14770 | 0.44200 | 0.13960 |
| O | 0.25800 | 0.43960 | 0.87740 |
| O | 0.34500 | 0.12900 | 0.53840 |
| O | 0.63300 | 0.38690 | 0.15800 |
| O | 0.03650 | 0.44640 | 0.97450 |
| C | 0.01640 | 0.38520 | 0.65080 |
| C | 0.66940 | 0.26290 | 0.45710 |
| C | 0.95720 | 0.39190 | 0.54440 |
| C | 0.04880 | 0.30610 | 0.76070 |
| C | 0.08050 | 0.19480 | 0.84070 |
| C | 0.12720 | 0.39150 | 0.37460 |
| C | 0.87940 | 0.10870 | 0.61460 |
| C | 0.19950 | 0.26880 | 0.27480 |
| C | 0.84460 | 0.51030 | 0.68000 |

**Table 4.2.** Refined atomic positions (fractional coordinates) for SSZ-48. Space group *P* $2_1$ (No.4). , a=11.19 Å, b= 4.99 Å, c=13.65 Å , and beta=100.7°. Standard deviation in parentheses.

| Atom Type | a | b | c | $U_{iso}$/Å$^2$ |
|---|---|---|---|---|
| Si | 0.2610(16) | 0.384(4) | 0.1890(13) | 0.111(13) |
| Si | 0.3974(14) | 0.277(4) | 0.3936(14) | 0.111(13) |
| Si | 0.4462(15) | 0.277(4) | 0.6064(13) | 0.111(13) |
| Si | 0.6300(15) | 0.379(4) | 0.8961(13) | 0.111(13) |
| Si | 0.3584(14) | 0.432(3) | 0.8028(12) | 0.111(13) |
| Si | 0.7469(15) | 0.409(4) | 0.1201(12) | 0.111(13) |
| Si | 1.0029(12) | 0.475(5) | 0.0667(10) | 0.111(13) |
| O | 0.2840(19) | 0.343(5) | 0.3073(11) | 0.110(13) |
| O | 0.352(2) | 0.608(7) | 0.162(3) | 0.110(13) |
| O | 0.1232(16) | 0.477(5) | 0.1509(12) | 0.110(13) |
| O | 0.285(2) | 0.108(7) | 0.136(3) | 0.110(13) |
| O | 0.360(3) | 0.319(4) | 0.5001(9) | 0.110(13) |
| O | 0.4388(16) | 0.972(4) | 0.384(2) | 0.110(13) |
| O | 0.5082(16) | 0.472(4) | 0.384(2) | 0.110(13) |
| O | 0.372(3) | 0.341(3) | 0.6930(14) | 0.110(13) |
| O | 0.4907(15) | 0.471(4) | 0.870(2) | 0.110(13) |
| O | 0.667(3) | 0.330(5) | 0.0139(12) | 0.110(13) |
| O | 0.285(3) | 0.208(5) | 0.8519(15) | 0.110(13) |
| O | 0.2845(17) | 0.708(5) | 0.7968(12) | 0.110(13) |
| O | 0.8883(16) | 0.389(5) | 0.1147(16) | 0.110(13) |
| O | 0.0196(17) | 0.269(7) | 0.9806(18) | 0.110(13) |
| C | 0.095(5) | 0.484(15) | 0.690(4) | 0.00(2) |
| C | 0.628(5) | 0.274(15) | 0.473(4) | 0.003(19) |
| C | 1.001(8) | 0.35(2) | 0.517(8) | 0.08(3) |
| C | 1.069(5) | 0.484(14) | 0.430(5) | 0.000(19) |
| C | 0.875(5) | 0.532(17) | 0.619(4) | 0.00(2) |
| C | 0.214(16) | 0.23(5) | 0.533(15) | 0.24(9) |
| C | 0.963(14) | 0.57(4) | 0.706(11) | 0.16(6) |

**Table 4.3.** Dynamical Scattering Refinement of Reflections from 3 Principle Zone Axes.

| Zone | # of Unique Reflections | Sample Thickness for Minimized R-value | $R_F$ |
|---|---|---|---|
| [001] | 14 | 55 nm | 0.224 |
| [100] | 14 | 67 nm | 0.199 |
| [010] | 105 | 25 nm | 0.241 |
| 3 Zone $R_F$ | 133 | | 0.232 |

A

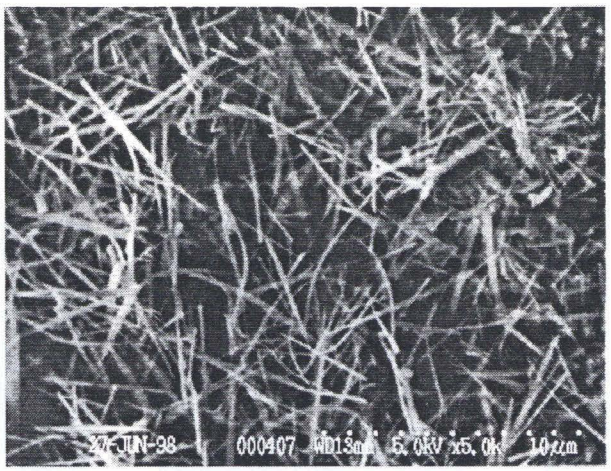

B

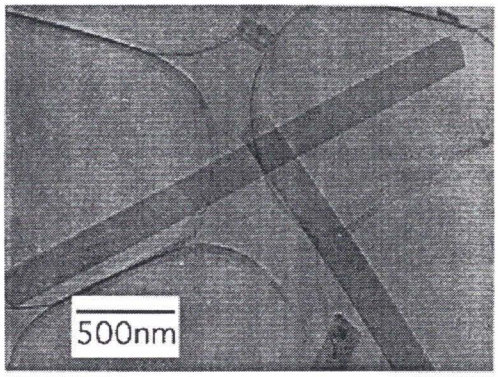


**Figure 4.1.** Scanning electron micrographs (a) and low resolution transmission electron micrograph (b) of as-made SSZ-48 crystals.

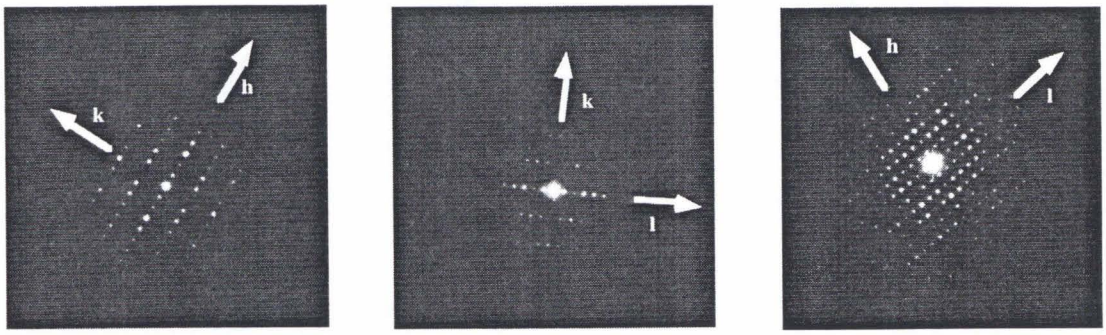


[001] [100] [010]

**Figure 4.2.** Experimental electron diffraction data from 3 principle zone axes of SSZ-48.

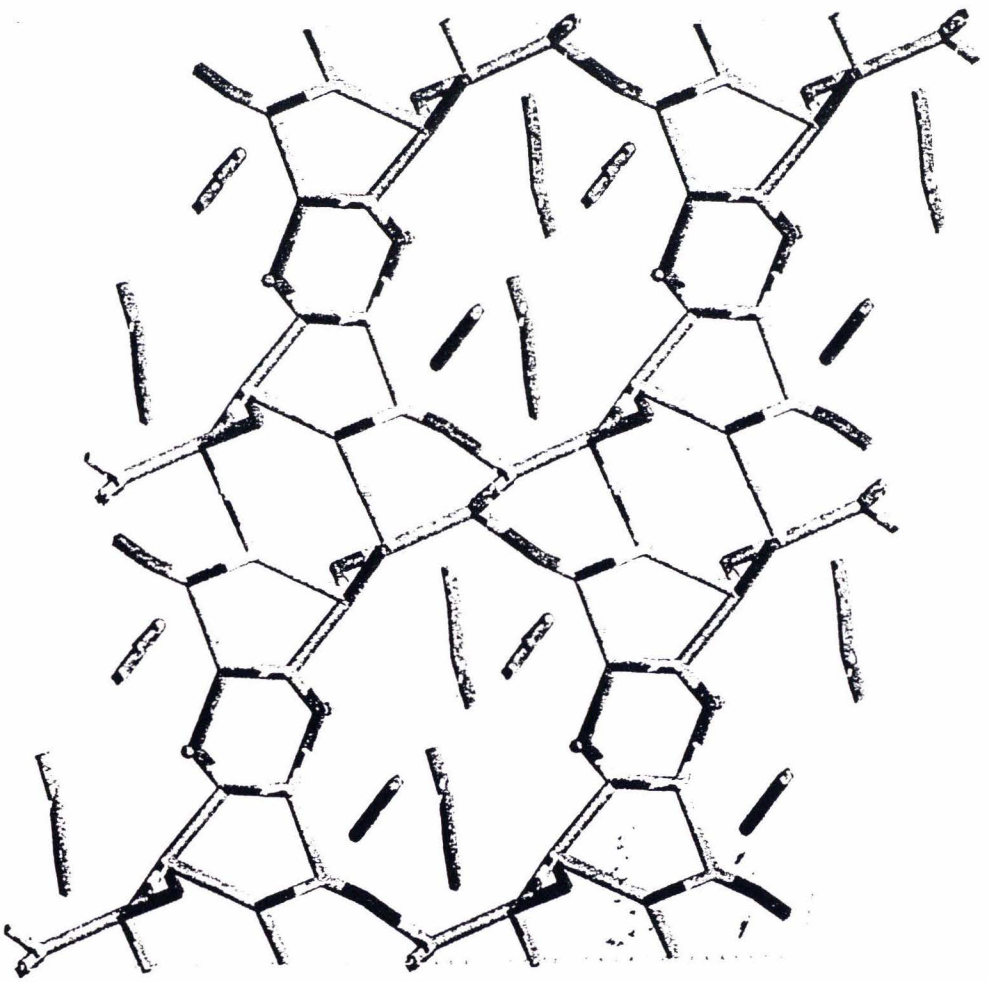

**Figure 4.3.** Model of SSZ-48 crystal structure obtained from electron diffraction structure solution.

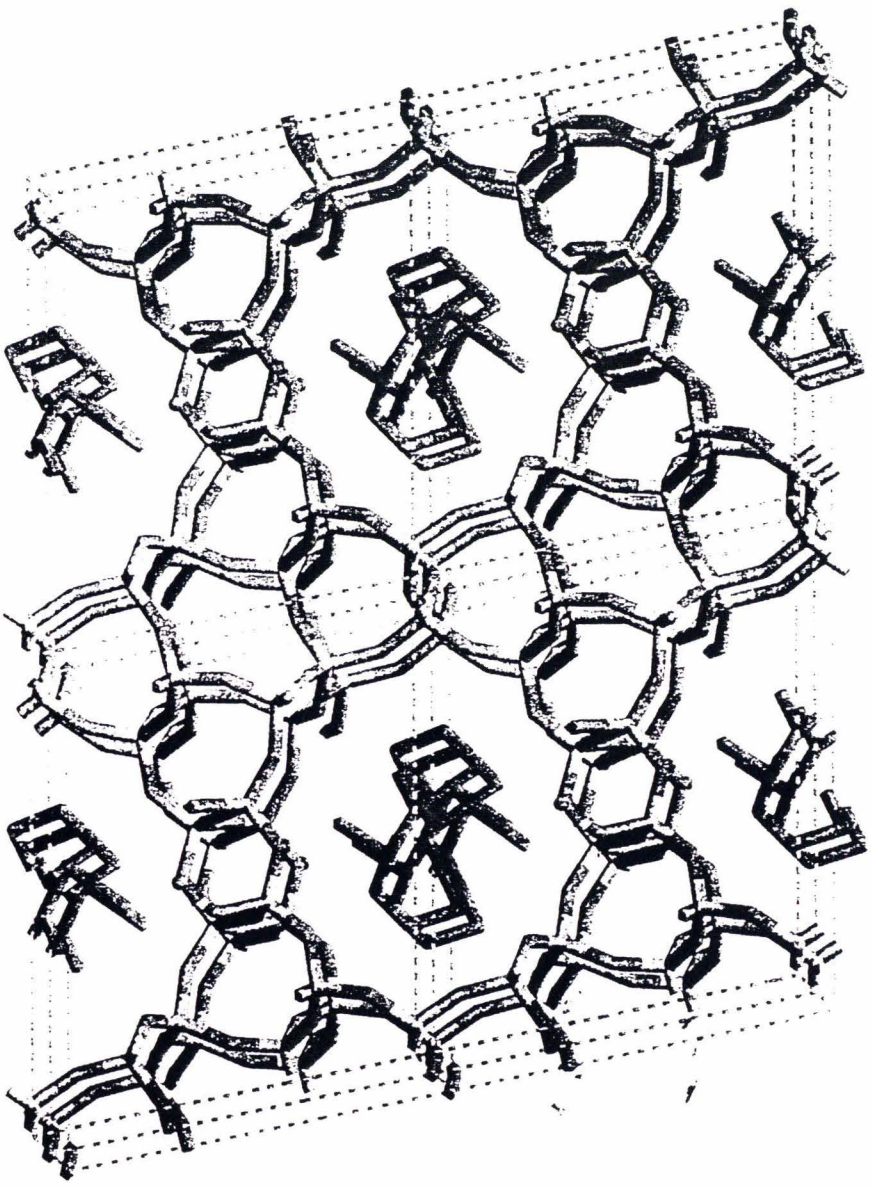

**Figure 4.4.** Model of SSZ-48 crystal structure obtained from electron diffraction refinement.

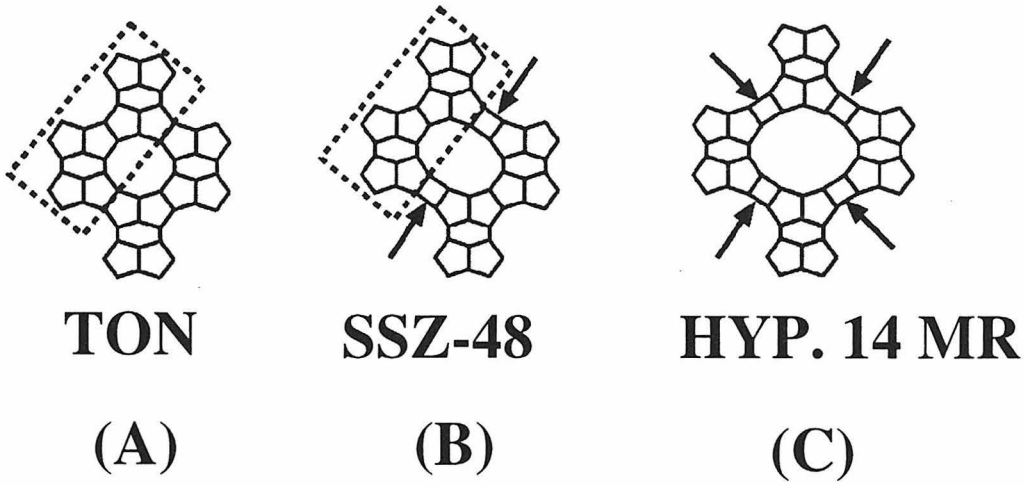


**Figure 4.5.** Illustraton of the relationship between the TON (a) SSZ-48 (b) and the hyptothetical 14 MR (c) structures through the 4 mr expansion of the $[5^4.6^1]$ units.

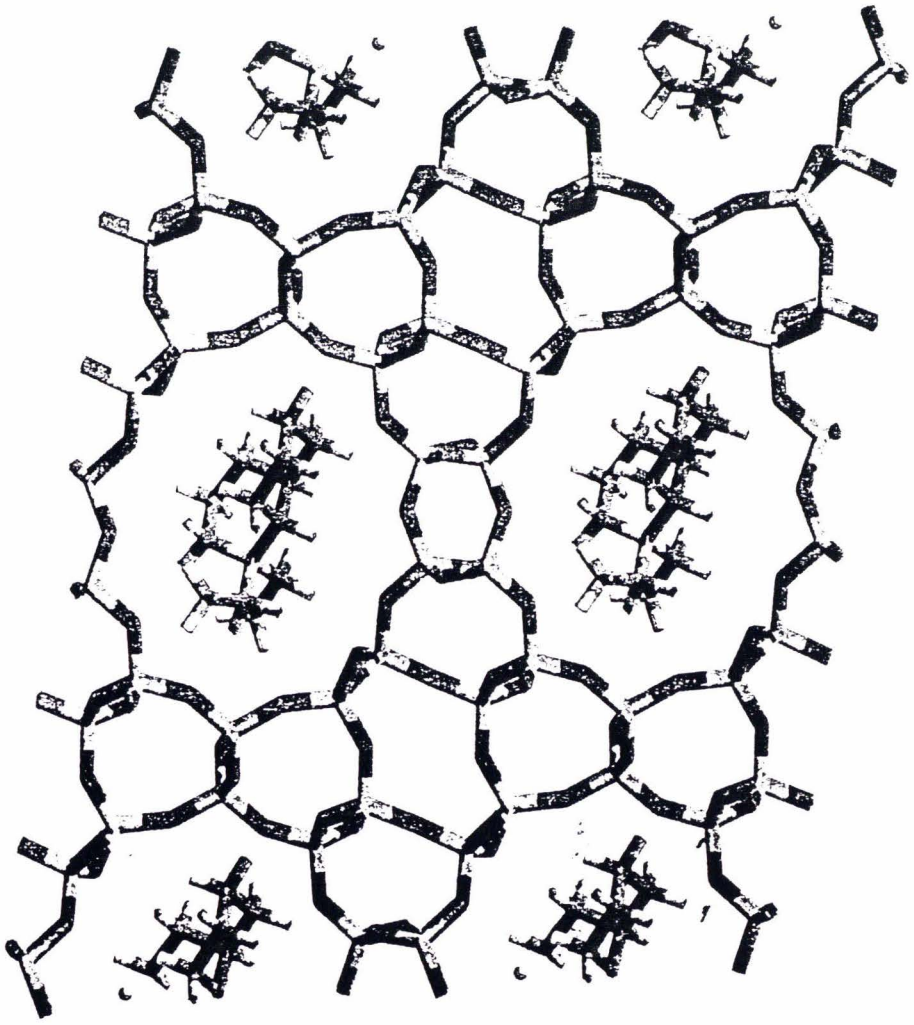

**Figure 4.6.** Energy minimized model of the structure directing agent, *N,N*-diethyldecahydroquinolinium, occluded within the pores of the SSZ-48 framework structure.

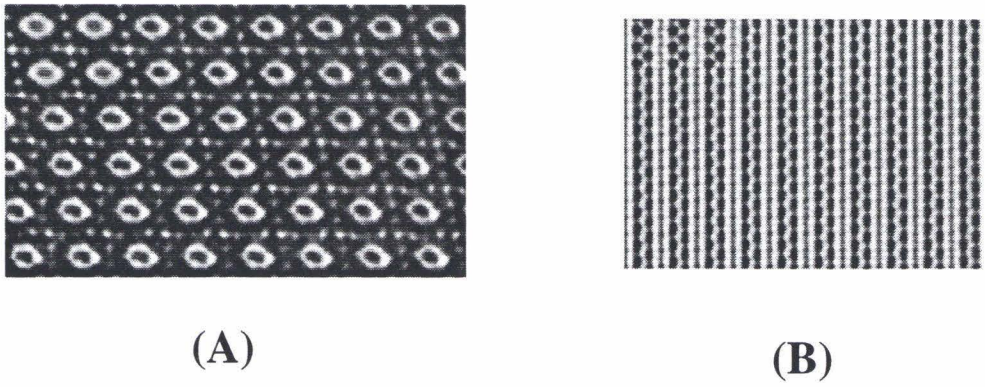


**Figure 4.7.** Fourier filtered experimental high-resolution transmission electron micrographs of SSZ-48 parallel to the pore direction , [010] (a) and perpendicular to the pore direction [001] (b). Simulated high resolution images are inset into the upper left hand corner of each of the experimental images.

## Supplementary Material Index for Chapter 4

## Chapter 4 Supplementary Material

1. h,k,l, observed and calculated structure factors from SHELX refinement.

| Point | h | k | l | Fc | Fo |
|---|---|---|---|---|---|
| 0 | 0 | - 4 | 0 | 3.87169 | 5.65685 |
| 1 | 0 | - 2 | 0 | 25.4008 | 21.8293 |
| 2 | 1 | - 2 | 0 | 14.6901 | 8.60581 |
| 3 | 2 | - 2 | 0 | 8.62612 | 5.92537 |
| 4 | 3 | - 2 | 0 | 9.93076 | 12.508 |
| 5 | 4 | - 2 | 0 | 1.51987 | 6.59848 |
| 6 | 1 | - 1 | 0 | 12.8016 | 18.3175 |
| 7 | 2 | - 1 | 0 | 5.20865 | 14.7292 |
| 8 | 3 | - 1 | 0 | 6.3498 | 8.18046 |
| 9 | 4 | - 1 | 0 | 6.77938 | 8.16088 |
| 10 | 5 | - 1 | 0 | 6.92098 | 8.83855 |
| 11 | 6 | - 1 | 0 | 3.68375 | 3.65923 |
| 12 | 1 | 0 | 0 | 18.6893 | 15.6649 |
| 13 | 2 | 0 | 0 | 4.32782 | 11.1692 |
| 14 | 3 | 0 | 0 | 31.8145 | 28.4786 |
| 15 | 4 | 0 | 0 | 1.94422 | 16.4018 |
| 16 | 5 | 0 | 0 | 2.98496 | 7.61249 |
| 17 | 7 | 0 | 0 | 0.264575 | 7.11266 |
| 18 | 8 | 0 | 0 | 7.51997 | 5.57674 |
| 19 | 1 | 1 | 0 | 12.8016 | 19.6 |
| 20 | 2 | 1 | 0 | 5.20865 | 13.7055 |
| 21 | 3 | 1 | 0 | 6.3498 | 9.11537 |
| 22 | 4 | 1 | 0 | 6.77938 | 7.19236 |
| 23 | 5 | 1 | 0 | 6.92098 | 9.49789 |
| 24 | 6 | 1 | 0 | 3.68375 | 3.45543 |
| 25 | 0 | 2 | 0 | 25.4008 | 22.7115 |
| 26 | 1 | 2 | 0 | 14.6901 | 10.4231 |
| 27 | 2 | 2 | 0 | 8.62612 | 6.59621 |
| 28 | 3 | 2 | 0 | 9.93076 | 12.8666 |
| 29 | 4 | 2 | 0 | 1.51987 | 3.90768 |
| 30 | 0 | 4 | 0 | 3.87169 | 6.98785 |
| 31 | - 2 | - 3 | 1 | 4.69681 | 6.29285 |
| 32 | - 1 | - 3 | 1 | 6.67083 | 7.51199 |
| 33 | - 3 | - 2 | 1 | 7.76531 | 6.95557 |
| 34 | - 2 | - 2 | 1 | 3.82884 | 10.6621 |
| 35 | - 1 | - 2 | 1 | 5.07543 | 7.01641 |
| 36 | 0 | - 2 | 1 | 7.20972 | 7.88543 |
| 37 | 1 | - 2 | 1 | 11.6009 | 15.8874 |
| 38 | 2 | - 2 | 1 | 3.56511 | 4.99199 |
| 39 | - 6 | - 1 | 1 | 3.96611 | 3.29545 |
| 40 | - 5 | - 1 | 1 | 4.99199 | 6.12862 |
| 41 | - 4 | - 1 | 1 | 15.9794 | 16.1802 |
| 42 | - 3 | - 1 | 1 | 7.54983 | 9.55353 |
| 43 | - 2 | - 1 | 1 | 22.6623 | 25.3126 |
| 44 | - 1 | - 1 | 1 | 27.4893 | 23.0983 |
| 45 | 0 | - 1 | 1 | 5.89491 | 11.6542 |
| 46 | 1 | - 1 | 1 | 6.1441 | 13.7412 |

| Point | h | k | l | Fc | Fo |
|---|---|---|---|---|---|
| 47 | 2 | - 1 | 1 | 5.77321 | 9.8585 |
| 48 | 3 | - 1 | 1 | 6.37103 | 4.50333 |
| 49 | 4 | - 1 | 1 | 9.10714 | 8.83912 |
| 50 | 5 | - 1 | 1 | 3.09839 | 2.498 |
| 51 | 6 | - 1 | 1 | 4.08779 | 1.76635 |
| 52 | 7 | - 1 | 1 | 3.2573 | 2.39792 |
| 53 | - 8 | 0 | 1 | 4.3359 | 6.22575 |
| 54 | - 6 | 0 | 1 | 5.30094 | 7.62758 |
| 55 | - 5 | 0 | 1 | 3.93319 | 4.3382 |
| 56 | - 4 | 0 | 1 | 11.887 | 6.55668 |
| 57 | - 3 | 0 | 1 | 15.1697 | 22.1585 |
| 58 | - 2 | 0 | 1 | 15.2715 | 19.9156 |
| 59 | - 1 | 0 | 1 | 15.9097 | 10.7149 |
| 60 | 1 | 0 | 1 | 11.1844 | 14.3944 |
| 61 | 2 | 0 | 1 | 20.3728 | 22.5342 |
| 62 | 3 | 0 | 1 | 12.0545 | 16.8502 |
| 63 | 4 | 0 | 1 | 8.70747 | 7.76724 |
| 64 | 5 | 0 | 1 | 4.23084 | 10.5641 |
| 65 | 6 | 0 | 1 | 3.96106 | 3.2078 |
| 66 | 7 | 0 | 1 | 2.69444 | 2.35797 |
| 67 | 8 | 0 | 1 | 1.89473 | 2.55734 |
| 68 | - 7 | 1 | 1 | 2.28254 | 2.69258 |
| 69 | - 6 | 1 | 1 | 3.96611 | 3.10161 |
| 70 | - 5 | 1 | 1 | 4.99199 | 6.22013 |
| 71 | - 4 | 1 | 1 | 15.9794 | 16.122 |
| 72 | - 3 | 1 | 1 | 7.54983 | 9.70979 |
| 73 | - 2 | 1 | 1 | 22.6623 | 25.4876 |
| 74 | - 1 | 1 | 1 | 27.4893 | 21.9509 |
| 75 | 0 | 1 | 1 | 5.89491 | 15.7715 |
| 76 | 1 | 1 | 1 | 6.1441 | 14.0684 |
| 77 | 2 | 1 | 1 | 5.77321 | 9.76217 |
| 78 | 3 | 1 | 1 | 6.37103 | 4.60652 |
| 79 | 4 | 1 | 1 | 9.10714 | 7.8721 |
| 80 | 5 | 1 | 1 | 3.09839 | 2.34094 |
| 81 | 6 | 1 | 1 | 4.08779 | 2.25167 |
| 82 | 7 | 1 | 1 | 3.2573 | 2.60768 |
| 83 | - 3 | 2 | 1 | 7.76531 | 6.82495 |
| 84 | - 2 | 2 | 1 | 3.82884 | 4.8949 |
| 85 | - 1 | 2 | 1 | 5.07543 | 7.76917 |
| 86 | 1 | 2 | 1 | 11.6009 | 16.3991 |
| 87 | 2 | 2 | 1 | 3.56511 | 4.07063 |
| 88 | - 2 | 3 | 1 | 4.69681 | 6.36553 |
| 89 | - 1 | 3 | 1 | 6.67083 | 8.21279 |
| 90 | - 4 | - 3 | 2 | 5.03289 | 5.44885 |
| 91 | - 2 | - 3 | 2 | 2.8688 | 3.14484 |
| 92 | - 6 | - 2 | 2 | 3.25576 | 2.42074 |
| 93 | - 4 | - 2 | 2 | 8.26378 | 4.16293 |

| Point | h | k | l | Fc | Fo |
|---|---|---|---|---|---|
| 94 | - 3 | - 2 | 2 | 9.68814 | 8.77496 |
| 95 | - 2 | - 2 | 2 | 5.62761 | 7.21595 |
| 96 | - 1 | - 2 | 2 | 2.36643 | 2.43516 |
| 97 | 0 | - 2 | 2 | 8.91403 | 10.3571 |
| 98 | 1 | - 2 | 2 | 5.22015 | 6.39922 |
| 99 | 2 | - 2 | 2 | 4.72652 | 6.91809 |
| 100 | 3 | - 2 | 2 | 2.79821 | 1.95704 |
| 101 | 4 | - 2 | 2 | 2.44745 | 1.88944 |
| 102 | 5 | - 2 | 2 | 2.70924 | 2.29347 |
| 103 | - 4 | - 1 | 2 | 12.7538 | 19.9181 |
| 104 | - 3 | - 1 | 2 | 9.17115 | 9.02386 |
| 105 | - 2 | - 1 | 2 | 13.8033 | 8.67698 |
| 106 | - 1 | - 1 | 2 | 35.6864 | 21.4026 |
| 107 | 0 | - 1 | 2 | 13.6118 | 14.2608 |
| 108 | 1 | - 1 | 2 | 5.94475 | 17.1892 |
| 109 | 2 | - 1 | 2 | 5.58211 | 9.2844 |
| 110 | - 8 | 0 | 2 | 1.54596 | 2.10476 |
| 111 | - 7 | 0 | 2 | 0.387298 | 3.74166 |
| 112 | - 5 | 0 | 2 | 6.94694 | 6.76314 |
| 113 | - 4 | 0 | 2 | 2.78209 | 9.6535 |
| 114 | - 3 | 0 | 2 | 6.47302 | 11.7571 |
| 115 | - 2 | 0 | 2 | 13.1647 | 16.8704 |
| 116 | - 1 | 0 | 2 | 1.90788 | 14.2267 |
| 117 | 0 | 0 | 2 | 7.34234 | 10.1887 |
| 118 | 1 | 0 | 2 | 12.3122 | 18.1711 |
| 119 | 2 | 0 | 2 | 24.5328 | 21.8692 |
| 120 | 3 | 0 | 2 | 3.98748 | 5.1643 |
| 121 | 4 | 0 | 2 | 3.64005 | 9.20761 |
| 122 | 5 | 0 | 2 | 13.2129 | 10.7819 |
| 123 | 6 | 0 | 2 | 2.26495 | 2.84781 |
| 124 | 8 | 0 | 2 | 2.73496 | 3.46699 |
| 125 | - 4 | 1 | 2 | 12.7538 | 20.0307 |
| 126 | - 3 | 1 | 2 | 9.17115 | 8.74471 |
| 127 | - 2 | 1 | 2 | 13.8033 | 12.3758 |
| 128 | - 1 | 1 | 2 | 35.6864 | 19.6334 |
| 129 | 0 | 1 | 2 | 13.6118 | 16.2148 |
| 130 | 1 | 1 | 2 | 5.94475 | 16.8956 |
| 131 | 2 | 1 | 2 | 5.58211 | 9.05925 |
| 132 | - 6 | 2 | 2 | 3.25576 | 2.43516 |
| 133 | - 4 | 2 | 2 | 8.26378 | 4.58367 |
| 134 | - 3 | 2 | 2 | 9.68814 | 7.506 |
| 135 | - 2 | 2 | 2 | 5.62761 | 7.71557 |
| 136 | - 1 | 2 | 2 | 2.36643 | 2.14942 |
| 137 | 0 | 2 | 2 | 8.91403 | 10.4149 |
| 138 | 1 | 2 | 2 | 5.22015 | 4.80729 |
| 139 | 2 | 2 | 2 | 4.72652 | 4.62601 |
| 140 | 3 | 2 | 2 | 2.79821 | 3.2078 |

| Point | h | k | l | Fc | Fo |
|---|---|---|---|---|---|
| 188 | - 4 | - 3 | 4 | 1.85742 | 2.77308 |
| 189 | - 6 | - 2 | 4 | 3.50571 | 4.81041 |
| 190 | - 4 | - 2 | 4 | 2.74773 | 3.26803 |
| 191 | - 2 | - 2 | 4 | 8.25893 | 9.25419 |
| 192 | 0 | - 2 | 4 | 10.2083 | 5.42863 |
| 193 | 1 | - 2 | 4 | 4.28486 | 8.40298 |
| 194 | 2 | - 2 | 4 | 3.32265 | 3.25576 |
| 195 | - 5 | - 1 | 4 | 3.75366 | 8.24985 |
| 196 | - 4 | - 1 | 4 | 4.99099 | 6.61816 |
| 197 | - 3 | - 1 | 4 | 4.18808 | 11.513 |
| 198 | - 1 | - 1 | 4 | 13.4183 | 5.47905 |
| 199 | 0 | - 1 | 4 | 5.07346 | 4.10244 |
| 200 | 1 | - 1 | 4 | 6.21852 | 4.70319 |
| 201 | 2 | - 1 | 4 | 7.08167 | 5.39537 |
| 202 | - 8 | 0 | 4 | 0.911043 | 3.2078 |
| 203 | - 6 | 0 | 4 | 7.16938 | 6.85784 |
| 204 | - 5 | 0 | 4 | 6.80221 | 10.1237 |
| 205 | - 4 | 0 | 4 | 1.20416 | 4.43959 |
| 206 | - 3 | 0 | 4 | 10.1084 | 13.5063 |
| 207 | - 2 | 0 | 4 | 14.1785 | 18.4163 |
| 208 | - 1 | 0 | 4 | 14.655 | 20.8545 |
| 209 | 0 | 0 | 4 | 25.5065 | 25.6336 |
| 210 | 1 | 0 | 4 | 15.1202 | 17.0156 |
| 211 | 2 | 0 | 4 | 8.89888 | 13.9133 |
| 212 | 3 | 0 | 4 | 17.269 | 16.0978 |
| 213 | 5 | 0 | 4 | 8.30482 | 8.07032 |
| 214 | 6 | 0 | 4 | 3.32566 | 3.3541 |
| 215 | 8 | 0 | 4 | 2.54362 | 4.54753 |
| 216 | - 5 | 1 | 4 | 3.75366 | 9.42284 |
| 217 | - 4 | 1 | 4 | 4.99099 | 6.37024 |
| 218 | - 3 | 1 | 4 | 4.18808 | 13.6671 |
| 219 | - 1 | 1 | 4 | 13.4183 | 4.94065 |
| 220 | 1 | 1 | 4 | 6.21852 | 4.58148 |
| 221 | - 6 | 2 | 4 | 3.50571 | 7.31369 |
| 222 | - 4 | 2 | 4 | 2.74773 | 2.77849 |
| 223 | - 2 | 2 | 4 | 8.25893 | 8.40298 |
| 224 | 0 | 2 | 4 | 10.2083 | 11.4547 |
| 225 | 1 | 2 | 4 | 4.28486 | 5.07839 |
| 226 | 2 | 2 | 4 | 3.32265 | 3.75633 |
| 227 | - 4 | 3 | 4 | 1.85742 | 3.36749 |
| 228 | - 5 | - 2 | 5 | 1.42478 | 2.93939 |
| 229 | - 3 | - 2 | 5 | 2.02485 | 2.50998 |
| 230 | - 2 | - 2 | 5 | 3.11929 | 2.62488 |
| 231 | - 6 | - 1 | 5 | 4.79062 | 4.53652 |
| 232 | - 5 | - 1 | 5 | 2.80713 | 2.00998 |
| 233 | - 4 | - 1 | 5 | 3.07734 | 7.43034 |
| 234 | - 2 | - 1 | 5 | 12.0839 | 8.70287 |

| Point | h | k | l | Fc | Fo |
|---|---|---|---|---|---|
| 235 | - 1 | - 1 | 5 | 9.50894 | 14.0239 |
| 236 | 0 | - 1 | 5 | 3.94335 | 2.84781 |
| 237 | 1 | - 1 | 5 | 7.86511 | 9.73345 |
| 238 | - 5 | 0 | 5 | 4.17373 | 5.21824 |
| 239 | - 4 | 0 | 5 | 1.86279 | 2.06882 |
| 240 | - 3 | 0 | 5 | 7.0859 | 6.005 |
| 241 | - 2 | 0 | 5 | 6.67907 | 10.6151 |
| 242 | - 1 | 0 | 5 | 17.8253 | 14.985 |
| 243 | 0 | 0 | 5 | 0.974679 | 14.988 |
| 244 | 1 | 0 | 5 | 4.87955 | 7.31095 |
| 245 | 2 | 0 | 5 | 2.97153 | 4.80625 |
| 246 | 3 | 0 | 5 | 4.14005 | 2.9 |
| 247 | 5 | 0 | 5 | 5.94979 | 6.49923 |
| 248 | 6 | 0 | 5 | 0.412311 | 3.01496 |
| 249 | 7 | 0 | 5 | 0.974679 | 4.82079 |
| 250 | - 6 | 1 | 5 | 4.79062 | 5.87878 |
| 251 | - 4 | 1 | 5 | 3.07734 | 6.39531 |
| 252 | - 2 | 1 | 5 | 12.0839 | 10.424 |
| 253 | - 1 | 1 | 5 | 9.50894 | 12.9646 |
| 254 | 1 | 1 | 5 | 7.86511 | 6.27615 |
| 255 | - 5 | 2 | 5 | 1.42478 | 3.33317 |
| 256 | - 3 | 2 | 5 | 2.02485 | 1.70587 |
| 257 | - 4 | - 2 | 6 | 2.78209 | 3.31361 |
| 258 | - 1 | - 2 | 6 | 3.53977 | 5.2 |
| 259 | - 6 | - 1 | 6 | 3.98623 | 3.97744 |
| 260 | - 5 | - 1 | 6 | 4.09756 | 3.60139 |
| 261 | - 2 | - 1 | 6 | 8.16272 | 4.74974 |
| 262 | - 1 | - 1 | 6 | 7.56505 | 6.33325 |
| 263 | 0 | - 1 | 6 | 0.748331 | 3.56511 |
| 264 | - 6 | 0 | 6 | 1.57797 | 3.29848 |
| 265 | - 5 | 0 | 6 | 3.09031 | 6.56049 |
| 266 | - 4 | 0 | 6 | 5.80689 | 4.72969 |
| 267 | - 2 | 0 | 6 | 4.63357 | 4.64004 |
| 268 | - 1 | 0 | 6 | 3.9128 | 6.70895 |
| 269 | 0 | 0 | 6 | 7.08943 | 10.556 |
| 270 | 1 | 0 | 6 | 4.59891 | 4.84355 |
| 271 | 2 | 0 | 6 | 11.2619 | 15.5229 |
| 272 | 3 | 0 | 6 | 3.75633 | 6.53605 |
| 273 | 4 | 0 | 6 | 1.87883 | 7.36682 |
| 274 | 5 | 0 | 6 | 0.4 | 12.245 |
| 275 | 7 | 0 | 6 | 3.747 | 6.66033 |
| 276 | 8 | 0 | 6 | 2.37065 | 3.5327 |
| 277 | - 7 | 1 | 6 | 1.1619 | 3.85487 |
| 278 | - 6 | 1 | 6 | 3.98623 | 4.10488 |
| 279 | - 5 | 1 | 6 | 4.09756 | 2.88444 |
| 280 | - 2 | 1 | 6 | 8.16272 | 7.09436 |
| 281 | - 1 | 1 | 6 | 7.56505 | 5.18845 |

| Point | h | k | l | Fc | Fo |
|---|---|---|---|---|---|
| 282 | - 4 | 2 | 6 | 2.78209 | 2.80357 |
| 283 | - 1 | 2 | 6 | 3.53977 | 3.1257 |
| 284 | - 5 | - 2 | 7 | 2.99833 | 4.12068 |
| 285 | - 2 | - 1 | 7 | 6.65282 | 7.52263 |
| 286 | - 1 | - 1 | 7 | 5.9127 | 3.26803 |
| 287 | - 6 | 0 | 7 | 7.22634 | 4.05832 |
| 288 | - 5 | 0 | 7 | 0.640312 | 6.57419 |
| 289 | - 3 | 0 | 7 | 10.5499 | 9.86053 |
| 290 | - 2 | 0 | 7 | 3.56931 | 6.34508 |
| 291 | - 1 | 0 | 7 | 2.1095 | 2.48193 |
| 292 | 0 | 0 | 7 | 3.87556 | 7.36003 |
| 293 | 2 | 0 | 7 | 4.72969 | 10.6141 |
| 294 | 3 | 0 | 7 | 5.9607 | 5.90169 |
| 295 | 5 | 0 | 7 | 7.86829 | 6.93542 |
| 296 | - 2 | 1 | 7 | 6.65282 | 6.87968 |
| 297 | - 5 | 2 | 7 | 2.99833 | 2.82135 |
| 298 | - 3 | 0 | 8 | 2.40208 | 5.73934 |
| 299 | - 2 | 0 | 8 | 1.80831 | 5.83609 |
| 300 | - 1 | 0 | 8 | 1.73781 | 6.7164 |
| 301 | 0 | 0 | 8 | 2.995 | 4.4699 |
| 302 | 1 | 0 | 8 | 9.28386 | 8.98165 |
| 303 | 4 | 0 | 8 | 1.23288 | 3.55246 |
| 304 | 6 | 0 | 8 | 1.18743 | 2.52784 |
| 305 | - 4 | 0 | 9 | 0.387298 | 2.8931 |
| 306 | - 3 | 0 | 9 | 2.93598 | 4.96588 |
| 307 | - 2 | 0 | 9 | 0.969536 | 8.39583 |
| 308 | 0 | 0 | 9 | 2.90172 | 4.98598 |
| 309 | 1 | 0 | 9 | 2.77308 | 2.72764 |
| 310 | 4 | 0 | 9 | 1.13137 | 5.25547 |
| 311 | 6 | 0 | 9 | 1.04881 | 3.05287 |
| 312 | 7 | 0 | 9 | 1.07703 | 5.21824 |
| 313 | - 4 | 1 | 9 | 6.39609 | 8.08888 |
| 314 | - 5 | 0 | 10 | 0.2 | 4.94975 |
| 315 | - 1 | 0 | 10 | 3.59583 | 6.9 |
| 316 | 0 | 0 | 10 | 5.98582 | 6.31189 |
| 317 | 2 | 0 | 10 | 2.23607 | 4.71911 |
| 318 | 3 | 0 | 10 | 0.538516 | 6.53223 |
| 319 | 4 | 0 | 10 | 1.85742 | 2.498 |
| 320 | 5 | 0 | 10 | 0.8544 | 2.20907 |
| 321 | - 3 | 0 | 11 | 1.99499 | 4.01871 |
| 322 | - 1 | 0 | 11 | 2.64575 | 2.7 |
| 323 | 3 | 0 | 11 | 1.90526 | 2.21585 |
| 324 | 0 | 0 | 12 | 2.20454 | 5.68331 |
| 325 | - 3 | 0 | 13 | 2.34521 | 3.42345 |

## Chapter 4 Supplementary Material

2. h,k,l, observed and calculated structure factors (based on simulations of dynamical diffraction effects using energy minimized SDA-SSZ-48 system) for [100], [010], and [001] zones.

| Point | h | k | l | Fo | Fs |
|---|---|---|---|---|---|
| 0 | 0 | 0 | 4 | 37.2156 | 30.9101 |
| 1 | 0 | 0 | 6 | 68.1542 | 56.8984 |
| 2 | 0 | 0 | 8 | 93.6483 | 85.9318 |
| 3 | 0 | 0 | 10 | 54.7723 | 45.8358 |
| 4 | 0 | 0 | 12 | 38.6005 | 43.5106 |
| 5 | 0 | 0 | 14 | 27.0278 | 25.8175 |
| 6 | 0 | 0 | 18 | 19.8997 | 21.9096 |
| 7 | 0 | 0 | 20 | 24.7689 | 16.7059 |
| 8 | 1 | 0 | 0 | 57.2713 | 68.5931 |
| 9 | 1 | 0 | 2 | 52.5357 | 52.4408 |
| 10 | 1 | 0 | 4 | 66.3702 | 57.2324 |
| 11 | 1 | 0 | 6 | 15.7003 | 33.318 |
| 12 | 1 | 0 | 8 | 62.0886 | 58.0355 |
| 13 | 1 | 0 | - 2 | 39.1152 | 64.9852 |
| 14 | 1 | 0 | - 4 | 51.9134 | 46.9016 |
| 15 | 1 | 0 | - 6 | 40.1871 | 42.134 |
| 16 | 1 | 0 | - 8 | 76.2561 | 54.0768 |
| 17 | 1 | 0 | 10 | 27.3861 | 31.8259 |
| 18 | 1 | 0 | 12 | 17.7059 | 15.7918 |
| 19 | 1 | 0 | 16 | 32.7872 | 23.6258 |
| 20 | 1 | 0 | -10 | 54.8635 | 50.9316 |
| 21 | 1 | 0 | -12 | 25 | 36.7753 |
| 22 | 1 | 0 | -16 | 24.5764 | 18.6249 |
| 23 | 1 | 0 | -20 | 26.467 | 29.8754 |
| 24 | 2 | 0 | 0 | 40.8044 | 15.7089 |
| 25 | 2 | 0 | 2 | 82.2192 | 61.4536 |
| 26 | 2 | 0 | 4 | 79.8123 | 70.9541 |
| 27 | 2 | 0 | 6 | 102.47 | 90.6651 |
| 28 | 2 | 0 | 8 | 50.8429 | 50.7629 |
| 29 | 2 | 0 | - 2 | 72.6636 | 48.1986 |
| 30 | 2 | 0 | - 4 | 78.9303 | 67.7142 |
| 31 | 2 | 0 | - 6 | 62.2495 | 51.3813 |
| 32 | 2 | 0 | - 8 | 67.1937 | 40.2975 |
| 33 | 2 | 0 | 10 | 17.5357 | 8.50879 |
| 34 | 2 | 0 | 14 | 38.7298 | 42.7849 |
| 35 | 2 | 0 | 20 | 17.6068 | 16.1313 |
| 36 | 2 | 0 | -14 | 23.5584 | 36.69 |
| 37 | 2 | 0 | -16 | 21.8975 | 26.158 |
| 38 | 2 | 0 | -18 | 31.7884 | 24.1557 |
| 39 | 3 | 0 | 0 | 103.923 | 85.1359 |
| 40 | 3 | 0 | 2 | 61.4817 | 61.0535 |
| 41 | 3 | 0 | 4 | 18.9077 | 29.6512 |
| 42 | 3 | 0 | 6 | 82.9156 | 72.754 |
| 43 | 3 | 0 | 8 | 58.8218 | 44.1196 |
| 44 | 3 | 0 | - 2 | 80.8703 | 75.7967 |
| 45 | 3 | 0 | - 4 | 42.9535 | 51.6192 |
| 46 | 3 | 0 | - 6 | 71.0282 | 62.0049 |

| Point | h | k | l | Fo | Fs |
|---|---|---|---|---|---|
| 47 | 3 | 0 | -8 | 49.4975 | 45.6483 |
| 48 | 3 | 0 | 12 | 23.8642 | 32.1451 |
| 49 | 3 | 0 | 14 | 21.9203 | 31.5552 |
| 50 | 3 | 0 | 20 | 26.0768 | 19.222 |
| 51 | 3 | 0 | -10 | 21.9089 | 19.9518 |
| 52 | 3 | 0 | -12 | 28.9482 | 34.6481 |
| 53 | 3 | 0 | -14 | 36.2629 | 40.8511 |
| 54 | 3 | 0 | -16 | 22.7925 | 18.0533 |
| 55 | 3 | 0 | -18 | 18.9605 | 21.8412 |
| 56 | 4 | 0 | 0 | 59.7495 | 56.2244 |
| 57 | 4 | 0 | 2 | 28.3461 | 56.6586 |
| 58 | 4 | 0 | 4 | 33.6898 | 46.5958 |
| 59 | 4 | 0 | 6 | 23.7171 | 37.3702 |
| 60 | 4 | 0 | -2 | 24.3311 | 48.379 |
| 61 | 4 | 0 | -4 | 35.2846 | 56.4419 |
| 62 | 4 | 0 | -6 | 11.3358 | 30.5557 |
| 63 | 4 | 0 | -8 | 13.8924 | 15.353 |
| 64 | 4 | 0 | 12 | 26.8794 | 27.7883 |
| 65 | 4 | 0 | 16 | 12.9615 | 18.8501 |
| 66 | 4 | 0 | 18 | 19.2484 | 20.2027 |
| 67 | 4 | 0 | -12 | 17.6918 | 24.4136 |
| 68 | 4 | 0 | -18 | 10.8628 | 17.2512 |
| 69 | 5 | 0 | 0 | 28.6967 | 30.8881 |
| 70 | 5 | 0 | 2 | 39.0512 | 35.7046 |
| 71 | 5 | 0 | 4 | 40 | 32.4863 |
| 72 | 5 | 0 | 6 | 62.2093 | 52.9061 |
| 73 | 5 | 0 | 8 | 29.4618 | 34.0935 |
| 74 | 5 | 0 | -2 | 15.906 | 29.8024 |
| 75 | 5 | 0 | -4 | 25.4067 | 45.6244 |
| 76 | 5 | 0 | -6 | 14.0357 | 21.4322 |
| 77 | 5 | 0 | -8 | 37.9473 | 40.3515 |
| 78 | 5 | 0 | 10 | 24.0936 | 25.1876 |
| 79 | 5 | 0 | 12 | 44.7214 | 37.3775 |
| 80 | 5 | 0 | 14 | 25.4657 | 35.7922 |
| 81 | 5 | 0 | -10 | 18.4932 | 32.8406 |
| 82 | 5 | 0 | -12 | 24.3516 | 32.1027 |
| 83 | 5 | 0 | -14 | 24.6069 | 18.7342 |
| 84 | 5 | 0 | -20 | 20.445 | 22.8406 |
| 85 | 6 | 0 | 6 | 13.6931 | 20.2364 |
| 86 | 6 | 0 | 8 | 12.4298 | 27.6901 |
| 87 | 6 | 0 | -2 | 28.5657 | 42.4687 |
| 88 | 6 | 0 | -6 | 36.6742 | 41.2227 |
| 89 | 6 | 0 | -8 | 25.4067 | 35.1435 |
| 90 | 6 | 0 | -12 | 17.9304 | 17.9322 |
| 91 | 6 | 0 | -14 | 15.2971 | 26.6274 |
| 92 | 7 | 0 | 0 | 26.1438 | 30.5022 |
| 93 | 7 | 0 | -4 | 14.3003 | 34.0895 |

| Point | h | k | l | Fo | Fs |
|---|---|---|---|---|---|
| 94 | 7 | 0 | 10 | 17.8045 | 6.44383 |
| 95 | 7 | 0 | 12 | 24.8093 | 24.8118 |
| 96 | 7 | 0 | 18 | 19.1181 | 20.6822 |
| 97 | 8 | 0 | 0 | 20.3593 | 25.7065 |
| 98 | 8 | 0 | 2 | 10.7703 | 24.4359 |
| 99 | 8 | 0 | 8 | 16.6433 | 20.9568 |
| 100 | 8 | 0 | - 2 | 22.7156 | 30.6758 |
| 101 | 8 | 0 | - 6 | 12.145 | 10.9243 |
| 102 | 8 | 0 | 12 | 12.9808 | 22.685 |
| 103 | - 2 | 0 | 12 | 26.727 | 34.9843 |
| 104 | - 8 | 0 | - 6 | 16.0209 | 18.6833 |
| 105 | 1 | 2 | 0 | 105.095 | 105.109 |
| 106 | 1 | 4 | 0 | 48.4768 | 49.8258 |
| 107 | 2 | 0 | 0 | 47.6445 | 53.5376 |
| 108 | 2 | 2 | 0 | 110 | 107.61 |
| 109 | 3 | 0 | 0 | 155.403 | 141.652 |
| 110 | 3 | 2 | 0 | 46.9042 | 78.3136 |
| 111 | 3 | 4 | 0 | 69.4442 | 61.982 |
| 112 | 4 | 0 | 0 | 117.26 | 116.021 |
| 113 | 4 | 2 | 0 | 41.7731 | 68.7952 |
| 114 | 5 | 0 | 0 | 49.3964 | 42.4841 |
| 115 | 6 | 0 | 0 | 33.9116 | 41.4667 |
| 116 | 7 | 0 | 0 | 22.6826 | 35.3281 |
| 117 | 0 | 4 | 0 | 126.293 | 62.8606 |
| 118 | 1 | 0 | 0 | 81.3634 | 136.893 |
| 119 | 0 | 0 | 4 | 52.915 | 39.5425 |
| 120 | 0 | 0 | 6 | 132.288 | 98.2343 |
| 121 | 0 | 0 | 8 | 108.167 | 108.17 |
| 122 | 0 | 0 | 10 | 76.0592 | 55.1748 |
| 123 | 0 | 0 | 14 | 33.8083 | 35.8403 |
| 124 | 0 | - 2 | 2 | 57.6194 | 69.3238 |
| 125 | 0 | - 2 | 4 | 69.4622 | 70.0768 |
| 126 | 0 | - 2 | 6 | 57.836 | 57.515 |
| 127 | 0 | - 2 | 8 | 21.2485 | 34.199 |
| 128 | 0 | - 2 | 10 | 14.7139 | 44.6973 |
| 129 | 0 | - 2 | 12 | 18.735 | 17.9184 |
| 130 | 0 | - 4 | 6 | 27.1109 | 36.4074 |
| 131 | 0 | - 4 | 8 | 25.4657 | 21.4856 |
| 132 | 0 | - 4 | - 2 | 41.1096 | 34.2812 |

| Point | h | k | l | Fc | Fo |
|---|---|---|---|---|---|
| 141 | 5 | 2 | 2 | 2.70924 | 2.31733 |
| 142 | - 4 | 3 | 2 | 5.03289 | 5.25357 |
| 143 | - 2 | 3 | 2 | 2.8688 | 3.46554 |
| 144 | - 3 | - 3 | 3 | 3.34515 | 3.01164 |
| 145 | - 6 | - 2 | 3 | 4.80104 | 4.84355 |
| 146 | - 5 | - 2 | 3 | 4.6076 | 5.06853 |
| 147 | - 3 | - 2 | 3 | 8.73899 | 10.0772 |
| 148 | - 2 | - 2 | 3 | 6.07865 | 6.11801 |
| 149 | - 1 | - 2 | 3 | 9.71442 | 6.61211 |
| 150 | 0 | - 2 | 3 | 3.24191 | 5.19904 |
| 151 | 2 | - 2 | 3 | 3.83014 | 4.80833 |
| 152 | - 6 | - 1 | 3 | 3.16386 | 3.1749 |
| 153 | - 4 | - 1 | 3 | 6.36396 | 15.4561 |
| 154 | - 3 | - 1 | 3 | 13.214 | 14.6949 |
| 155 | - 2 | - 1 | 3 | 3.34066 | 7.02424 |
| 156 | - 1 | - 1 | 3 | 16.48 | 14.4796 |
| 157 | 0 | - 1 | 3 | 11.0567 | 11.6116 |
| 158 | 1 | - 1 | 3 | 8.13634 | 7.56108 |
| 159 | - 8 | 0 | 3 | 3.68511 | 3.30151 |
| 160 | - 6 | 0 | 3 | 2.65707 | 9.94535 |
| 161 | - 5 | 0 | 3 | 6.92748 | 3.82492 |
| 162 | - 4 | 0 | 3 | 2.70555 | 3.10161 |
| 163 | - 3 | 0 | 3 | 7.50666 | 18.0147 |
| 164 | - 2 | 0 | 3 | 18.0613 | 17.0552 |
| 165 | - 1 | 0 | 3 | 11.975 | 10.9339 |
| 166 | 0 | 0 | 3 | 20.9516 | 18.6759 |
| 167 | 1 | 0 | 3 | 3.94842 | 4.30349 |
| 168 | 2 | 0 | 3 | 26.9462 | 28.0838 |
| 169 | 3 | 0 | 3 | 20.8255 | 22.7249 |
| 170 | 4 | 0 | 3 | 4.51774 | 6.44981 |
| 171 | 5 | 0 | 3 | 5.76368 | 17.0423 |
| 172 | 6 | 0 | 3 | 2.58844 | 3.62905 |
| 173 | 8 | 0 | 3 | 2.00998 | 4.07431 |
| 174 | - 6 | 1 | 3 | 3.16386 | 3.39411 |
| 175 | - 4 | 1 | 3 | 6.36396 | 14.8105 |
| 176 | - 3 | 1 | 3 | 13.214 | 12.7984 |
| 177 | - 2 | 1 | 3 | 3.34066 | 6.71714 |
| 178 | - 1 | 1 | 3 | 16.48 | 13.9875 |
| 179 | 0 | 1 | 3 | 11.0567 | 15.4638 |
| 180 | 1 | 1 | 3 | 8.13634 | 6.52457 |
| 181 | - 6 | 2 | 3 | 4.80104 | 4.8775 |
| 182 | - 5 | 2 | 3 | 4.6076 | 8.60639 |
| 183 | - 3 | 2 | 3 | 8.73899 | 10.7121 |
| 184 | - 2 | 2 | 3 | 6.07865 | 5.40463 |
| 185 | - 1 | 2 | 3 | 9.71442 | 7.08378 |
| 186 | 2 | 2 | 3 | 3.83014 | 4.19166 |
| 187 | - 3 | 3 | 3 | 3.34515 | 3.52846 |

# CHAPTER FIVE

# Guest/Host Interaction Study I: Silica Molecular Sieve Syntheses Using Sparteine Related Compounds as Structure Directing Agents

Reprinted with permission from:

[K. Tsuji, P. Wagner and M. E. Davis "Silica Molecular Sieve Syntheses Using the Sparteine Related Compounds as Structure Directing Agents" Microporous and Mesoporous Materials, *in press*]

Abstract

Three quaternary ammonium compounds are synthesized from sparteine and their performances in high-silica molecular sieve syntheses investigated. N(1)-Methyl-α-isosparteinium (compound **A**) is found to from the pure-silica molecular sieve with the CFI topology that was first synthesized with its diastereomer N(16)-methylsparteinium (**B**). The crystallization time for the synthesis of pure-silica CFI using **A** as an organic agent is shorter than that with **B**. The crystal size of the product obtained with **A** is much smaller than that recovered when using **B**. These results indicate that **A** is a better structure-directing agent for the formation of the CFI than **B**. Molecular modeling studies suggest that the reason **A** is a better structure-directing agent for CFI than **B** is that **A** can form greater number of van der Waals interactions with the silica framework of CFI. The very rigid and bulky compound, N(1),N'(16)-endo-methylenesparteinium (compound **C**) does not yield any crystalline molecular sieves over a range of the reaction conditions. The lack of success with **C** could be due to its decreased hydrophobicity and hydrothermal stability compared to **A** and **B**.

Introduction

There continues to be a strong demand for new high-silica zeolites or molecular sieves that have novel structures in order to improve chemical processes that involve catalysis and separations. Zeolitic structures containing extra-large pore systems are of great interest [1]. A topology with chirality would also be very attractive for the use in enantio-selective catalysis or racemic compound separation. One method for obtaining new structures is via the use of organic structure-directing agents (SDA). Davis and Zones point out that the rigidity of the organic molecule is one of the desired features to direct the formation of novel zeolitic structures [2]. Davis and Lobo predict that a material with chiral topology might be obtained by using a chiral organic molecule as a templating agent [3]. Sparteine is one of the natural alkaloids and is a very rigid, chiral

molecule. Thus, it fulfills some of the desired features that are speculated to be necessary to direct the formation of molecular sieves with unique structures. Nakagawa [4] and Lobo and Davis [5] succeeded in utilizing the sparteine related compound N(16)-methylsparteinium as a structure-directing agent to synthesize the high-silica molecular sieve with the AFI topology. Wagner et al. followed this work with the synthesis of CIT-5 (CFI) that is a high-silica molecular sieve with a 14-membered ring pore [6-8]. A large literature exists on the structures and syntheses of sparteine related compounds [9,10]. Here, we focused on two additional quaternary compounds as potential structure-directing agents among the reported sparteine compounds; N(1)-methyl-α-isosparteinium (compound **A**) that is the diastereomer of N(16)-methylsparteinium (compound **B**) and N(1),N'(16)-endo-methylenesparteinium (compound **C**). The crystal structures of **B** and **C** are known [10,11] and interestingly, the location of the N-alkyl groups are different from each other, i.e., the N-methyl group of **A** and N,N'-methylene group of **C** are in the endo position (or two nitrogens are in cisoid orientation), i.e., surrounded by the sparteinium skeleton, whereas the N-methyl of **B** is in the exo position (transoid orientation) and located at the outer surface of sparteinium skeleton (Scheme 1). Additionally **A** and **B** are monoquaternary ammonium cations while **C** is diquaternary ammonium compound:

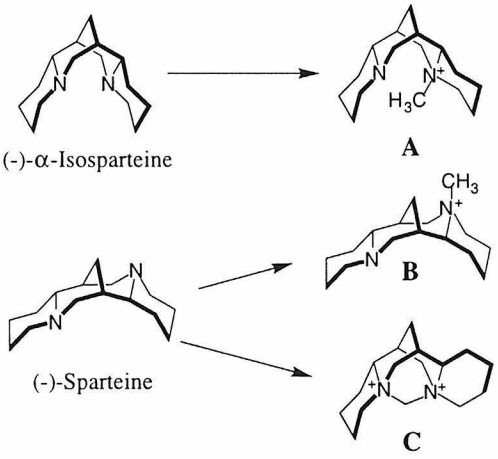


Scheme 1

Here, we report high-silica molecular sieve syntheses using the sparteine related compounds **A** and **C**, and the results are compared to those of **B** in order to investigate the structure-directing effect of these compounds.

Experimental Section

Syntheses of organic compounds . N(1)-methyl-isosparteinium iodide(**A**-iodide): α-Isosparteine was synthesized by the method reported by Leonard et al. [12,13 ] and methylated with iodomethane.

(-)-Sparteine (Aldrich, 58.7g) was dissolved in 4% acetic acid aqueous solution (450ml) and the resultant solution was added to a flask containing mercuric acetate (Aldrich, 640g). The mixture was heated to 80~90°C for 4h under nitrogen atmosphere with mechanical stirring. The cooled reaction mixture was filtered and an excess amount of hydrogen sulfide was blown into the filtrate until the whole mixture became black. The precipitate was removed by centrifuging and sulfuric acid (52g) was added. The resultant solution was evaporated until an oil is obtained. Methanol (100ml) was added and evaporated. Again, methanol was added and the methanol-insoluble (-)-$\Delta^{5,11}$-didehydrosparteine bisulfate was obtained by filtration (yield 35%). The free amine ((-)-$\Delta^{5,11}$-didehydrosparteine) was obtained by alkalization, ether extraction and evaporation (yield 94%). To (-)-$\Delta^{5,11}$-didehydrosparteine (19.1g) was added 96% formic acid (17.7g) dropwise. The reaction mixture was heated at 60°C for 2h and 10% HCl (80ml) was added. The resultant solution was basified with 20% NaOH (80ml) and a free amine was extracted with ether. The combined organic layers were dried over sodium sulfate, filtered and evaporated to give α-isosparteine as a yellowish solid. Iodomethane (Aldrich, 14.5ml) was added to the α-isosparteine

(18.2g) in ethylacetate (200ml) and stirred for 5 days at room temperature. The precipitate was recovered by filtration and recrystallized from 2-propanol three times (yield 49%). $^{13}C$ NMR spectrum of **A**-iodide in $CDCl_3$ has peaks at 20.8, 22.3, 24.9, 25.1, 25.8, 30.1, 34.6, 35.5, 36.0, 45.9, 52.7, 55.8, 63.5, 65.6, 69.3 and 74.0 ppm and is basically identical to the previous report [14].

Anal. Calcd. for $C_{16}H_{29}N_2I$: C, 51.06; H, 7.77; N, 7.44; I, 33.72. Found: C, 51.04; H, 8.02; N, 7.52; I, 34.30.

N(16)-methyl-sparteinium iodide(**B**-iodide): N-methylsparteinium iodide was synthesized by the procedure reported previously [5]. The recrystallization was carried out three times from 2-propanol.

N(1),N'(16)-endo-methylenesparteinium diiodide(**C**-diiodide): Diiodomethane (20ml (250mmol) Aldrich) was added dropwise to the sparteine (23.5g (100mmol) Aldrich) in 1-propanol (500ml) and heated under reflux for 13h. After cooling to room temperature, the appeared precipitate was recovered by filtration and washed with 2-propanol and dried under vacuum to obtain 33.1g yellow solid (yield 66%). Recrystallization was carried out from methanol. $^{13}C$ NMR spectrum of C-diiodide in $D_2O$ has peaks at 18.1, 19.0, 20.7, 21.0, 23.2, 23.5, 24.6, 30.4, 30.5, 49.7, 62.8, 63.8, 67.8, 70.4, 70.5 and 73.4 ppm.

Anal. Calcd. for $C_{16}H_{28}N_2I_2$: C, 38.28; H, 5.62; N, 5.58; I, 50.54. Found: C, 38.30; H, 5.89; N, 5.58; I, 48.79.

Anion exchange from iodide to hydroxide. The aforementioned organic halides were anion exchanged into their hydroxide forms using an anion exchange resin (Bio Rad 1-X8: OH form). For the case of **C**, the use of the resin resulted in the

decomposition of the compound so $Ag_2O$ was used instead of resin. The concentration of the resultant organic hydroxides were determined by HCl titration.

Molecular sieve synthesis. Pure-silica molecular sieve syntheses using **A** and **B** were carried out with reaction mixtures of composition 0.2 $R^+(OH^-)$/ 1 $SiO_2$/ x LiOH/ 40$H_2O$ where $R^+(OH^-)$ is the organic cation, x = 0 or 0.1 and a colloidal silica (Snowtex 40, Nissan Chemical) was used as a silica source. Borosilicate molecular sieve syntheses using **A** and **B** were carried out with reaction mixtures of composition 0.2 $R^+(OH^-)$/ 1 $SiO_2$/ 0.02 $B_2O_3$/ 0.1 NaOH/ 40$H_2O$ and a fumed silica (Cab-O-Sil, M-5) was used as a silica source. An as-synthesized borosilicate analogue of zeolite beta was used as seed (seed/ $SiO_2$=0.03) in some experiments. High-silica molecular sieve syntheses using **C** were carried out at various reaction conditions using colloidal silica, fumed silica or tetraethylorthosilicate (TEOS) as a silica source. The syntheses in hydroxide media were performed statically in sealed, pure-silica tubes at 120-175°C. Products were recovered by filtration, washed with water and acetone and dried at room temperature.

Analytical procedure. X-ray powder diffraction (XRD) patterns were collected on a Scintag XDS 2000 diffractometer equipped with a liquid-nitrogen cooled Ge detector using Cu-K$\alpha$ radiation.

Thermogravimetric analyses (TGA) were carried out on a Du Pont 951 thermogravimetric analyzer. The samples were heated in air and the temperature ramp was 10°C/min.

Raman spectra were recorded on a Nicolet System 950 Raman Spectrometer.

Solution NMR spectra of organic compounds were recorded on a General Electric QE300 spectrometer.

Scanning electron microscopy (SEM) images were recorded on a Camscan 2-LV scanning electron microscope operating with an accelerating voltage of 15 kV.

Phase Transfer Phase transfer value of iodide salts of **A**, **B** and **C** were determined by the method reported by Kubota et al. [15].

Molecular modeling calculations. The molecular modeling calculations were performed using the Open Force Field module of Cerius$^2$ [16]. The conformations of the rigid CIT-5 structure-directing agents **A** and **B** used in this study were obtained from the published single crystal structures [11,17]. The unit cell parameters for the as-synthesized **A**-CFI and **B**-CFI were obtained by refining the powder X-ray data (a=13.800 Å, b=5.03 Å, and c=25.436 Å) [18].

The calculations were carried out by first conducting sorption simulations at a fixed loading of 1 SDA molecule/unit cell. The sorption simulation probed 50000 SDA/ zeolite configurations and the lowest energy configuration was energy minimized using the Burchart-Universal force field. The framework atoms were fixed during the energy minimization and the coulomb terms of the non-bonded energy calculations were ignored. The calculated stabilization energy represents the non-bonded van der Waals interactions between the framework and the SDA.

## Results and discussion

Results of syntheses using N(1)-methyl-α-isosparteinium (**A**) as a SDA are given in Table 1. As shown by the data in Table 1, the products synthesized using **A** as an organic agent are the same as with **B**, i.e., the molecular sieves obtained with **A** are the

CFI and AFI. Although several other reaction conditions were explored (not shown here), the products obtained by using **A** and **B** are basically the same (include dense phases and amorphous materials). The amounts of incorporated organic in the as-synthesized materials are slightly different. The product synthesized with **A** has more organic than the product obtained by **B** in both CFI and AFI (Table 1). This trend is clearer for the case of as-synthesized CFI; CFI synthesized with **A** has about 8% more organic than the CFI with **B**. Figure 1 compares the Raman spectra of the as-synthesized, pure-silica molecular sieves with the CFI topology and the iodides of the quaternary sparteinium compound **A** and **B**. The spectra of the as-synthesized materials with **A** and **B** as organic agents (Figure 1-a and c) are similar to the spectra of **A**-iodide and **B**-iodide (b and d), respectively. These results indicate that these as-synthesized materials have organic agents intact inside their pore systems. The crystallization times for the formation of these molecular sieves depend on the organic agents used. Compound **A** appears to give CFI in shorter times than **B**, whereas borosilicate AFI is obtained in shorter time by **B** rather than **A**. The difference in the crystallization time for the CFI synthesis between **A** and **B** is much clearer in the absence of Li. **A** gives the product in 15 days although B is not able to complete the crystallization in 32 days (Table 1). The crystallization time is further carefully compared for the CFI syntheses when Li is used in the synthesis and the results are shown in Figure 2. The CFI begins to form in two days and crystallization is almost completed in three days with **A** as an organic agent, while it takes three days to observe diffraction lines and five days to obtain a fully crystalline material when using **B**. Figure 3 shows the SEM images of the crystals obtained from these syntheses (the as-synthesized sample obtained after 4 days of heating with **A** and after 5 days for **B**, respectively). The crystal size of the product synthesized with **A** is approximately 5×15μm whereas the size of the product obtained with **B** is much smaller (~2×5μm). Since the crystal size is related to the number of nuclei, it reflects how readily the

organic agent is able to form nuclei. Thus, the final crystal size is somewhat suggestive of how strong the structure-direction of the organic agent is. Thus, **A** appears to be a better structure-directing agent for CFI than **B** in that it causes a greater degree of nucleation and a faster rate of crystallization.

A possible reason why **A** is a better SDA than **B** for the formation of the CFI is the bulkiness of **A**. **A** is slightly larger than **B** that may fit in the 14-membered ring of the CFI pore in a conformation that may allow for a greater number of van der Waals contacts. Another possibility is the difference in hydrophobicity. Often it is observed that a more hydrophobic organic is able to form the pure-silica molecular sieve in shorter time than less hydrophobic ones [19]. Figure 4 shows the results of phase transfer experiments from water to chloroform of **A**, **B** and **C** as well as the relationship between the $C/N^+$ ratio and the transfer of simple tetraalkylammonium iodides [14]. Although both **A** and **B** have the same $C/N^+$ ratio, **B** has lower transfer than **A**. This is probably due to the existence of the nitrogen in the tertiary amino group in **B** whose electron lone pair may make the compound more hydrophilic. **A** also has the tertiary amino group but it is too close to the charged center to contribute to increase the hydrophilicity (the phase transfer value of **A** is almost the same as tetrabutylammonium iodide). Thus, the better performance of **A** in the CFI synthesis could be due to its higher hydrophobicity. However, in an apparent contradiction to this hydrophobicity argument, **B** is able to form the borosilicate AFI more readily than **A** (Table 1).

Molecular modeling studies reveal that the van der Waal energies of interaction between the CFI framework and the SDA molecules calculated on the basis of 1 SDA per unit cell are -7.68404 kcal for the **A** /CFI interaction and -5.34177 kcal for the **B**/CFI interaction. These calculated stabilization energies correlate well with the experimental observations of a decrease in the crystallization time and an increase in the nucleation (smaller crystallite size) of CFI in the presence of **A** relative to **B**. The

increased stabilization energy between **A** and the CFI framework (Figure 5-a) compared to **B** (Figure 5-b) appears to be primarily a result of the interaction between the N-methyl group of the organic agent and the eight membered-ring pockets along the channel system of the CFI. The cisoid orientation of the N(1)-methyl group (relative to N(16) lone pair electrons) in **A** allows increased van der Waals contacts between the methyl hydrogens of **A** and the framework oxygens of the eight membered-ring pocket relative to the transoid configuration of the N(16)-methyl group of **B**. These results indicate that while both **A** (N(1)-methyl-α-isosparteinium) and **B** (N(16)-methylsparteinium) serve specific structure-directing functions for the formation of pure-silica CFI, **A** is better able to stabilize the unique pore structure of CFI due to the increased van der Waals interactions of the cisoid N-methyl group with the side pockets of the CFI pores.

Efforts to synthesize molecular sieves using **C** as an organic agent are summarized in Table 2. Although a variety of reaction conditions were employed, no molecular sieves were obtained. This is probably due to its hydrophilicity (shown in Figure 4) and low thermal stability (decomposed in a day at 120°C at high pH).

## Conclusions

Although the microporous materials with novel structures were not obtained using the two sparteine derived compounds **A** and **C** as structure-directing agents, strong structure-direction for the formation of the pure-silica, molecular sieve with the CFI topology of **A** is revealed. This strong structure-direction is most likely due to its ability to adopt an occluded configuration that provides for more van der Waals contacts compared to diastereomer **B**. The fact that **C** is not able to direct the formation of any crystalline microporous materials is consistent with the proposition that possession of proper hydrophobicity (the transfer from water to chloroform should be more than zero) and thermal stability under the molecular sieve synthesis condition are necessary

features for the structure-direction in high-silica, molecular sieve syntheses as previously reported [15].

Acknowledgment

Financial support for this project was provided by the Chevron Research and Technology Co. The authors thank Dr. Stacey Zones of the Chevron Research and Technology Co. for helpful discussions. KT thanks Showa Denko K. K. for the opportunity to study at Caltech. PW thanks the Dow Chemical Company Foundation for a Dow Graduate Fellowship.

References

[1] M.E. Davis, Chem. Eur. J., 3 (1997) 1745.

[2] M.E. Davis and S.I. Zones, in: M.L. Occelli, H. Kesseler (Eds.), Synthesis of Porous Materials: Zeolites, Clays and Nanostructures, Marcel Dekker, New York (1996).

[3] M.E. Davis and R.F. Lobo, Chem. Mater., 4 (1992) 756.

[4] Y. Nakagawa, US Patent 5,271,922.

[5] R.F. Lobo and M.E. Davis, Microporous Materials 3 (1994) 61.

[6] P. Wagner, M. Yoshikawa, M. Lovallo, K.Tsuji, M.Tsapatsis and M.E. Davis, Chem. Commun., 1997, 2179.

[7] M. Yoshikawa, P. Wagner, M. Lovallo, K. Tsuji, T. Takewaki, C.-Y. Chen, L.W. Beck, C.W. Jones, M. Tsapatsis, S.I. Zones and M.E. Davis, J. Phys. Chem. B, 102 (1998) 7139.

[8] P.A. Barrett, M.J. Diaz-Cabanas, M.A. Camblor and R.H. Jones, J. Chem. Soc., Faraday Trans., 94 (1998) 2475.

[9] T. Borowiak and I. Wolska, J. Mol. Struc., 374 (1996) 97 and ref. of this article.

[10] A.E. Koziol, Polish J. Chem., 65 (1991) 1367 and ref. of this article.

[11] A.E. Koziol, J. Crystallogr. Spectrosc. Res., 22 (1992) 449.

[12] N. J. Leonard and R.E. Beyler, J. Am. Chem. Soc., 72 (1950) 1316.

[13] N. J. Leonard, P. D. Thomas and V. W. Gash, J. Am. Chem. Soc., 77 (1955) 1552.

[14] M.F. Simeonov, S.L. Spassov, H. Duddeck, U. Majchrzak-Kucznska and J. Skolik, Magn. Res. Chem., 27, (1989) 476.

[15] Y.Kubota, M.M. Helmkamp, S.I. Zones and M.E. Davis, Microporous Mater., 6 (1996) 213.

[16] CERIUS$^2$, Molecular Simulations, Cambridge, UK, (1993).

[17] U. Majchrzak-Kuczyska, A. E. Koaiol, K. Langowska and M Weiwiorowski, Bull. Polish Acad. Sci., 32 (1984) 233.

[18] A. C. Larson and R. B. Von Dreele Los Alamos Laboratory Report, (1987) No. LA-UR-86-748.

[19] K.Tsuji and M.E. Davis, Microporous Mater., 11 (1997) 53.

**Table 5.1.** Summary of molecular sieve syntheses using **A** and **B** as structure-directing agents.

| SDA | Gel composition* | Temp/°C | Time/days | Product | R/u.c. ** |
|---|---|---|---|---|---|
| **A** | 0.2 ROH/ 1 $SiO_2$(c) / 0.1 LiOH/ 40 $H_2O$ | 175 | 3 | CFI | 0.810 |
| **B** | 0.2 ROH/ 1 $SiO_2$(c)/ 0.1 LiOH/ 40 $H_2O$ | 175 | 4 | CFI | 0.751 |
| **A** | 0.3 ROH/ 1 $SiO_2$(c) / 40 $H_2O$ | 175 | 15 | CFI | 0.983 |
| **B** | 0.3 ROH/ 1 $SiO_2$(c) / 40 $H_2O$ | 175 | 32 | Amorphous(+CFI) | |
| **A** | 0.2 ROH/ 1 $SiO_2$(f)/ 0.02 $B_2O_3$/ 0.1 NaOH/ 40 $H_2O$ | 175 | 20 | AFI+Layered | |
| **B** | 0.2 ROH/ 1 $SiO_2$(f)/ 0.02 $B_2O_3$/ 0.1 NaOH/ 40 $H_2O$ | 175 | 12 | AFI+Layered | |
| **A** | 0.2 ROH/ 1 $SiO_2$(f)/ 0.02 $B_2O_3$/ 0.1 NaOH/ 0.02 seed/ 40 $H_2O$ | 175 | 2 | AFI | 0.689 |
| **B** | 0.2 ROH/ 1 $SiO_2$(f)/ 0.02 $B_2O_3$/ 0.1 NaOH/ 0.02 seed/ 40 $H_2O$ | 175 | 1 | AFI | 0.673 |

* $SiO_2$(c): Colloidal silica, $SiO_2$(f): Fumed silica.

** The amount of occluded organic molecules per unit cell calculated from TGA results.

**Table 5.2**. Results of molecular sieve syntheses using **C** as an organic agent.

| Gel composition* | Temp. /°C {Time/days} | Product |
|---|---|---|
| 0.15 $R(OH)_2$/ 1 $SiO_2$(f)/35 $H_2O$ | 150{120}, 175{120} | Amorphous |
| 0.15 $R(OH)_2$/ 1 $SiO_2$(f)/0.05 NaOH/ 35 $H_2O$ | 150{20}, 175{20} | Amorphous |
| 0.15 $R(OH)_2$/ 1 $SiO_2$(f)/ 0.02 $B_2O_3$/ 0.05 NaOH/ 35 $H_2O$ | 150{120}, 175{120} | Amorphous |
| 0.15 $R(OH)_2$/ 1 $SiO_2$(c)/ 40 $H_2O$ | 150{148}, 175{148} | Amorphous |
| 0.15 $R(OH)_2$/ 1 $SiO_2$(c)/ 0.02 seed (B-beta)/ 40 $H_2O$ | 150{148}, 175{148} | Amorphous |
| 0.15 $R(OH)_2$/ 1 $SiO_2$(c)/ 0.1 LiOH/ 40 $H_2O$ | 150{43}, 175{21} | Dense+Amorphous |
| 0.15 $R(OH)_2$/ 1 $SiO_2$(c)/ 0.02 $B_2O_3$/ 0.1 NaOH/ 40 $H_2O$ | 150{43}, 175{11} | Dense+Amorphous |
| 0.2 $R(OH)_2$/ 1 $SiO_2$(c)/ 0.04 ZnO/ 0.1 LiOH/ 45 H2O | 135{105}, 175{105} | Amorphous |
| 0.15 $R(OH)_2$/ 1 $SiO_2$(t)/ 0.025 $Al_2O_3$/ 0.15NaOH/ 53 $H_2O$ | 175{173} | Amorphous |
| 0.15 $R(OH)_2$/ 1 $SiO_2$(c)/ 0.1 $Al_2O_3$/ 0.5 NaOH/ 40 $H_2O$ | 120{14}, 135{8}, 150{1} | Amorphous |

* $SiO_2$(f): Fumed silica, $SiO_2$(c): Colloidal silica, $SiO_2$(t): Tetraethylorthosilicate

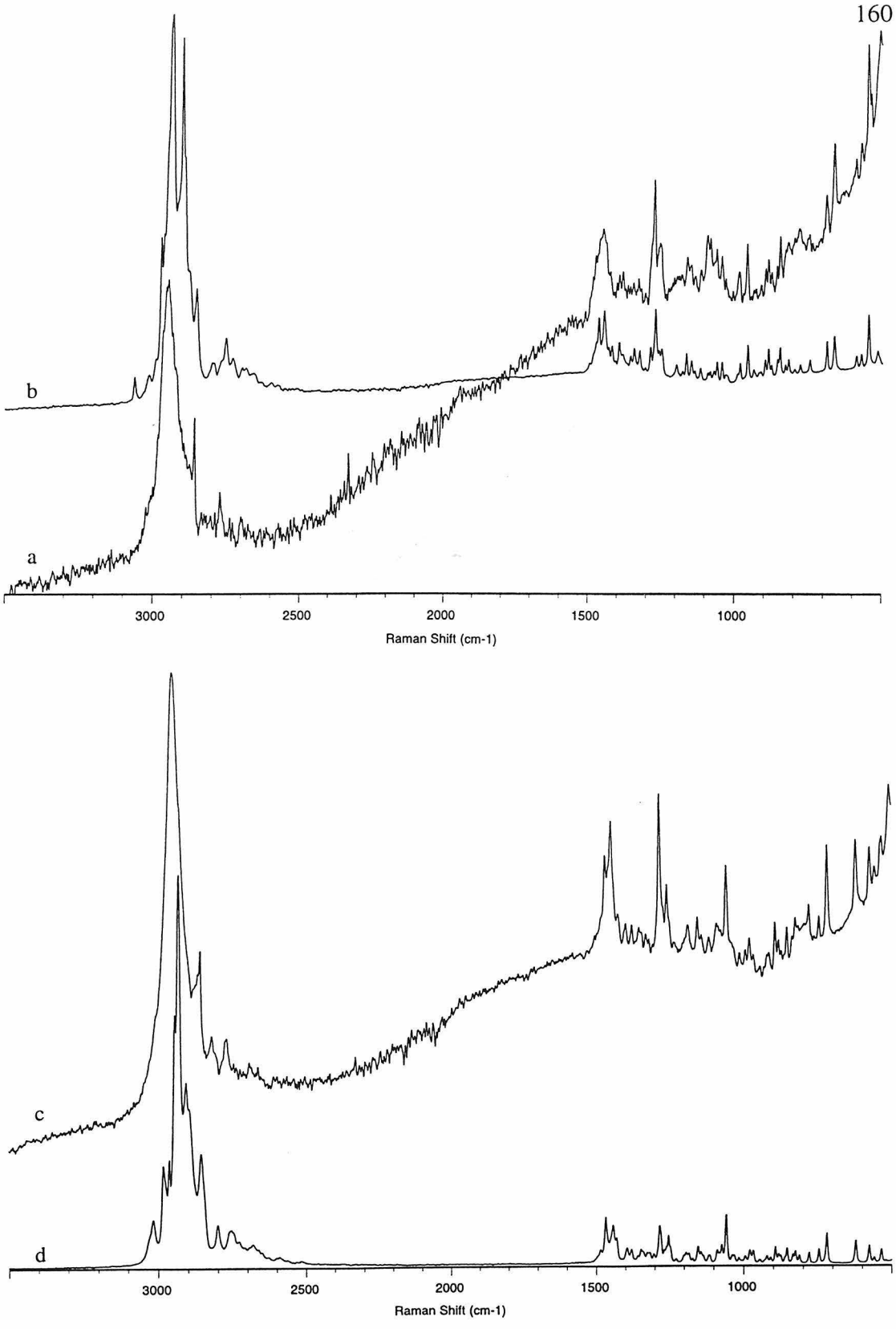


**Figure 5.1.** Raman spectra of the as-synthesized CFI and the SDAs. a: As-synthesized CFI with **A**, b: **A**-iodide, c: As-synthesized CFI with **B**, d: **B**-iodide.

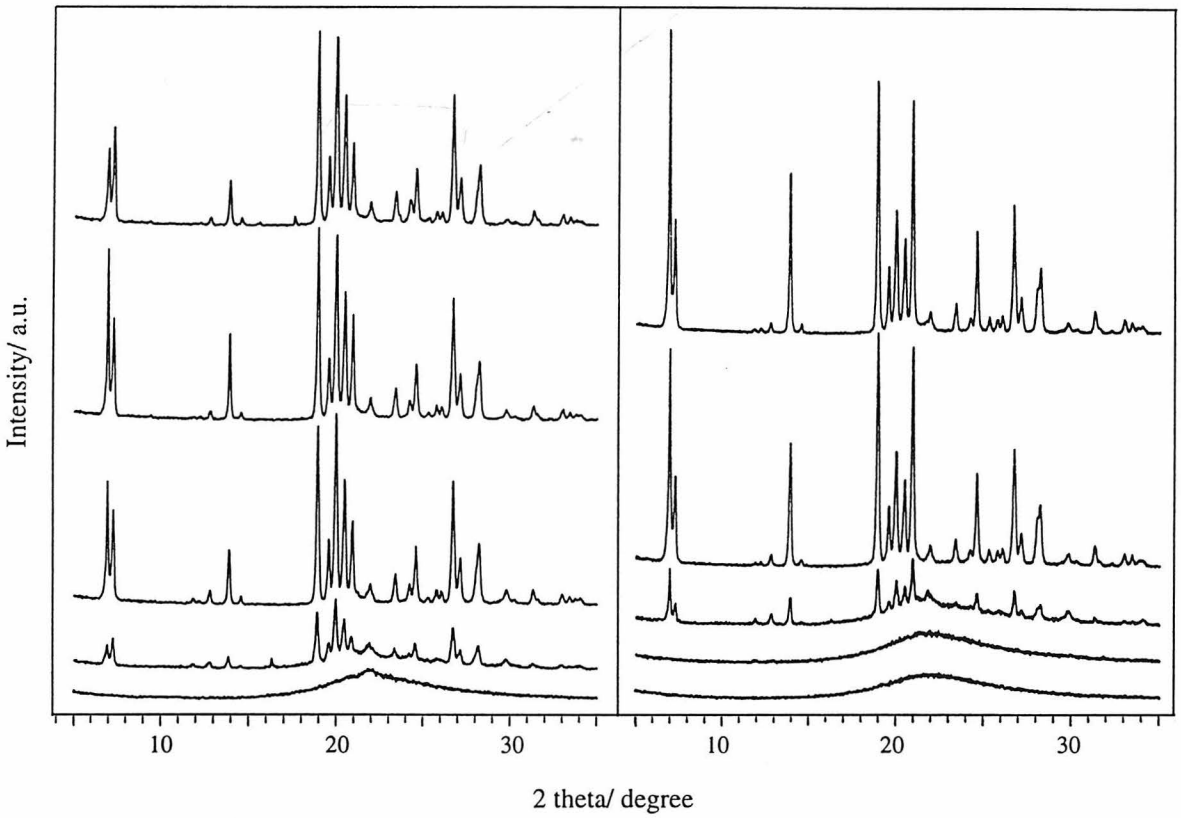


**Figure 5.2.** XRD patterns of as-synthesized materials with **A** and **B** as structure directing agents. Left from the bottom: as-synthesized materials with **A** after 1 day, 2 days, 3 days, 4 days and 5 days of heating at 175°C, respectively. Right from the bottom: as-synthesized materials with **B** after 1 day, 2 days, 3 days, 4 days and 5 days of heating at 175°C, respectively.

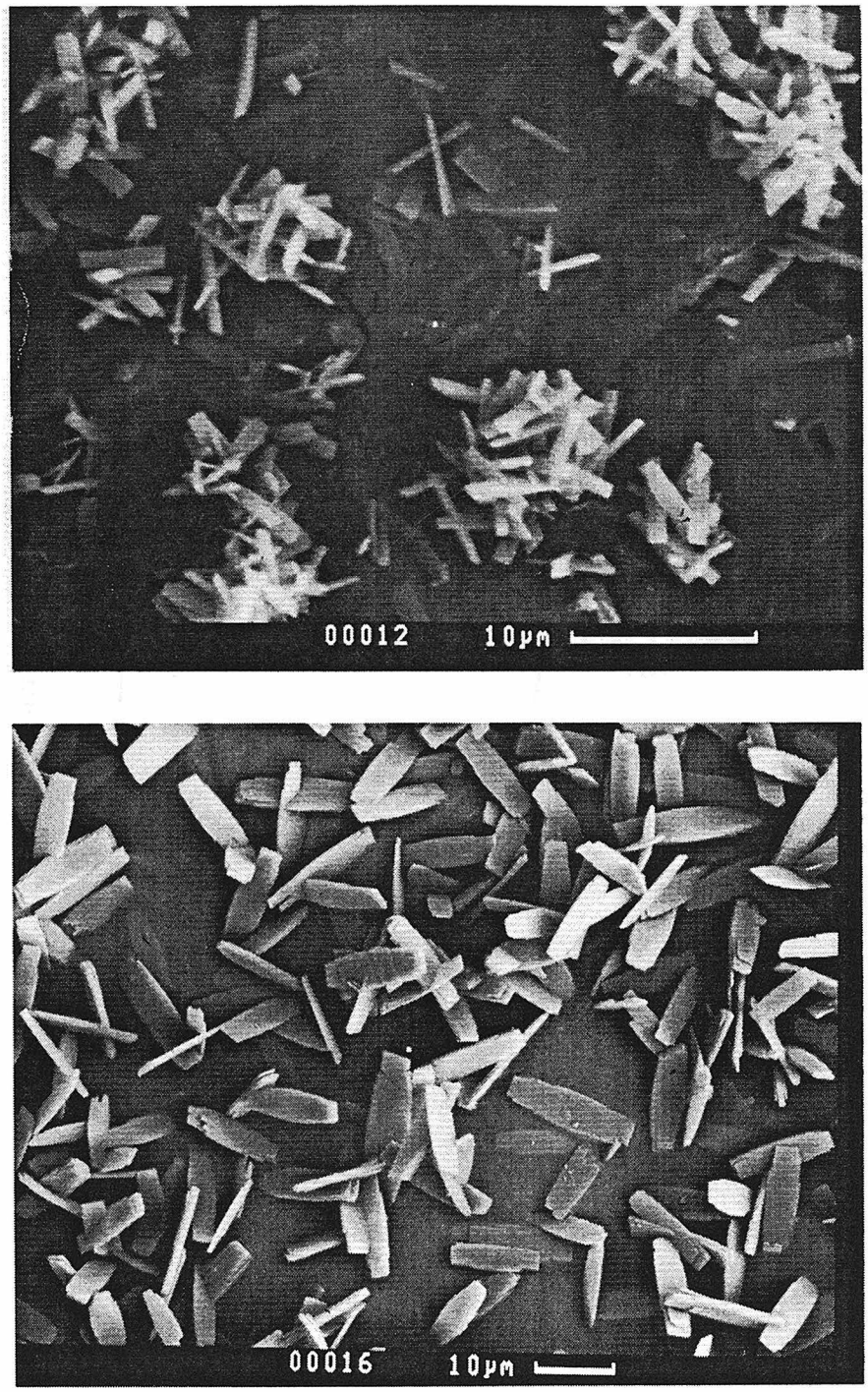


**Figure 5.3.** SEM images of the as-synthesized CFI. Top: As-synthesized CFI with **A**, Bottom: As-synthesized CFI with **B**.

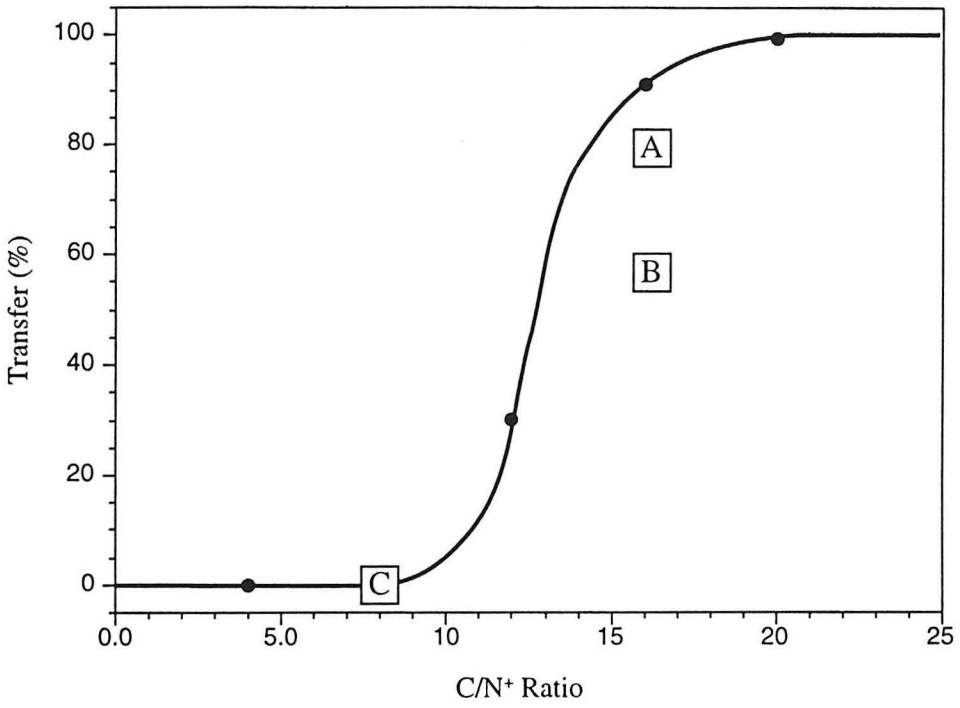


**Figure 5.4.** Results of phase transfer of **A**, **B** and **C**-iodide from water to chloroform. The solid dots are from tetraethylammonium iodide, tetrapropylammonium iodide, tetrabutylammonium iodide and tetrapentylammonium iodide [15].

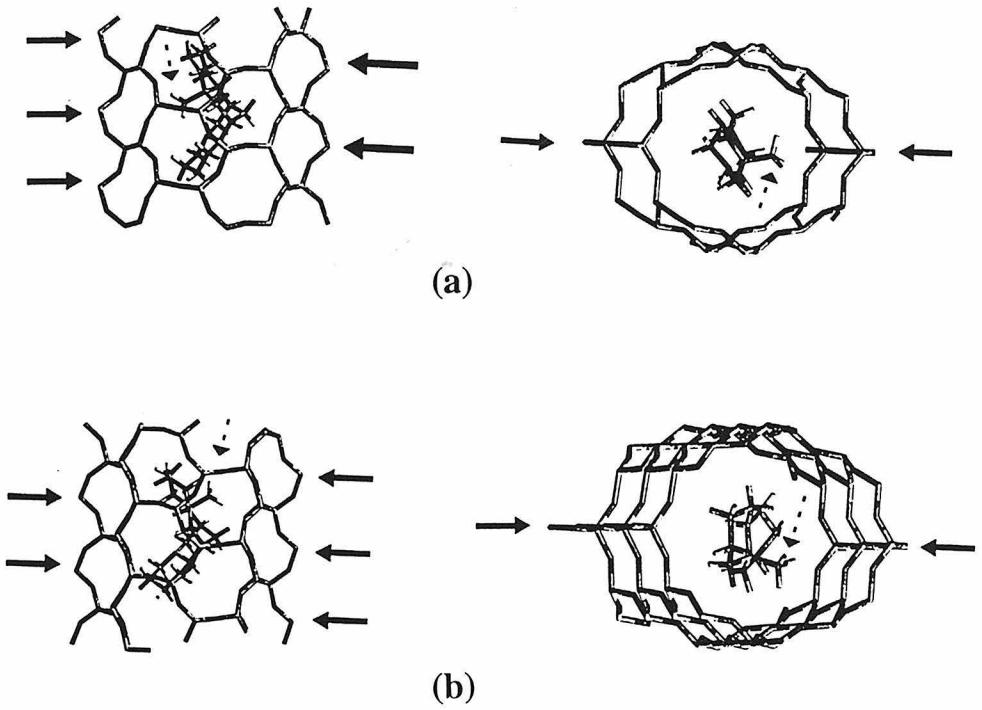


**Figure 5.5.** Calculated minimum energy configurations of SDAs within the pores of CFI (a) The configuration of **A** perpendicular to the pore direction (left) and down the pores (right), (b) The configuration of **B** perpendicular to the pore direction (left) and down the pores (right). Solid arrows indicate framework cage positions and dashed arrows indicate N-methyl groups.

# CHAPTER SIX

# Guest/Host Interaction Study II: Synthesis of the Novel Cage-Based Zeolites: SSZ-35, SSZ-36, and SSZ-39

[P. Wagner Y. Nakagawa, G. Lee, M. E. Davis, S. Elomari, R. C. Medrud, and S. I. Zones, 'Guest/Host Relationships in the Synthesis of the Novel Cage-Based Zeolites: SSZ-35, SSZ-36, and SSZ-39" submitted to *J. Am. Chem. Soc.*]

Abstract

Here we report the synthesis and structure of three silicate molecular sieves, SSZ-35, SSZ-36, and SSZ-39 that are synthesized from a library of 37 different cyclic and polycyclic quaternized amine molecules. The size and shape of the quaternized amine molecules are designed in order to obtain novel zeolite structures and the synthesis of these designed quaternized amine molecules is presented. The selectivity for the three zeolite phases is found to depend on both the organic structure directing agent (SDA) and on the degree of heteroatom lattice substitution of $Al^{+3}$or $B^{+3}$ in the silica framework. Molecular modeling is utilized to probe the effects of the non-bonded SDA/zeolite interaction energy on the SDA selectivity for the observed zeolite phase. The Rietveld refinement of the powder X-ray data confirms the structure of the SSZ-39 zeolite to be isomorphous with the aluminophosphate molecular sieve, SAPO-18 (AEI). The structure of SSZ-36 is found to possess a range of fault probabilities between the 2-dimensional channel system, end-member polymorphs, ITQ-3 and RUB-13 (International Zeolite Association Codes ITE and RTH respectively). The SSZ-35 structure is reported to contain a 1-dimensional pore system possessing stacked cages circumscribed by alternating rings of 10 and 18 tetrahedral-atoms (10- and 18- membered-rings, MRs).

.

Introduction

There remains a keen interest in developing new, three-dimensional, zeolitic silicate frameworks as these materials have found commercial use in hydrocarbon processing in the petrochemical industries. Catalysts based upon zeolites continue to proliferate in the extent of varied uses in the modern refinery [1]. New zeolite structures lend themselves to the possibility of finding new niches in processing based upon shape-selective capabilities. This trend represents a step change from much of the previous applications of Y zeolites (FAU) that perform much of the large scale catalyst work in areas like FCC and hydrocracking. Recent niche-selective examples have been the replacement

of solvent extraction by shape-selective zeolites capable of isomerization dewaxing [2] in the pursuit of high quality lube oil basestocks and the introduction of zeolitic catalysts to replace phosphoric acid on a silica support in the production of cumene from benzene and propylene [3]. Cumene is then oxidized in a commercial process to produce both phenol and acetone.

Many of the novel silica-based zeolite structures are derived from the use of organo-cations as guest molecules in the crystallizing product, i.e., they effectively stabilize the void regions within the inorganic structure. A popularization of this guest activity has been to refer to them as "template" molecules [4] or as "structure-directing agents" (SDA) [5]. Clearly, part of the challenge in synthesizing new zeolites is to develop candidate guest molecules that have the potential to generate novel zeolite structures. While the size and shape of the guest molecules often correlates well with the void dimensions within the host, there are still aspects of phase selectivity in zeolite synthesis that are kinetically controlled. That is, the same organo-cation guest may be capable of crystallizing more than one zeolitic phase [6]. So, while research becomes ever more sophisticated in molecular modeling approaches towards developing favorable guest/host interactions [7], the experimentalist is still faced with the question of what controls "how to get there" [8].

From the standpoint of empirical learning, we have divided the set of high-silica zeolite formation into five domains that are related by the extent of lattice substitution and the size of the guest SDA molecule. With small SDA molecules and little heteroatom lattice substitution, clathrates are the favored product [9]. Clathrates are cage based structures in which the guest molecule is surrounded by an inorganic lattice with portals too small to allow any communication between cages. As the guest molecules become larger, the second domain is observed in which one-dimensional, parallel pore systems are found at the high-silica lattice content. A third case results as lattice substitution increases, and multidimensional channel systems possessing larger overall micropore volumes predominate. A fourth domain is often observed at high lattice substitution, in which the

highly heteroatom substituted zeolites contain cages with smaller portals. The fifth domain arises from the use of large guest molecules with strong non-bonded SDA/zeolite interaction energy resulting in the stabilization of open framework zeolite lattices; in this case, due to the strong interaction energy, the stabilized framework structure is formed over the entire heteroatom lattice substitution range. The recent report of a pure-phase MEL zeolite (ZSM-11) is an example of this fifth case [10].

In order to overcome the propensity for SDA molecules to form clathrate structures, Nakagawa developed a designed organic system that was based upon bringing together individual ring structures in a Diels-Alder reaction to build candidate molecules leading to large pore zeolites [11]. The individual rings themselves, if converted into charged ammonium compounds, would generate clathrate products. Figure 1 shows three different sized norbornane derivatives (based upon Diels-Alder chemistry) and the transition from clathrate to open pore structure. Many of the rigid, elongated SDA derivatives formed from variations of cyclopentadiene reacting with maleimides produce open-pore, one-dimensional zeolites like MTW or SSZ-31 (shown in Figure 1) These two 12-ring zeolites possess different configurations of the pore opening, with the MTW containing a somewhat puckered pore opening [12] and the SSZ-31 possessing a very open but highly elliptical pore opening with dimensions ranging from 8.8 Å to 5.5 Å [13].

Here, we describe our efforts to synthesize novel zeolite structures by designing SDA molecules that are both too large to fit into the cages of the clathrate-type silicates, and that possess a spheroidal shape that precludes the formation of the straight one-dimensional channel system zeolite structures that tend to form when using rigid elongated SDA molecules, e.g., Figure 1b. The initial success of this SDA design effort resulted from a derivative of the camphor-type molecule (Entry 1, Table 2) that led to the crystallization of the novel, open-framework zeolites SSZ-35 and 36. Subsequently, numerous other zeolite structure directing molecules were discovered using this design

strategy (Tables 1-3) and we present a detailed investigation into the guest/host relationship between these organic SDA molecules and the resulting zeolite phases.

## Experimental Section

### Synthesis of Organo-Cation Structure Directing Agents (SDAs)

The syntheses of the 37 organo-cation SDAs that appear in Tables 1-3 are reported in the Supplementary Materials Section. Table 1 presents the monocyclic organic directing molecules, Table 2 presents the bicyclic organic directing molecules and Table 3 presents the tri- and tetracyclic organic directing molecules used in this study. The quaternary ammonium guest molecules are used in their hydroxide form after ion exchanging the halide anion using BioRad AG 1-X8 ion exchange resin. All reagents are from Aldrich Chemical Co. unless otherwise stated.

### Zeolite Syntheses

The individual zeolite synthesis reactions are run in Parr reactors of 23-ml capacity. The crystalline products are generally collected on glass frits, washed with roughly 100 times the amount of water as the initial reaction solution, and then air dried before XRD patterns are obtained on a Siemens D-500 instrument. The six different zeolite syntheses run for the majority of the 37 guest molecules reported here were recently described [14], and a representative procedure for each synthesis is presented. The reactions are labeled as to starting silica-to-alumina ratio (SAR) or, in one case, the corresponding ratio for silica and borate . These reactions correspond to the entries found in Table 4 in which the reaction product is presented.

SAR = 30: 2 millimoles of the guest molecule hydroxide is mixed with 0.20 gram of 1 N NaOH and the mass brought to 6 grams with water. 2.5 grams of Banco "N" silicate is added (28 wt % $SiO_2$, 8.9 wt % $Na_2O$). 0.25 grams of Union

Carbide's LZY–62 is added as an aluminum source. The reaction is heated at 135∞C and 43 rpm and is checked every 3-4 days for a pH jump (from near 11.80 to 12.50).

SAR = 40: 2.15 millimoles of guest molecule hydroxide is mixed with 1.43 grams of 1 N NaOH and the mass brought to 7.2 grams with the addition of water. 0.25 gram of Union Carbide's LZY-52 zeolite is added as aluminum source, and finally 0.80 gram of Cabosil-M5 is added. This reaction is run like the one above but at 160∞C.

SAR = 70: 3 millimoles of the organic hydroxide is mixed with 0.76 gram of 1 N NaOH and the total mass is brought to 7 grams with water. 0.25 gram of Union Carbide's LZ 210 and 0.74 gram of Cabosil-M5 is added, and the reaction is run at 170∞C and 43 rpm.

SAR =100: 2.15 millimoles of organic hydroxide and 1.50 millimoles of 1 N NaOH are brought up to a mass of 11.75 grams with water. 0.03 grams of Reheis F-2000 alumina (53 wt % $Al_2O_3$ ) is dissolved. Finally, 0.90 gram of Cabosil-M5 is blended in and the reaction is carried out at 170∞C with 43 rpm.

SAR = 300: In this reaction, Tosoh's 390 HUA is used as the Si and Al source [15]. 2.25 millimoles of organic hydroxide and 2.25 millimoles of 1 N NaOH are combined and the mass brought to 10 grams with water. 0.90 gram of Tosoh 390 HUA is added and the reaction is heated at 160∞C with 43 rpm tumbling.

$SiO_2/B_2O_3$ = 30: 2.25 millimoles of organic hydroxide in 4.35 mL of water is used to dissolve 0.095 gram of sodium borate decahydrate. When the solution is clear, 1.36 grams of Dupont's Ludox AS-30 (30% $SiO_2$) is added and the reaction is heated at 160∞C without stirring. The completion of the reaction is determined by the transformation of the uniform gel into a settled solid.

Sample Preparation for Synchrotron Data Collection

The calcined silicate materials are loaded into 1 mm diameter glass capillaries, heated to 350°C under vacuum and then sealed. The data collected on the X7A

synchrotron beamline at the National Synchrotron Light Source at Brookhaven National Laboratory (Upton, NY) are indexed [16] and converted into a format compatible with GSAS [17] for the Rietveld refinement work.

## Molecular Modeling

Monte Carlo simulations are conducted at 300 K with a fixed loading of 1 organic guest molecule per cage [18]. The sorption simulation probes 20,000 guest/host configurations, and the lowest energy result is energy-minimized using the Burchart-Universal force field. The framework atoms are fixed during the energy minimization, and the cationic charge of the organo-cation is counterbalanced by averaging the negative charge over the framework atoms. The reported stabilization energies represent only the nonbonded van der Waals interactions between the silicate framework and the organic guest.

## Results and Discussion

### Synthesis

Table 4 presents the silicate products that result from each of the 37 structure directing molecules (Tables 1-3) in the zeolite synthesis reactions with silica-to-alumina-ratios (SAR) =30,40,70,100, >300 and also with boron lattice substitution (silica-to-borate-ratio, SBR =40) . The three letter code entries in Table 4 are assigned by the International Zeolite Association and further information on these structures can be found in reference 19. Zeolites that are referred to with an SSZ designation in Table 4 have not yet been assigned structure codes.

### Observed Zeolite Formation Domains

Entry 3 in Table 4 provides an example of the first domain of zeolite synthesis discussed in the Introduction in which small SDA molecules tend to result in the

formation of clathrates at low lattice substitution. The clathrate NON results from the small molecule SDA Entry 3 over a range of low lattice substitutions (SAR: 70 ->300) as seen in Table 4. At very low lattice substitution (SAR >300) the small molecule SDA Entry 4 is also seen to direct for the clathrate NON. The results indicate that these small SDA molecules effectively maximize the silica/SDA interaction by stabilizing the small silica cages present in the clathrate materials such as NON and DDR.

As the size of the SDA molecule is increased beyond the small cage size of the clathrates, one-dimensional channel system zeolites tend to form at low lattice substitution. Entry 5, Table 4 indicates that the *N,N*-diethyl piperidium derivative molecule that possesses a pendent ethyl group off of the carbon ring results in the crystallization of the 1-dimensional channel system zeolite SSZ-31 at SAR >300. Increasing the lattice substitution results in the formation of the multidimensional, 10 MR zeolite MFI (SAR 40 and 70). This SDA provides examples of the second and third domains of zeolite formation.

At very high lattice substitution the zeolitic phases denoted SSZ-39 and CHA tend to crystallize from a number of the SDA molecules in Tables 1-3. The most aluminum-rich reaction described in the Experimental Section (SAR =30) is the best reaction for selectively generating these zeolite. Compared with the other five zeolite synthesis reactions described, the high alumina syntheses also have a much higher OH/Si ratio in the reactants. Zeolite synthesis mixtures containing high alumina and high hydroxide concentrations are favorable for producing cage-based zeolites, such as CHA, with small 8-ring pores and structural subunits constructed of even-membered tetrahedral-atom rings [20]. The structure solution of SSZ-39 outlined below also reveals that this zeolite contains cages with 8-ring pores and is composed entirely of 4- and 6- membered rings of tetrahedral atoms similar to CHA. These even-membered-ring zeolites tend to form at high-lattice substitution because the strict alternation of the silicon and aluminum in the framework avoids the energetically unfavorable electrostatic interaction that arises from two

adjacently located negatively charged alumina tetrahedra. CHA and SSZ-39 are examples of the fourth zeolite formation domain in which high alumina containing zeolite syntheses result in highly heteroatom-substituted, even-membered-ring containing zeolites that possess cages with smaller portals.

The tetracyclic Diels-Alder product, Entry 29, Table 3 (also shown in Figure 1c), is an example of a large rigid spheriodal SDA that is designed to obtain novel, open framework zeolites by avoiding the crystallization of the commonly observed clathrates and straight 1-dimensional channel system zeolites that result when either small or rigid elongated molecules are employed as SDAs. As can be seen from Entry 29 of Table 4, this tetracyclic Diels-Alder SDA molecule is found to have a very high selectivity for the novel zeolite phase denoted SSZ-35 over the entire lattice substitution range from fairly aluminum rich (SAR =30) [21] to pure-silica. The diffraction pattern of SSZ-35 is presented in Figure 2. The strong non-bonded SDA/zeolite interaction energy between Entry 29 and SSZ-35 accounts for the high phase selectivity (as will be discussed in more detail in the molecular modeling section); replacing just one *N*-methyl group with ethyl prevents the crystallization of SSZ-35. Entry 29 successfully achieves the design goals for generating new zeolite topologies and provides an example of the fifth domain of zeolite formation in which strong non-bonded SDA/zeolite interactions stabilize a particular zeolite structure over a wide range of lattice substitution.

The extensions of methyl groups off the bicyclic ring system of Entry 1 (Table 2) also creates a bulky spheriodal SDA that satisfies the design strategy, however the phase specificity in this case is much weaker than in the previous case. The use of organo-cation 1 (Table 1) in zeolite synthesis reactions with silica-to-alumina ratios (SAR) of 100 also results in the formation of SSZ-35 (Entry 1, Table 4). Increasing the alumina or borate content in zeolite synthesis reactions containing Entry 1 (Table 1) results in the novel zeolitic phase denoted SSZ-36 (Entry 1, Table 4). A diffraction pattern for SSZ-36

is shown in Figure 3a. Clearly Entry 1 has a weaker selectivity for SSZ-35 than Entry 29 and illustrates the competing influences of the kinetic control of the inorganic gel composition with the thermodynamic influences of the organic/inorganic interactions in the zeolite formation and will be explored more thoroughly in the molecular modeling section.

Summary of SSZ-35, SSZ-36 and SSZ-39 Syntheses

A number of zeolite synthesis trends are apparent within the group of 37 organo-cation guest molecules employed in this study (Table 4). The SSZ-36 material is generally favored by the mono and bicyclic ring systems (Tables 1 and 2) with ring methylation beyond the charged nitrogen and tends to preferentially form at higher heteroatom lattice-substitutions; no pure-silica example has been found. The SSZ-36 product can be crystallized at high lattice substitution with SAR =10-40 [21] and can also be crystallized in the presence of a number of guest molecules when the synthesis conditions are rich in borate. It is important to note that certain reflection intensities and breadths observed in the SSZ-36 powder X-ray diffraction data depend on the degree of lattice substitution and the organo-cation employed in the SSZ-36 syntheses. Such preferential line broadening in the powder X-ray data is indicative of faulting and will be discussed in greater detail below in the context of the SSZ-36 structure.

SSZ-35 is most effectively crystallized in the presence of tri- and tetracyclic charged compounds (Table 3) with no additional ring derivatization and tends to be favored at low lattice substitution. The calculated SDA/zeolite interaction energy indicates that the tri- and tetracyclic quaternized amine molecules provide favorable van der Waals stabilization of the SSZ-35 cages as will be discussed in more detail in later. The distinct preference for forming this new zeolite structure via the tri- and tetracyclic organo-cations indicates that not only the overall size of the molecule but also the shape of the molecule is important in considering new molecules as SDAs for zeolite synthesis.

As discussed previously, SSZ-39 is able to be crystallized from a wide range of the SDA molecules in Tables 1-3 at very high lattice substitution. The reactions employing high alumina content also require a high hydroxide concentration in order to soluablize the alumina and tend to result in cage-based zeolites with small portals such as SSZ-39 due to the ordering of aluminum in the framework; the details of the SSZ-39 structure are presented below. Highly lattice substituted even-membered ring containing zeolites such as CHA and SSZ-39 tend to be observed when the inorganic gel composition predominates over the organic /inorganic interactions.

Zeolite Structures

SSZ-35

The details of the structure solution of the high-silica, molecular sieve SSZ-35 are described in a recent publication [22]. The structure contains an unusual, one-dimensional channel system with pore openings that alternate between rings containing 10 tetrahedral atoms (T-atoms) and 18 tetrahedral atoms (Figure 4a). This alternating pore diameter can also be viewed as arising from the stacking of [6, 5, 4] cages with 10 T-atom openings at the top and bottom of the cages (Figure 4b).

SSZ-39

The refined [17] unit cell parameters for SSZ-39 obtained from the synchrotron powder XRD data are a = 13.629692 Å, b = 12.674772 Å, c = 18.473045 Å and $\beta$ = 89.9288°. Analysis of the systematic absences for the monoclinic structure indicates a space group assignment consistent with *C 2/c* (No. 15). The structure solution of the new aluminosilicate SSZ-39 is obtained by the isomorphic substitution of the non-oxygen framework atoms in the SAPO-18 structure [23] with silicon atoms.

For the Rietveld refinements of SSZ-39 from the synchrotron powder XRD data (SPXRD), 10 background parameters (shifted Chebychev function) , the scale factor, and the zero shift were first refined, followed by the refinement of the lattice parameters,

six profile parameters (Simpson's rule integration of the pseudo Voight function); and finally, the atomic positions and the isotropic temperature factors for all the atoms were refined.

94 variables were refined in the final Rietveld refinement over a profile range of 2.0-50.0 degrees ($\lambda$ = 1.20106 Å, step sizes = 0.005 degree, resulting in 9600 observables) containing 649 reflections. 57 soft constraints were employed (24: d( Si-O) = 1.61 (01) Å, 33 d(O-O) = 2.61 Å), resulting in an average d(Si-O) of 1.611 Å with a maximum of 1.644 Å and minimum of 1.588 Å minimum of 105.5°, and the average Si-O-Si angle being 148.57° with a maximum of 152.6° and a minimum of 141.3°. The final residual values were wRp = 11.338% and an Rp = 9.30%. The Fourier difference map showed maximum peak heights all less than 0.5 e-/Å. The refinement data is presented in Figure 5. The atomic position together with the isotropic temperature factors are presented in supplementary materials.

The structure of SSZ-39 is composed of columns of double 6-rings that stack along the [001] direction (Figure 6a). These columns interconnect through bridging oxygen atoms to form layers that connect through other oxygen atoms (Figure 6b). The layerlike units stack along the [010] direction and are related through mirror planes (Figure 6c). This layer stacking of the sheets of double six-ring units gives rise to a cage system similar in volume to the cages found in the SSZ-35 structure. They are interconnected in three dimensions by eight-rings as shown in Figures 6c and 6d.

SSZ-36

Twin faulting and intergrowth occurs frequently in zeolitic materials due in part to the poor specificity of the structure-directing agent for a particular end-member polymorph of the fault series. Twin faulting in zeolites is commonly manifested as a stacking disorder of a layerlike unit in which the successively stacked layers can either be

related through mirror planes or inversion centers. As the density of the twin faults increases , i.e., the distance between the twin faults decrease, broadening or streaking of reflection intensities in the diffraction data occur.

As seen in Figure 3a, the SSZ-36 material synthesized from Entry 1 in Table 2 contains a distribution of reflection widths, that together with SEMs showing uniform crystal morphology, indicates that the crystals contain a high density of twin faults. The reflections at smaller scattering angles lack significant broadening in comparison to the reflections near 18 degrees 2-Θ. These sharp reflections resemble the low scattering angle portion of the powder X-ray diffraction pattern observed for the RUB-13 material (RTH) [24].

The RTH topology possesses a two-dimensional pore system circumscribed by 8-membered rings and contains large cages that are interconnected through the 8-member rings. The RTH structure can be viewed as resulting from the stacking of layerlike units related through mirror planes that can twin parallel to c* [24]. This twin fault gives rise to layerlike units that are related through inversion centers and results in the formation of a new large cage structure that differs in shape from the cages found in the RTH structure but that possesses a similar volume. The synthesis and structure solution of the RTH end-member material has recently been reported [25] and has been given the IZC code ITE. Figure 7 (adapted from Reference 25) shows the comparison of the symmetry differences for the two cage types generated for these two end-member structures. The representation shows the 2-dimensional 8-ring pores system that intersect into sizable cages.

Simulations of powder X-ray diffraction (PXRD) data for crystals containing varying RTH-ITE twin fault densities were performed using DiFFaX [26] (Figure 8). At the low twin fault densities, the PXRD data closely matches the PXRD data resulting from the pure end-member polymorph; however, as the twin fault density

increases, broad reflection intensities arise due to the decreasing distance between the twin faults as previously discussed.

SSZ-36 has been synthesized from a number of different organic structure-directing agents and depending on the particular SDA and the degree of heteroatom substitution, the PXRD data are effected to varying degrees by twin faulting between the RTH and the ITE structures. For example, comparison of the experimental powder X-ray diffraction pattern of SSZ-36 synthesized from Entry 1, Table 2 (Figure 3a) to the fault simulations indicates that this material is a faulted intermediate between the RTH and the ITE structures with a fault probability of approximately 80% RTH (Figure 9). In contrast, Figure 3b shows the powder X-ray diffraction pattern that results from the use of Entry 18 in Table 2. Comparison of this PXRD data with the fault simulations in Figure 8 indicates that the material is nearly fault-free. The PXRD pattern is characteristic of a material consisting predominantly of the structure of the pure end-member polymorph ITE. The product here is not pure- silica, as is the case for the published ITE.

Correlations Between Guest Molecules
and Phase Selectivities

Here, we present several molecular modeling studies in which the non-bonded SDA/zeolite energy of interaction is correlated with the observed zeolite phase selectivity from a particular SDA. These results provide insights into the factors that effect the specificity for the observed zeolite phases from the designed SDA molecules.

As mentioned in the Discussion Section, the SSZ-36 material is favored by the mono and bicyclic ring systems with ring methylation beyond the charged nitrogen (Table 4). Entries 19 and 20 (Table 2) present an interesting example of this phenomenon, in which the addition of one methyl group to the carbon ring of the [4.1.1] octane molecule (Entry 19) dramatically shifts the phase selectivity from SSZ-35 to SSZ-36. Molecular

modeling calculations are employed in order to gain a better understanding of the strong specificity of the [4.1.1] octane molecule with and without the ring methyl group. The calculated non-bonded energy of the Entry 20/SSZ-35 interaction indicates that Entry 20 strongly stabilizes the SSZ-35 cage structure (-11.81kcal/cage). However, the addition of the methyl group to the carbon ring (Entry 19) results in a positive energy of interaction (0.69 kcal/cage ) indicating that the molecule is too large to fit into the cages of the SSZ-35 material. The modeling calculations suggest that the mono and bicyclic ring SDA molecules with ring methylation beyond the charged nitrogen are either too large or of the wrong shape to fit within the cages of the competing SSZ-35 phase. These results support the design strategy outlined in the Introduction for developing rigid molecules that are too large to fit into the cage or pore system of competing phases.

As discussed previously the SSZ-36 material that results from Entry 1 is a faulted intermediate between the RTH and the ITE structures. In order to gain a better understanding of the effects of the SDA molecule on zeolite faulting, Entry 1 was modeled in the cages of both ITE and RTH. The resulting VDW energies of stabilization for 1 in the RTH cages is -14.9 kcal/cage, while the stabilization energy of 1 in the ITE cages is –14.03 kcal/cage. The similarities of the nonbonded van der Waals energy of stabilization for Entry 1 within both the ITE and RTH cages suggests that this compound may lead to a structure that is a faulted intermediate between the RTH and ITE structures. The experimentally observed powder X-ray data for the SSZ-36 material that results from Entry 1 reveals that it is faulted and possesses a fault probability towards the RTH structure of approximately 80% (Figure 9).

Additional insight into the phase selectivity of the organic guests for a particular silicate framework is gained by examining the behavior of the tri- and tetracyclic molecules in Table 3. With the lone exception of Entry 37, these guest molecules all produce SSZ-35.

These molecules must therefore possess the correct size and geometry to stabilize the SSZ-35 cages.

An interesting case of SSZ-35 phase selectivity is observed for the tetracyclic Entry 29, that crystallizes SSZ-35 over the entire lattice substitution range. Molecular modeling was employed to determine the effects of the van der Waals (VDW) energy of interaction between Entry 29 and the cages of the SSZ-35 phase and the cages of the competing phases (ITE, RTH, and SSZ-39). The calculation results are located in Table 5 and indicate that Entry 29 strongly stabilizes SSZ-35 relative to these competing phases. The significant stabilization of SSZ-35 over SSZ-39 (-20.87 vs. –6.79 kcal/cage) is particularly interesting. This result is consistent with the experimental observation that, even at high aluminum substitution, Entry 29 stabilizes the SSZ-35 structure over the six-ring rich structures that commonly result from syntheses containing high alumina content and high OH/Si ratios (Entry 29, Table 4 SAR=30).

## Conclusions

Here we have presented the results of our organic structure directing agent design strategy for synthesizing the three novel zeolite phases: SSZ-35, SSZ-36, and SSZ-39. The strategy involves synthesizing rigid bulky organo-cations that are too large, or of the wrong geometry to fit into the cavities or pores of commonly encountered competing phases such as the clathrates or the straight 1-dimensional channel system zeolites, e.g. SSZ-31 and MTW.

The tri- and tetracyclic charged compounds with no additional ring derivatization (Table 3) are found to be very effective structure directing agents for the novel zeolitic phase, SSZ-35. This new material also tends to be favored at low lattice substitution. The molecular modeling results indicate that the tri- and tetracyclic quaternized amine molecules are particularly effective in stabilizing the SSZ-35 cages. The structure of SSZ-35 contains an unusual, one-dimensional channel system containing an alternating 10-

and 18 MR pore diameter that can also be viewed as arising from the stacking of cages with 10 T-atom openings at the top and bottom of the cages.

The novel zeolitic phase, SSZ-36, is favored by the mono- and bicyclic SDA molecules in Tables 1 and 2 that possess ring methylation beyond the nitrogen. Molecular modeling results indicate that these molecules are typically are too large or are of the wrong geometry to fit within the cages of potentially competing phases such as SSZ-35. The SSZ-36 phase also tends to be favored at higher lattice substitutions; no all-silica SSZ-36 materials were synthesized. The structure of SSZ-36 is found to be a faulted intermediate between the two end-member polymorphs RTH and ITE, that possess 2-dimensional pore systems circumscribed by 8 membered rings and that intersect into large cavities.

The SSZ-39 material is a frequently observed product of the high alumina containing syntheses (SAR=30) using the organic molecules in Tables 1-3. If the inorganic gel composition predominates over the organic/inorganic interactions in the high alumina containing zeolite synthesis then cage-based zeolites containing even-membered ring constructions and small portals such as SSZ-39 tend to form. The structure of SSZ-39 is found to be isomorphous with the aluminophosphate molecular sieve, SAPO-18 (AEI).

The successful strategy of designing organic zeolite directing molecules that are too large or of the wrong geometry to stabilize commonly encountered competing phases in order to synthesize novel zeolite materials is complemented by the computational modeling results that provide useful insights into the observed zeolite phase selectivities of the designed SDA molecules. Understanding the effects of the nonbonded energy of the organic SDA/zeolite interaction on zeolite phase selectivity and fault probability will play a fundamental role in the future discovery of new zeolite phases through rational SDA design.

Acknowledgments

We thank Dr. Guang Zhang and Mr. Ken Ong for help in preparation and data collection at the synchrotron source. For the gathering of X-ray data from Beamline X7A, the research was carried out at the National Synchrotron Light Source at the Brookhaven National Laboratory. This facility is supported by the U.S. Department of Energy, Division of Materials Science and Division of Chemical Sciences. We appreciate the help of Dr. D. E. Cox in the data collection. Dr. Peter Crozier, from the High Resolution Electron Microscopy Center at Arizona State University, is thanked for his work on SSZ-35. P.W. thanks Dow Chemical Company Foundation for a Dow Graduate Fellowship.

References

1. Absi-Halabi, A.; Stanislaus, A.; Qabazard, H.; *Hydrocarbon Processing*, **1997**, February, 45.
2. Miller, S. J., "Wax Isomerization for Improved Lube Oil Quality," given at AICHE Spring Meeting, March, New Orleans, 1998 (see abstracts).
3. Innes, R. A.; Nacamuli, G.; Zones, S. I. U.S. Patent 4,891,458 (1990).
4. Lok, B. M.; Cannan, T. R.; Messina, C. A. *Zeolites*, **1983**, *3*, 282.
5. Lobo, R. F.; Zones, S. I.; Davis, M. E., in Inclusion Chemistry with Zeolites, Nanoscale Materials by Design Eds., N. Herron and D. Corbin, Vol. 21(Kluwar Academic Publishers, the Netherlands), pp 47-78, 1995.
6. Wagner, P.; Yoshikawa, M.; Lovallo, M.; Tsuji, K.; Tsapatsis, M.; Davis, M. E. *J. Chem. Soc. Chem. Comm.*, **1997**, 2179-80.
7. Lewis, D. W.; Willock, D. J.; Catlow, C. R. A.; Thomas, J. M.; Hutchings, G. J. *Nature*, **1996**, *382*, p 604.
8. Davis, M. E, Zones, S. I., in Synthesis of Porous Materials, Eds., M. L. Occelli and H. Kessler (Marcel Dekker, New York), p 1, 1997.
9. Gies, H., Inclusion Compounds (Academic Press, London), Vol 5, pp 1-35 (1991).
10. (a) Nakagawa, Y., WO 95/09812.
    (b) Terasaki, O.; Ohsuna, T.; Sakuma, H.; Watanabe, D.; Nakagawa, Y.; Medrud, R. C. *Chem. Mater.* **1996**, *8*, 463.
    (c) Nijo, S. L., Koegler, J. H., van Koningsveld, H., van de Graaf, B., in Microporous Mater, 8, pp 223-230 (1997).
11. Nakagawa, Y.; Zones, S. I. *Molecular Sieves*, Vol. 1, Eds. M. L. Occelli and H. E. Robson (Van Nostrand Reinhold, New York), p 222 (**1992**).
12. La Pierre, R. B. Rohrman, A. C. Jr.; Schlenker, J. L.; Wood, J. D.; Rubin, M. K.; Rohrbaugh, W. J. *Zeolites*, **1985**, *5*, 346.

13. (a) Lobo, R. F.; Tsapatsis, M.; Freyhardt, C. C.; Chan, I. Y.; Chen, C. Y.; Zones, S. I.; and Davis, M. E. *J. Am. Chem. Soc.*, **1997**, *119*, 3732.

(b) See Treacy, M. M. J.; Deem, M. W.; Newsam, J. M. DIFFaX Version 1.801 (**1995**).

14. Nakagawa, Y.; Lee, G. S.; Harris, T. V;Yuen, L. T.; Zones, S. I. *Mesoporous and Microporous Materials*, **1998,** *22* , 69.

15. Zones, S. ,I., and Nakagawa, Y., WO 96/29,284 (**1996**).

16. Werner, P. E.; Erikson, L.; Westdahl,M. J. *J. Appl. Crytallogr.* **1985**, *18*, 367.

17. Larson A.C., Von Dreele R.B. GSAS--- General Structure Analysis System., Los Alamos National Lab. Report, LA-UR 86-748 ( 1986)

18. CERIUS 2 Version 3.5, Molecular Simulations Inc., Cambridge, UK ( 1996)

19. Meier, W. M.; Olson, D. H.; Baerlocher, Ch. *Atlas of Zeolite StructureTypes*, 4th ed.; Elseveir; London, 1996.

20. (a) Zones, S. I.; Van Nordstrand, R. A.; Novel Materials in Heterogeneous Catalysis, ACS Symp., 437, Eds. R. T. K. Baker and L. L. Murrell (ACS Publ., Washington, D.C.), p 14 (1990).

(b) Zones, S. I.; van Nordstrand, R .A Zeolites, **1989**, p 458.

21. Zones, S. I.; Nakagawa, Y., U.S. Patent 5,785,947 (1998).

22. (a) Wagner, P.; Medrud, R. C.; Davis, M. E.;Zones, S. I. Proceedings of the 12th Int'l Zeol. Conf., July 1998, Baltimore, Recent Progress Reports Poster Abstract ,RR

(b) Wagner,P; Medrud, R. C.; Davis, M. E. ; Zones, S. I., *Angew. Chem. Int Ed.*, in press **1999**.

23. Simmen A.; McCusker L.B. ; Baerlocher Ch.; Meier W.M *Zeolites* **1991**, *11*, 654.

24. Vortman, S.; Marler, B.; Gies, H.; Daniels, P. *Microporous Materials*, **1995**, *4*, 111.

25. Camblor, M. A.; Corma, A.; Lightfoot, P.; Villaescusa, L. A.; and Wright, P. A. *Angew. Chem. Int'l. Ed.,* **1997**, 36, 2659.

26. Treacy M.M.J., Deem M.W., Newsam J.M., DIFFaX Version 1.801 (**1995**)

**Table 6.1.** Substituted Monocyclic Quaternary Ammonium Structure Directing Agents (SDAs).

| Entry # | Structure |
|---|---|
| 2 | 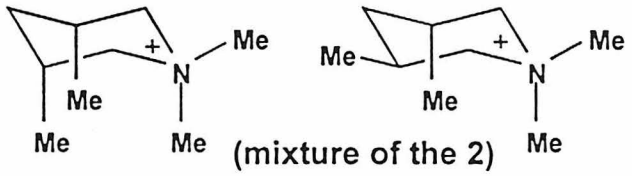 (mixture of the 2) |
| 3 | 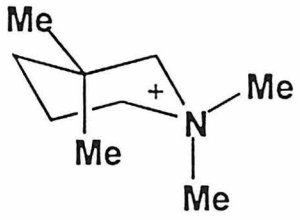 |
| 4 | 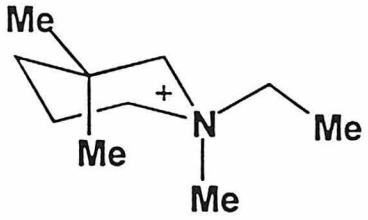 |
| 5 | 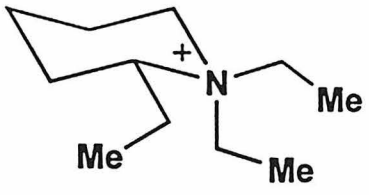 |
| 6 | 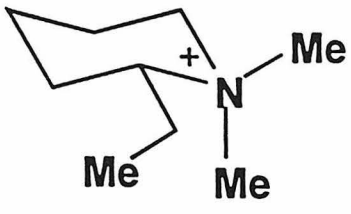 |

**Table 6.1(cont'd).** Substituted Monocyclic Quaternary Ammonium Structure Directing Agents (SDAs).

| Entry # | Structure |
|---|---|
| 7 | 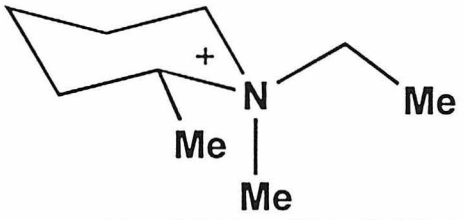 |
| 8 | 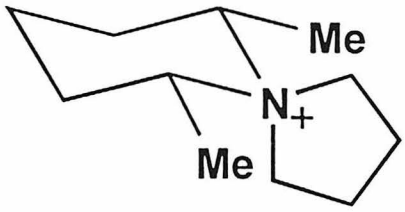 |
| 9 | 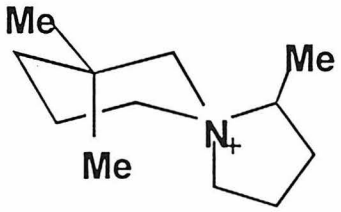 |

*Includes Spirocyclic Derivative 8 and 9

**Table 6.2.** Substituted Bicyclic Quaternary Ammonium Structure Directing Agents (SDAs).

| Entry # | Structure |
|---|---|
| 1 | 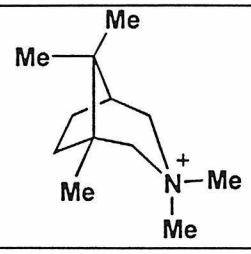 |
| 10 | 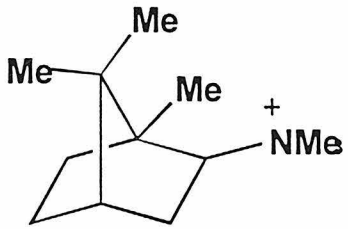 |
| 11 | 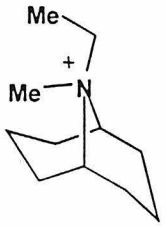 |
| 12 | 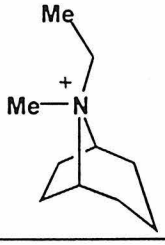 |
| 13 | 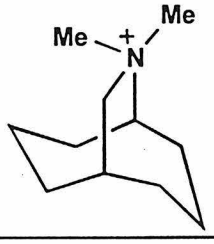 |

**Table 6.2 (cont'd).** Substituted Bicyclic Quaternary Ammonium Structure Directing Agents (SDAs).

| Entry # | Structure |
|---|---|
| 14 | 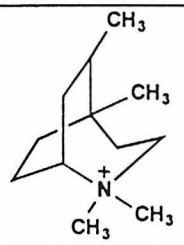 |
| 15 | 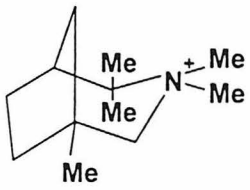 |
| 16 | 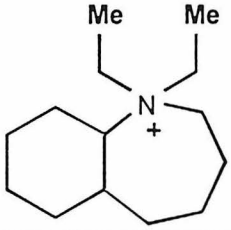 |
| 17 | 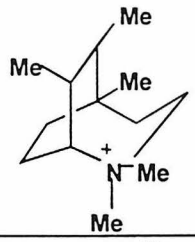 |
| 18 | 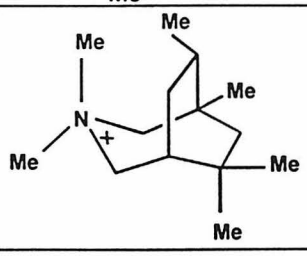 |

**Table 6.2 (cont'd).** Substituted Bicyclic Quaternary Ammonium Structure Directing Agents (SDAs).

| Entry # | Structure |
|---|---|
| 19 | 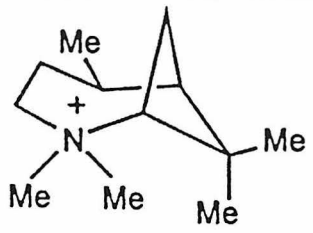 |
| 20 | 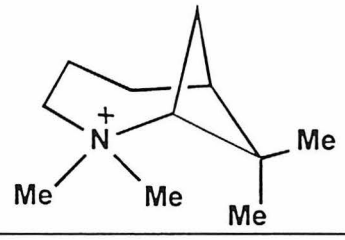 |
| 21 | 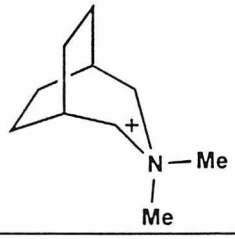 |
| 22 | 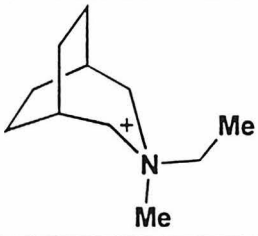 |
| 23 | 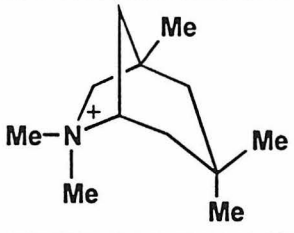 |

**Table 6.2 (cont'd).** Substituted Bicyclic Quaternary Ammonium Structure Directing Agents (SDAs).

| Entry # | Structure |
|---|---|
| 24 | 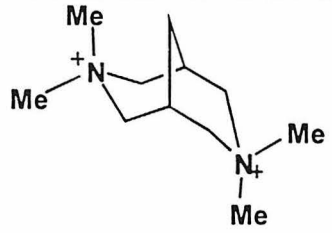 |
| 25 | 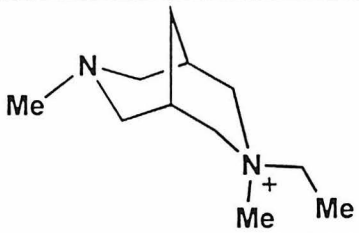 |
| 26 | 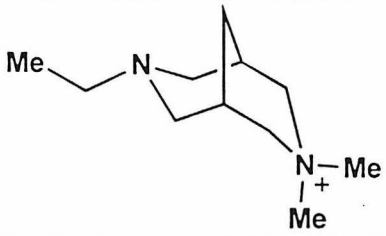 |
| 27 | 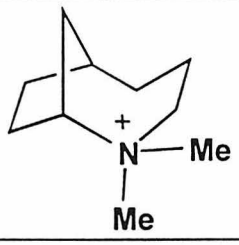 |

**Table 6.3.** Substituted tri- and tetracyclic Quaternary Ammonium Structure Directing Agents (SDAs).

| Entry # | Structure |
|---|---|
| 28 | 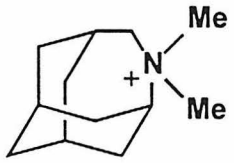 |
| 29 | 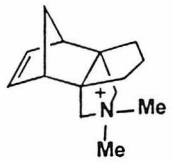 |
| 30 | 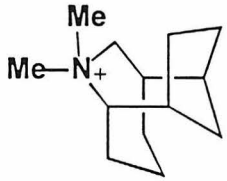 |
| 31 | 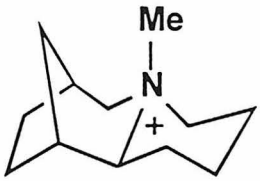 |
| 32 | 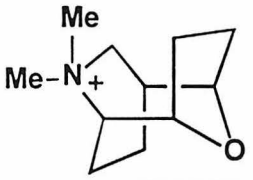 |
| 33 | 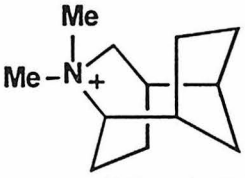 |

**Table 6.3 (cont'd).** Substituted tri- and tetracyclic Quaternary Ammonium Structure Directing Agents (SDAs).

| Entry # | Structure |
|---|---|
| 34 | 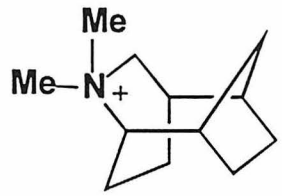 |
| 35 | 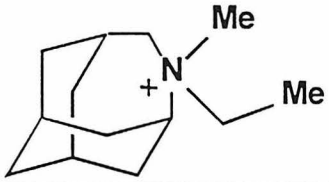 |
| 36 | 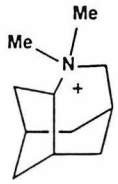 |
| 37 | 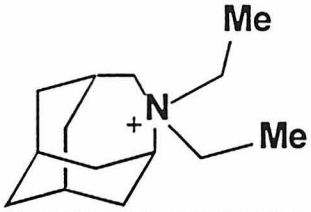 |

**Table 6.4.** Products of zeolite synthesis reactions using organic molecules listed in Tables 1-3. SAR indicates the silica-to-alumina ratio in the synthsis mixture. The syntheses are conducted according to the procedures outlined in the text.

| Entry # | SAR = 30 | 40 | 70 | 100 | >300 | $SiO_z/B_2O_3$= 40 |
|---|---|---|---|---|---|---|
| 1 | SSZ-36 | SSZ-35 | SSZ-35 | SSZ-35 | SSZ-35 | SSZ-35 |
| 2 | SSZ-39 | MFI | MTW | ZSM-S/11 | MTW | SSZ-36 |
| 3 | CHA | CHA | NON | NON | NON | SSZ-36 |
| 4 | CHA | - | EUO | MFI | NON | SSZ-36 |
| 5 | - | MFI | MFI | - | SSZ-31 | SSZ-35 |
| 6 | - | MFI | SSZ-31 | - | SSZ-31 | SSZ-36 |
| 7 | CHA | MFI | MTW | Layer | Layer | SSZ-36 |
| 8 | - | SSZ-35 | SSZ-35 | SSZ-35 | SSZ-31 | SSZ-35 |
| 9 | CHA | CHA | CHA | - | Layer | SSZ-33 |
| 10 | | SSZ-36 | | | | |
| 11 | CHA | SSZ-35 | SSZ-35 | SSZ-35 | SSZ-35 | SSZ-35 |
| 12 | CHA | CHA/DDR | - | - | DDR | SSZ-35 |
| 13 | - | - | - | - | SGT | SSZ-35 |
| 14 | - | SSZ-35 | SSZ-35 | SSZ-35 | SSZ-35 | SSZ-35 |
| 15 | SSZ-36 | SSZ-36 | SSZ-35 | SSZ-35 | SSZ-35 | SSZ-36 |
| 16 | SSZ-36 | - | SSZ-36 | SSZ-36 | - | - |
| 17 | SSZ-36 | SSZ-36 | SSZ-36 | SSZ-35 | - | SSZ-36 |
| 18 | SSZ-36 | SSZ-36 | SSZ-36 | SSZ-36 | - | SSZ-36 |
| 19 | SSZ-36 | SSZ-36 | SSZ-36 | SSZ-36 | SSZ-35 | SSZ-36 |
| 20 | SSZ-39 | SSZ-35 | SSZ-35 | SSZ-35 | SSZ-35 | SSZ-35 |
| 21 | Mord | SSZ-28 | DDR/SGT | - | DDR | SSZ-35 |
| 22 | CHA | - | - | - | NON | SSZ-35/CHA |
| 23 | SSZ-39 | SSZ-35/36 | SSZ-35 | - | SSZ-31 | SSZ-36 |
| 24 | CHA/Mord | SSZ-35 | SSZ-35 | SSZ-35 | SSZ-35 | SSZ-35 |
| 25 | CHA | SSZ-35 | SSZ-35 | SSZ-35 | SSZ-35 | SSZ-35 |
| 26 | Mord | MFI | MFI | SSZ-35 | Layer | - |
| 27 | CHA | DDR | DDR | NON | NON | DDR |
| 28 | CHA | SSZ-35 | - | SSZ-35 | SSZ-35 | SSZ-35 |
| 29 | SSZ-35 | SSZ-35 | - | SSZ-35 | SSZ-35 | - |
| 30 | SSZ-36 | SSZ-35 | - | - | SSZ-35 | SSZ-35 |
| 31 | CHA | SSZ-31 | SSZ-31 | SSZ-35 | SSZ-31 | SSZ-35 |
| 32 | - | DDR | - | - | DDR | SSZ-35 |
| 33 | - | DDR | - | - | DDR/35 | SSZ-35 |
| 34 | SSZ-35 | SSZ-35 | - | - | DDR/35 | SSZ-35 |
| 35 | CHA | SSZ-35 | SSZ-24 | SSZ-35 | - | SSZ-35 |
| 36 | CHA | SSZ-35 | SSZ-35 | SSZ-35 | SSZ-35 | SSZ-35 |
| 37 | CHA | CHA | SSZ-24 | SSZ-24 | SSZ-24 | |

**Table 6.5** Stabilzation energy for Entry 29 (Table 3) in the cages of competing zeolite phases

| Zeolite | Compound 29, kcal/Cage |
|---|---|
| ITE | -19.9 |
| RTH | -18.8591 |
| SSZ-39 | -6.79554 |
| SSZ-35 | -20.87 |

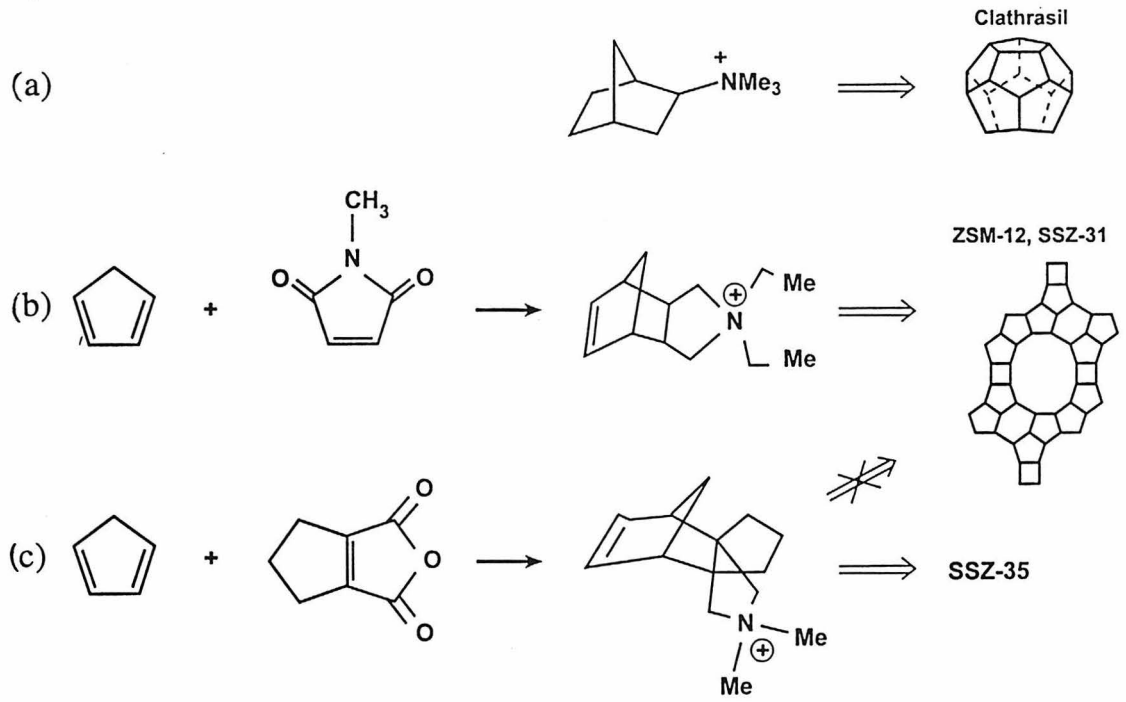


**Figure 6.1.** Three guest molecules based upon extensions of the Diels-Alder reaction and the types of zeolites generated as spatial features change:

(a) The norbornyl derivative is still small enough to generate cage-centered clathrate structures like nonasil ( NON).

(b) The tricyclic derivatives with long, central axes produce one-dimensional, large pore zeolites.

(c) The pseudo propellane developed in this guest leads away from one-dimensional large pore zeolites and generates zeolites with cavities like SSZ-35.

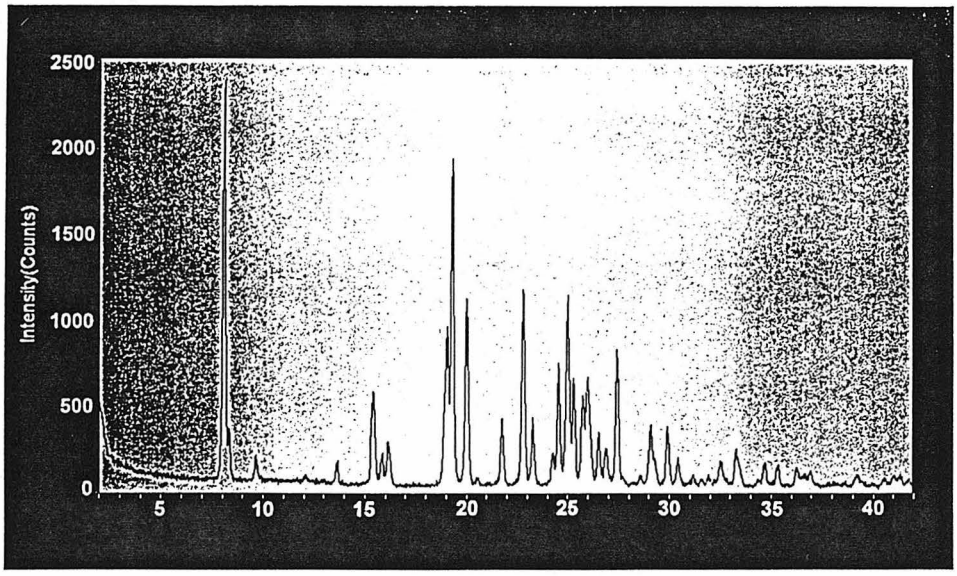


**Figure 6.2.** An X-ray powder diffraction pattern for SSZ-35.

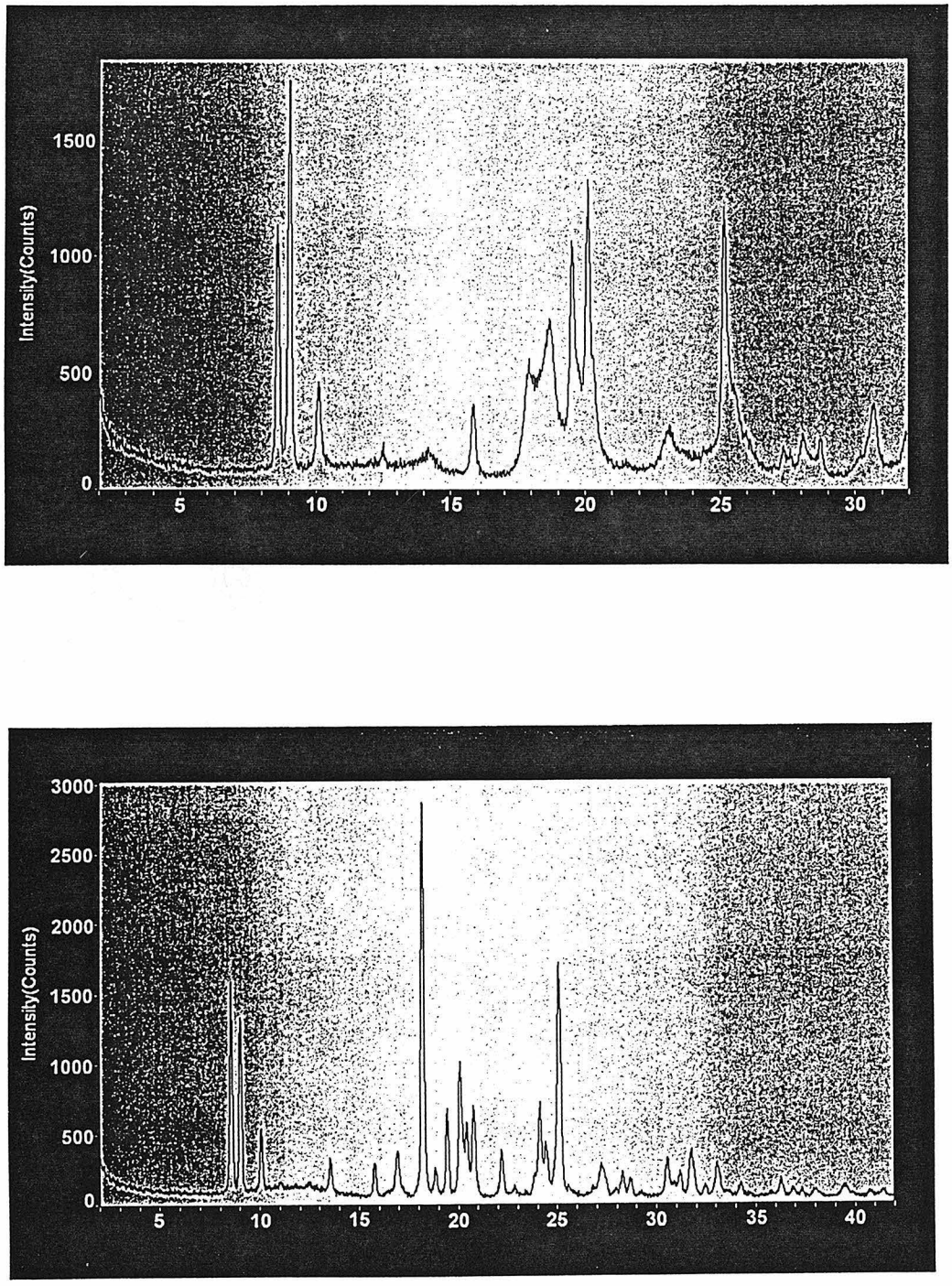


**Figure 6.3.** Two examples of X-ray powder diffraction patterns for SSZ-36: (a) from a synthesis using Entry 1 and (b) from Entry 18.

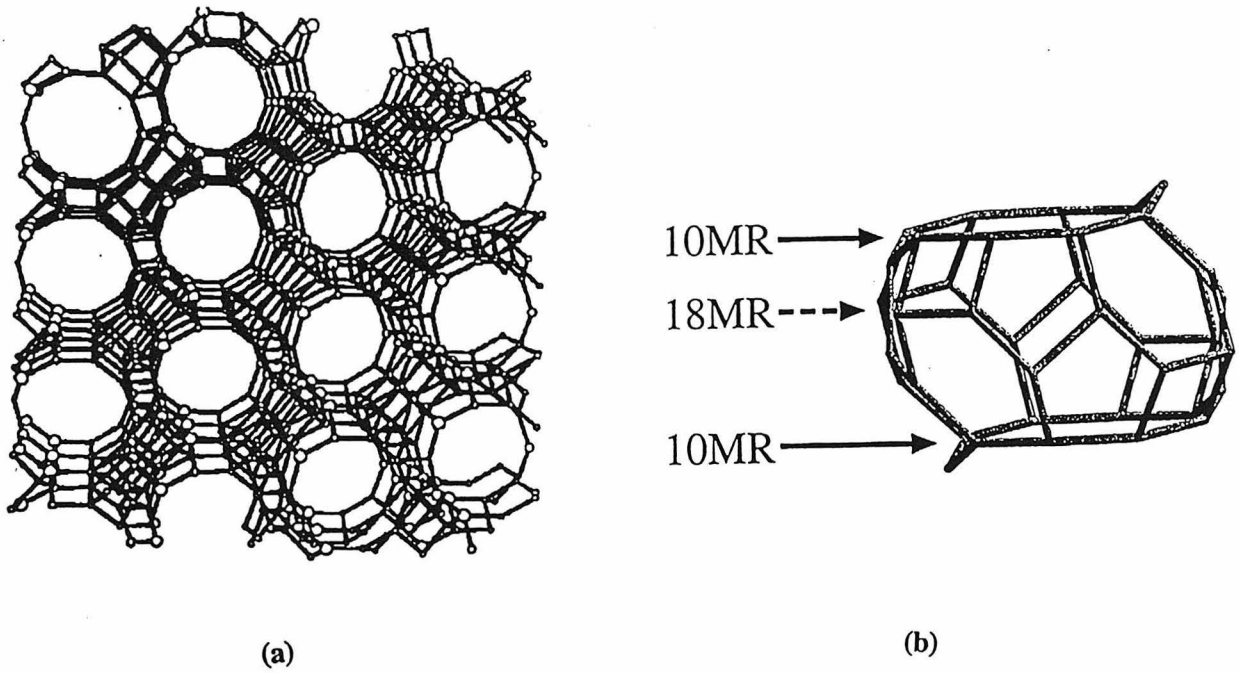


**Figure 6.4.** A framework representation of SSZ-35 showing the 10-ring portals leading into larger cavities.

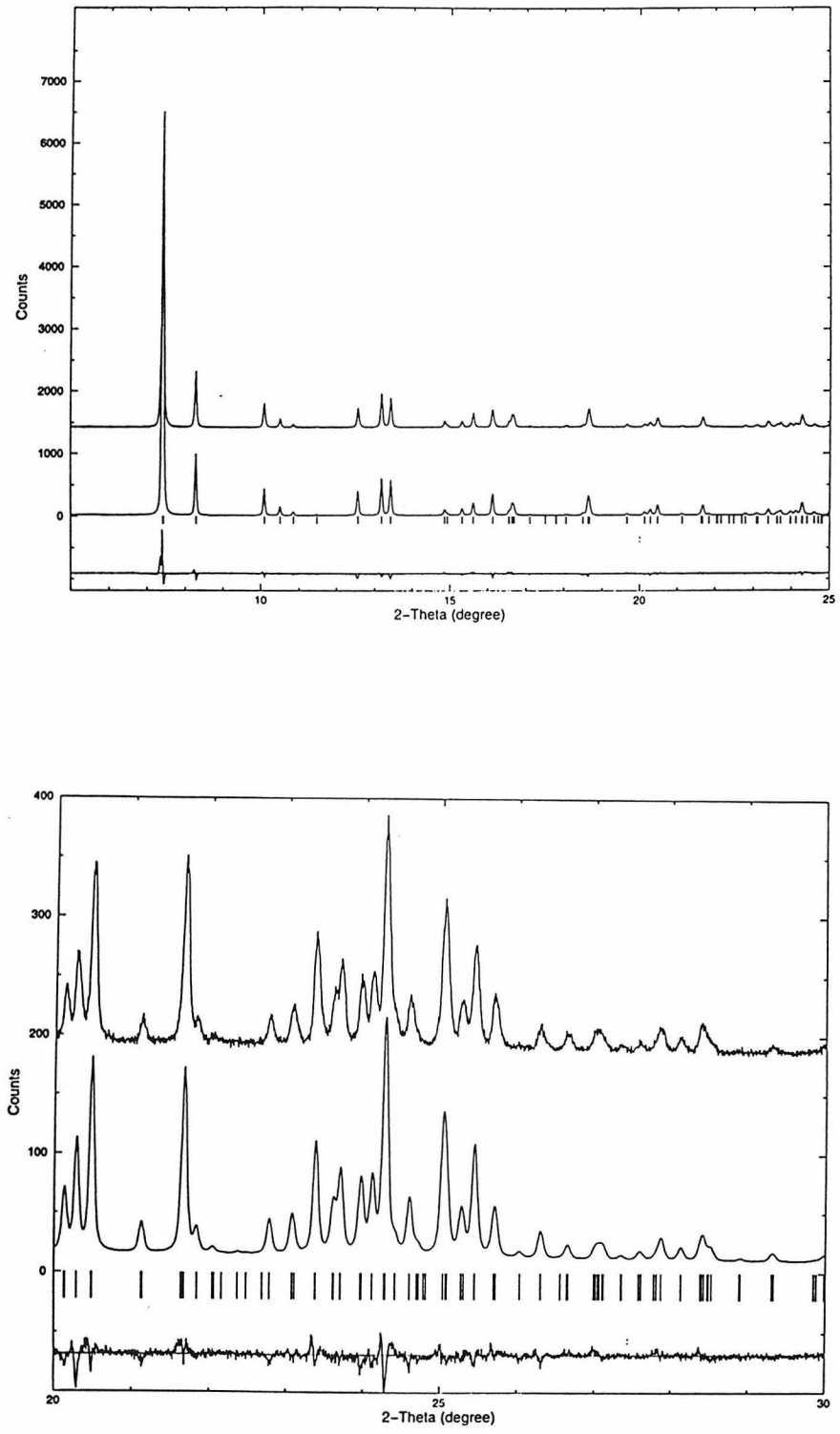


**Figure 6.5.** Calculated and experimental ( synchrotron data ) diffraction patterns for SSZ-39.

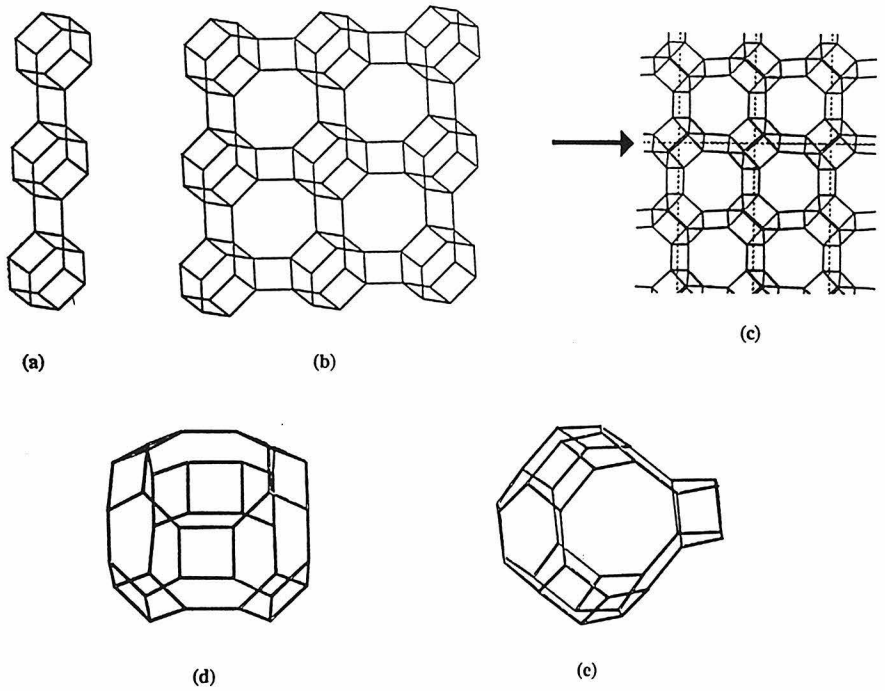


**Figure 6.6.** Linkages for the chains and connectivities used to construct the cavities in SSZ-39.

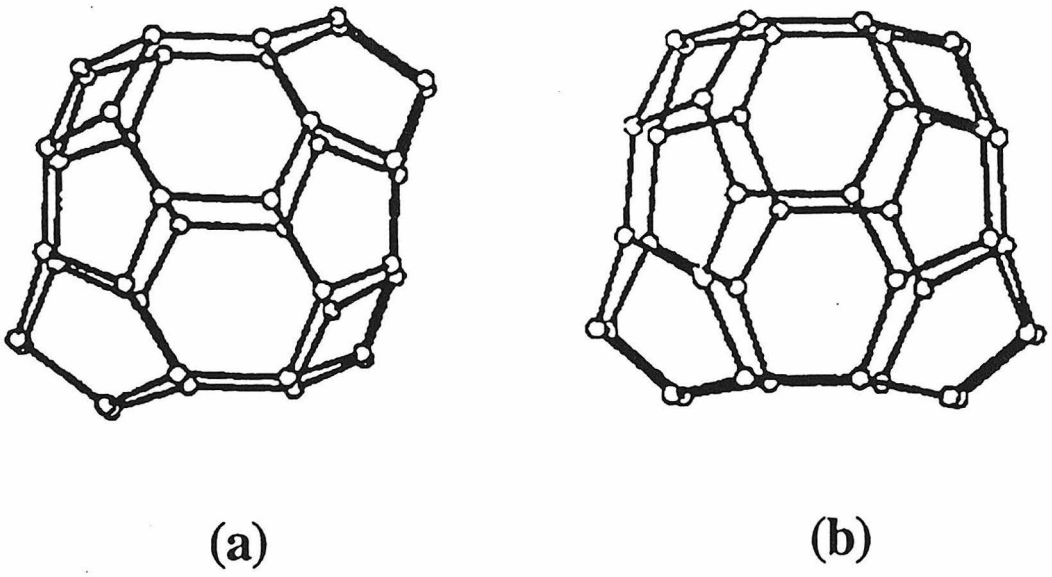


**Figure 6.7.** A comparison of the cage constructions for ITE and RTH (left). It can be seen that a difference of one symmetry operator results in the two unique structures (taken from Reference 25).

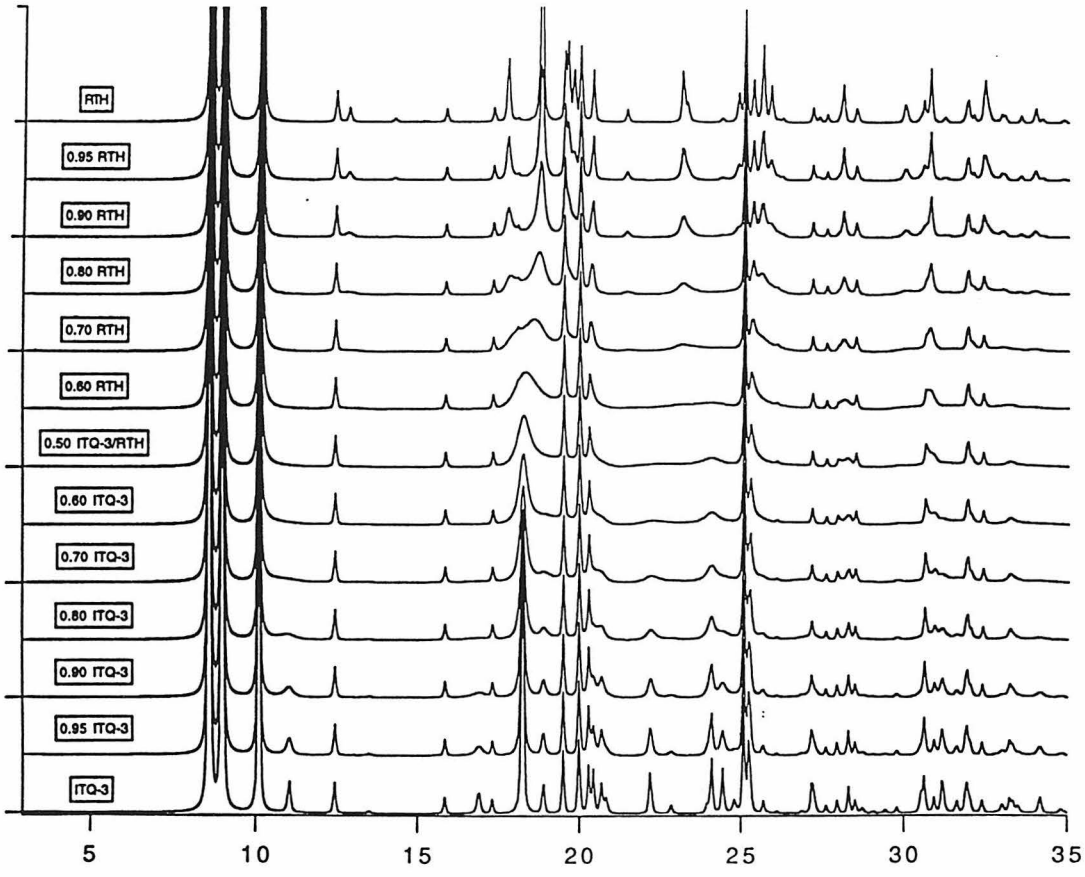


**Figure 6.8.** DIFFaX analysis for simulation of polymorph intergrowth from end members ITE and RTH.

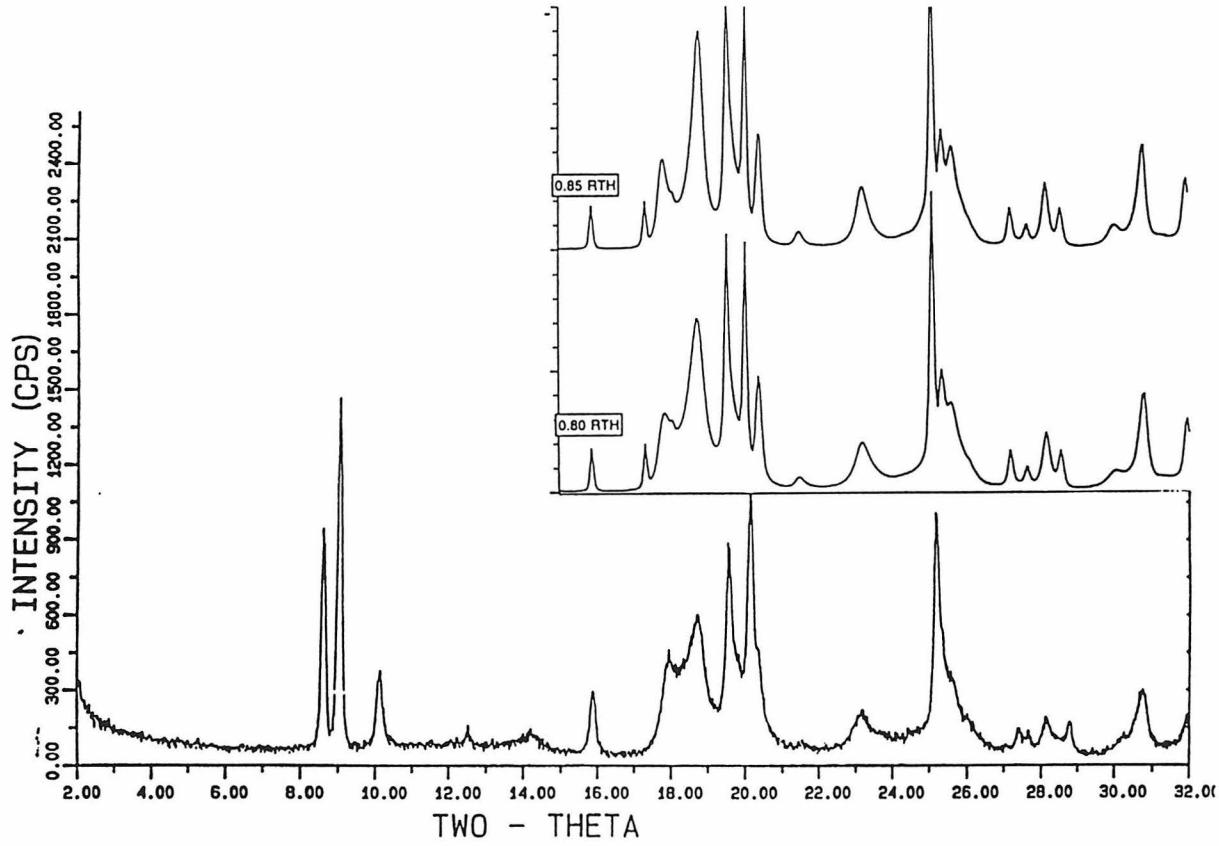


**Figure 6.9.** A comparison of the experimental XRD powder data from Figure 3(a) and the DIFFaX modelling of polymorph mixtures in the range of RTH having 80% probability.

# Supplementary Material For Chapter Six

# Synthesis of the 37 Organo-Cations Located in Tables 1-3

ENTRY 1 - The synthesis of N-methyl camphidinium is described in four steps in the patent to Nakagawa [15].

ENTRY 2 - 29.48 grams of 3,5 dimethyl piperidine (cis/trans mixture) was dissolved in 250 mL of methanol. 37.55 grams of $KHCO_3$ were added to this solution. Methyl Iodide (107.5 grams) was added dropwise while the other reagents were stirred. The reaction was stirred for several days at room temperature. The methanol solvent was stripped off, and the residual solids were then triturated with an equal volume of chloroform. Undissolved solids were filtered away, and the chloroform was stripped away. The remaining solid was then recrystallized from an excess of warm isopropanol, with just enough ethanol added to dissolve the solids. White needles were recovered after cooling the solution. 52.6 grams of 2 with a M.P. (melting point) of 273-276∞C was obtained in a first crop: C= 40.28 (40.16), H= 7.27(7.49) N = 5.19 (5.20). The iodide salt was ion exchanged to the hydroxide compound for use in zeolite synthesis. The exchange used AG 1-X8 OH resin, with the resulting solution titrated before use.

ENTRY 3 - The same procedure described for 2 was used with the piperidine being 3,3' dimethyl piperidine. The product had a M.P. of 275-277∞C. The elemental analyses for the iodide salt were C = 40.16 (39.95), H = 7.18 (7.49), N = 5.07 (5.20).

ENTRY 4 - 35 grams of 3,3' dimethyl piperidine were placed in 300 mL of methanol. 70.2 grams of ethyl iodide, which had been passed through a short column of aluminum oxide, was added into solution; and the reaction was heated to reflux using a heating mantle while stirring. The reaction was followed by thin-layer chromatography and cooled after a few days. Diethyl ether was added to force solids out of solution. The solids were then dissolved in 200 mL of water and the pH

subsequently adjusted to 12 using 50% NaOH.. The product was collected via 3200-mL extractions with methylene chloride. The extracts are dried over $Na_2SO_4$, and the latter was then filtered off and the solvent stripped. 37.69 grams of the N-ethyl piperidine derivative was recovered as an oil. This tertiary amine was now suspended in 200 mL of methanol, and the same reaction was carried out as in Entry 2 (13.36 grams of $KHCO_3$ and 76.5 grams of methyl iodide). The product recovered from recrystallization from hot isopropanol and acetone, has a M.P. of 272-273∞C. It analyzed for C = 42.34 (42.41), H = 7.65 (7.83), and N = 4.74 (4.95).

ENTRY 5 - 47.17 grams of 2-ethyl piperidine was reacted with 93.58 grams of ethyl iodide in 400 mL methanol in a manner like ENTRY 4 above. After 2 days the reaction was stopped; and with similar work-up, 37.2 grams of oil was collected. 18.6 grams of this oil was reacted with another charge of ethyl iodide (41 grams) and 6.59 grams of potassium bicarbonate in 130 mL methanol at reflux. After the work-up as in 4, and recrystallization from hot acetone/isopropanol, 20.27 grams of crystals was collected with M.P. = 252-254∞C. C = 44.49 (44.45), H = 7.60 (8.14), N = 4.70 (4.71).

ENTRY 6 - The product was prepared as in 2, starting with 2-ethyl piperidine. M.P. = 278-279∞C; C = 40.55 (40.16), H = 7.53 (7.49), N = 5.13 (5.20).

ENTRY 7 - Starting with 2-methyl piperidine, the same reaction as in Entry 5 was carried out to make the mono N-ethyl derivative. The product oil was then reacted with excess methyl iodide (dropwise) in methanol. After forcing the product out with ether, the solids are recovered and recrystallized from acetone/methanol. A third crop, the largest fraction collected, has M.P. = 301-304∞C. Analyzed as C = 39.93 (40.16), H = 7.54 (7.49), N = 4.81 (5.20).

ENTRY 8 - 22.87 grams of 2,6 dimethyl piperidine was placed in a reaction flask with 50 mL methanol and 30 grams potassium bicarbonate as base. With

dropwise addition, 61.94 grams of 1,4 diodobutane was added. The reaction was stirred at room temperature for 4 days. Next the methanol was stripped off. The residual solids are treated with 100-200 mL chloroform and the undissolved solids are removed. The remaining solution was treated with diethyl ether until solids precipitate. The solids are dissolved in 200 cc water and the pH was adjusted to 12. 3100-mL extractions are carried out with methylene chloride. The extracts are dried with sodium sulfate. The dried solution was then stripped off and the solids are recrystallized from hot acetone/methanol. The resulting crystals have M.P. =280-282∞C and C = 44.77 (44.76), H = 7.53 (7.51), N = 4.45 (4.75).

ENTRY 9 - The same type of reaction as in 8 was carried out except 3,3' dimethyl piperidine was reacted with 1,4 dibromopentane. Work up in the same manner as 8, except skipping the basification with water and proceeding directly to recrystallization (acetone/methanol); after recovery in chloroform, yields a product with a M.P. = 256-258∞C. It analyzed as C = 54.88 (54.96), H = 9.17 (9.22), N = 5.13 (5.34).

ENTRY 10 - Exhaustive methylation of bornylamine was carried out as in ENTRY 1.

ENTRY 11 - The skeleton for this polycyclic molecule was constructed from the use of a Mannich reaction. A 5-liter flask was set up with condenser and nitrogen sweep capability. 140 grams of glutaraldehyde and 630 mL of water are placed in the flask. 70.66 grams of methylamine hydrochloride in 700 mL water was added next. 116.6 grams of acetone dicarboxylic acid in 1162 grams of water was added in; and also, a solution 123 grams of sodium phosphate, dibasic, and 10.22 grams of NaOH (s) in 280 mL water was placed in the flask. The reaction was stirred at room temperature, and a bubbler was used to monitor gas sweep and evolution. Next add 46 mL of concentrate HCl and reflux for 1 hour to complete the decarboxylation. Then add 105 grams of NaOH (s) in 140 mL of water followed by 8

extractions (250 mL each) with methylene chloride. Dry over sodium sulfate and strip down. 103 grams was collected. Next, the carbonyl functionality was reduced via Wolff-Kischner reduction. 44 grams of the oil was added into a 2-liter flask also containing 1351 mL of triethylene glycol, 148 grams of KOH (s), and 36.75 grams of hydrazine, which are added last and slowly to contain the exotherm. Slowly bring the reaction to reflux and maintain for 8 hours. Upon cooling, replace the condenser with a distillation head. Add boiling chips to the flask and begin to raise the temperature Collect distillate until the head temperature was 215∞C. Extract the distillate with chloroform (2 x 150 ml). Add 150 mL water to the extracts and lower pH below 2. Repeat a second low pH treatment of the chloroform phase. Now add NaOH to bring pH above 12 and back-extract with ether (4 x 200 mL). Dry over sodium sulfate and strip. This produces the free, tertiary amine. 7.0 grams of the amine was reacted with ethyl iodide in chloroform. The resulting product was recrystallized from hot methanol/ether to give a M.P. = 316-319∞C. The product analyzed for C = 44.80 (44.75), H = 7.59 (7.51), and N = 9.53 (9.44).

ENTRY 12 - Starting with tropinone, the same Wolff-Kischner reduction and subsequent alkylation was carried out as in ENTRY 11: C = 42.53, H = 7.03, N = 4.97.

ENTRY 13 - Bicyclo [3.3.1] nonane–9-one was converted to the lactam as follows: 8.67 grams of the ketone was placed in 61 mL formic acid (96%). With an addition funnel, 10.86 grams of hydroxylamine-o-sulphonic acid in 32 mL formic acid was added dropwise. The mixture was refluxed for 24 hours. Next pour the reaction onto 500 grams of ice and then adjust pH to above 12 with 50% NaOH. Extract with methylene chloride (3 x 100 mL). Dry with sodium sulfate and then strip down. Using a column of 120 grams of silica gel (230-400 mesh) slurried into chloroform, the oil was loaded in a minimum of chloroform; and then the column was eluted with 98/2 chloroform/methanol. Following the fractionation by TLC, 4.85 grams of the lactam

was recovered after stripping down the relevant fractions. The lactam was reduced to the amine using lithium aluminum hydride (LAH, caution in using). A three-neck , 200-mL round bottom flask with condenser, gas bubbler, and addition funnel was set up. 1.86 grams of LAH was carefully added to 46 mL anhydrous ether in the flask. 4.75 grams of lactam in 23 mL methylene chloride was added slowly from the addition funnel. A dry ice/acetone bath was used to control temperature. As the reaction was stirred and allowed to come to room temperature, it was monitored by TLC for the loss of the lactam. By the next day reaction looks complete. Carefully add 1.9 grams of water, generating considerable gas evolution. Next, 1.9 grams of 15% NaOH was added; and then an additional 5.6 mL of water was added last. After stirring for a while, the solids are filtered off and washed with additional methylene chloride. The combined organic solutions are treated first with acidic solution, and then the high pH modification and ether extraction was carried out as in ENTRY 11 to iberate the amine. 3.80 grams of the amine was alkylated with methyl iodide as in ENTRY 2. Recrystallization from hot isopropanol/methanol yielded slightly purple flakes. The M.P. was 300-302∞C and C = 44.90 (44.75), H = 7.57 (7.51) and N = 9.61 (9.43).

ENTRY 14 - This guest molecule was constructed from a single ring construction step via Michael Addition between a lithium-stabilized dienolate and an activated olefin. Then a number of side-chain modification steps were carried out, finally leading to a ketone. The ketone was transformed to lactam, amine, and quaternary ammonium product in the same sequence of steps as given for ENTRY 13. A three-neck, 5-liter flask was set up with additional funnel with equalization arm. A septum was placed over the funnel. Nitrogen was passed through the system. First an in-situ reagent was developed by placing 104.55 grams of diisopropylamine in 1859 mL of tetrahydrofuran (THF) and then slowly adding 401.7 mL of n-butyl lithium (2.5 M in hexane) while keeping the temperature near –70∞C. The n butyl lithium was charged to the addition funnel by use of a cannula. The addition into THF

took about 1.25 hours. Stir for another hour. 104.53 grams of 3-methyl-2-cyclohexene-1 one in 1117 mL THF was added dropwise over a 0.75-hour period. Lastly, add 161.73 grams of methyl acrylate over a period of 0.25 hour. Gradually allow the reaction to warm to room temp and follow progress by TLC. The reaction appears to go overnight. The work-up was begun by adding 1N HCl until the solution becomes acidic. Transfer to separatory funnel and recover the aqueous phase to subsequently treat with methylene chloride (2 x 250 ml). Dry the combined organic phase over sodium sulfate and then strip solvent. The residue was taken up in ether to free it from a little gummy material. The ether was removed and the oil was distilled; a Vigreaux column (30 cm) was set up and run at 2-4 mm Hg. The bulk of the product comes over between 123-137∞C. A number of earlier studies have indicated that the stereochemistry for this first ketoester product have both carbonyls ($C_2$ and $C_5$) syn to each other [44a]. This product was next reduced using the same LAH reduction procedure described for ENTRY 13. The reduction produces a diol, 1-methyl, 2-methanol, 7 hydroxy bicyclo [2.2.2] octane. The side methanol group was tosylated by reaction of tosyl chloride (96.92 grams) with the diol (85.68 grams) in anhydrous pyridine (500 ml). The tosyl chloride was added to the other two components, under nitrogen, via addition using a powder addition funnel while cooling the reaction to –5∞C. The addition was carried out over 0.75 hour. Warm to room temperature and run overnight. Add 500 mL methylene chloride, transfer to a separatory funnel, and wash with water (2 x 250 mL ). Dry over sodium sulfate, filter, and strip to yield 150 grams of oil. The product was purified by column chromatography. A kilogram of silica gel (230-400 mesh) was slurried in hexane, and the oil was loaded on top in 50 mL methylene chloride. The elution was carried out using 25/75 ethyl acetate (ETOAC); hexane and fractions are monitored by TLC. 83 grams of product was collected. The tosylate was then reduced using LAH (as above) to yield 1,2 dimethyl, 7 hydroxy bicyclo [2.2.2] octane. Next, the alcohol was reoxidized to the ketone.

37.84 grams of the alcohol was reacted in a three-neck, 2-liter flask as follows: 34.60 grams of oxalyl chloride and 604 mL of methylene chloride are loaded in and blanketed under nitrogen. With an addition funnel with side arm, 46 grams of anhydrous dimethylsulfoxide (DMSO) in 122.7 mL of methylene chloride was added. The bath was cooled to –60∞C using a dry ice/acetone bath, and the addition takes 0.5 hour. The alcohol, in 53.4 mL methylene chloride, was added at this temperature over 0.5 hour. Stir another 0.5 hour. Next, place 126.65 grams of triethylamine in the addition funnel. Begin addition and continue over 0.25 hour. All of the additions produce exothermic response, so continue to cool. Slowly warm to room temperature and continue to run overnight. Work-up begins with addition of 500 mL water. The separated aqueous phase was then extracted with methylene chloride (2 x 250 ml) . The combined organic phases are then dried over magnesium sulfate and then stripped. The oil was triturated with ether to separate a small amount of insoluble material. Stripping off ether yields 37 grams. The product ketone was then carried through the same oxime-to-lactam-to-amine steps as in ENTRY 13. This yields a mixture of two amine isomers (nitrogen at ring position 2 or 3). The mixture was alkylated with methyl iodide, as described in ENTRY 2. Recrystallization from hot acetone/methanol gives the 2-position isomer selectively (M.P. = 278-281∞C).

ENTRY 15 - The synthesis of the eventual target molecule begins with the reaction of 98 grams of (1R)-(-)-fenchone (as the ketone) with 112 grams of hydroxlamine-o-sulfonic acid in formic acid (970 mL total) as described above . Two isomeric lactams may form. The lactams are collected via chromatography, as described above. Next, reduction was carried out using LAH, as described above. Alkylation, as in ENTRY 2, was carried out. Recrystallization from hot acetone/methanol yielded flakes, M.P. = 274-275∞C.

ENTRY 16 - The same procedures are carried out as in ENTRY 15, starting with 64.53 grams of trans-1-decalone. The last step was alkylation with ethyl

iodide, as in ENTRY 5. The product from hot acetone/methanol had M.P. = 214-217∞C.

ENTRY 17 - The same lengthy reaction sequence as in ENTRY 14 was begun with 90 grams of 3-methyl-2-cyclohexen-1-one, but the addition component this time was 163.56 grams of methyl crotonate (replacing the previous methyl acrylate). The same sequence of steps was carried out: LAH reduction to diol, formation of tosylate, rereduction, oxidation to the mono ketone, formation of the oxime, rearrangement of the lactam, reduction to the amine, methyl iodide alkylation, as in ENTRY 2. Recrystallization from hot acetone/isopropanol yielded M.P = 250-255∞C.

ENTRY 18 - The same reaction as in ENTRY 14 was carried out but using isophorone (119 grams) as the entry ketone. The final alkylation step, as in ENRY 2, yields solids with M.P. = 226-228. NMR shows a mixture of isomers for nitrogen at 2 or 3 position.

ENTRY 19 - The entry ketone, in this instance, was first prepared by hydrogenating 20 grams of the unsaturated keto compound, verbenone, using 2 grams of Pd on activated carbon in 200 mL absolute ethanol. The reduction was carried out in a Parr hydrogenator at 60 psi hydrogen. The reaction mixture was filtered through a short column of celite/silica gel, rinsing with ethanol. A different procedure was used this time for a two-step formation of the oxime and then lactam. 72.9 grams of the ketone was combined with 40.34 grams of hydroxylamine hydrochloride, 78.57 grams of sodium acetate (tri hydrate), 435 mL ethanol, and 218 mL water. This mixture was then refluxed for about 2 hours. The cooled mixture was worked up by pouring into a brine solution and extracting with chloroform (3 x 250 ml), drying over sodium sulfate, and then stripping. The lactam was formed next by reacting 88 grams of the oxime with tosyl chloride (153 grams), potassium carbonate (185 grams) in 768 mL dimethoxy ethane, and 666 mL water. This mixture was refluxed for 6 hours (80∞C).

Next, remove the dimethoxyethane in a rotoevaporator. The aqueous phase was extracted with chloroform (3 x 250 ml), and the latter was washed once with 300 mL brine and then dried over sodium sulfate. 76 grams of oil was recovered. Purification on silica gel (2 kg) slurried in hexane and used as described above gave 58 grams of isolated product. The same steps were then carried out to reduce (LAH) the lactam and alkylate (ENTRY 2) to the dimethyl ammonium derivative. Recrystallization from hot acetone gave a product with M.P. = 215-220∞C.

ENTRY 20 - The same procedure as described above for ENTRY 19 was used to transform 40 grams of (1R)-(+)- nopinone to the lactam. Subsequently, the same LAH reduction and methyl iodide alkylation steps were carried out. From hot acetone/isopropanol, a product was recovered with M.P = 241-245∞C.

ENTRY 21 - This compound was prepared from 3 aza bicyclo [3.2.2] nonane reacting with methyl iodide, as in ENTRY 2.

ENTRY 22 - Using the same amine as in ENTRY 21 and the procedure for ENTRY 4, the mixed methyl/ethyl derivative was made. The product was recrystallized from hot acetone/methanol and a slight bit of ether. M.P = 256-258∞C and C = 43.50 (44.75), H = 7.69 (7.51), N = 4.61 (4.74) C/N = 9.44 (9.44).

ENTRY 23 - Alkylation as in ENTRY 2 was carried out for 1,3,3, trimethyl-6- aza bicyclo [3.2.1] octane

ENTRY 24-26 - The preparation of these compounds has already been described in part [45-47]. The skeleton of these 3,7 diazabicyclo [3.3.1] nonanes was formed by reacting N-substituted 4-piperidones with a mixture of methylamine hydrochloride, glacial acetic acid, and paraformaldehyde. The resulting 9-keto group was eliminated by Wolff-Kischner reduction, as has been described above for ENTRY 11. Subsequent alkyl halide addition to the secondary or tertiary amine gives the desired product.

ENTRY 27 - Starting with bicyclo [3.2.1] octan-2-one, the same oxime and lactam transformations were carried out as in ENTRY 19. LAH reduction lead to the amine, and the dimethyl quaternary derivative was formed as in ENTRY 2. Recrystallizing from hot acetone/methanol gave a solid with a decomposition temperature near 290∞C. By NMR, the product was a 3/1 mixture of the two isomers with 2N position over 3N position.

ENTRY 28 - The reaction was started with the available lactam, 2-aza-tricyclo [4.3.3.1] undeca-3-one. LAH reduction followed by alkylation, as in ENTRY 2, gave the product.

ENTRY 29 - The Diels-Alder reaction was carried out between freshly cracked cyclopentadiene and cyclopentene 1,2 anhydride using previous methods [11]. The anhydride was converted to the imide by refluxing in 40 % methylamine (water) with a catalytic amount of N-dimethyl-4-pyridine (DMAP). The reaction was best carried out using a Parr teflon-lined pressure vessel where the reaction can be carried out in a closed container at 80-90∞C. The resulting imide was reduced with LAH, and the alkylation was carried out as in ENTRY 2.

ENTRY 30 - Using a previously published procedure, the enamine was formed for 3-chloro cyclohexene reacting with pyrrolidine [48]. This compound (27 grams) was reacted with freshly cracked cyclopentadiene in a Diels-Alder reaction. In a dry reaction flask and under nitrogen sweep, 520 mL of methylene chloride was used as solvent for 34 grams of silver tetrafluoroborate. This was cooled to –78∞C (dry ice/isopropanol), and 25 grams of the diene was stirred in. Lastly, the chloroenamine , in 70 mL of methylene chloride, was added dropwise and kept at this temperature for 4 hours. It was slowly brought to room temperature and continued for 12 hours. Filter through a pad of celite and concentrate. Next, this intermediate product was taken up in 200 mL water, 100 mL methanol, and 23 grams of NaOH to drive the formation of the ketone. Reflux for 7 hours and then strip off the methanol. The basic aqueous solution

was extracted with 200 mL ether. Drying over magnesium sulfate and stripping gives a single compound by NMR (62 grams of solid). This polycyclic ketone was converted to the oxime. The reaction was carried by using 1 equivalent of the ketone, 5.5 for hydroxylamine hydrochloride, 40 mL pyridine in 160 mL methanol . Reflux for 1.5 days. The double bond in the other ring was removed via hydrogenation in 100 mL absolute ethanol and 0.25 gram of Pd on carbon for 4.4 grams of olefinic, polycyclc oxime. Hydrogen was used in a Parr hydrogenator at 42 psi. The work-up was as in ENTRY 19. The lactam was formed via use of tosyl chloride in pyridine. For 1 gram of oxime, 3.5 grams of tosyl chloride was mixed in 75 mL pyridine. The mix was stirred at room temperature overnight and then refluxed at 80∞C for 2 hours. Concentrate under reduced pressure and then pass through a silica gel plug using methylene chloride to collect material.

ENTRY 31 - The 3 position of norcamphor was alkylated using 1-chloro-4-iodobutane, reacting 72 grams of the ketone with 178.5 grams of the dihalide, facilitated by the in-situ reagent generated from diisopropylamine (78 grams) and 295 mL of 2.5 M n-butyl lithium in hexane. 900 mL of anhydrous THF was used as solvent. The sequence of addition steps was as in ENTRY 14. The reaction was slowly allowed to come to room temperature after all reagents have been added and stirred. Stir at room temperature for 4 days. The work-up was carried out by partitioning the reaction products between 500 mL of 2N sulfuric acid and 3 liters of ether. The separation must be vigorously shaken. The ether phase was next washed with 500 mL brine, dried over sodium sulfate, and concentrated, yielding 161 grams of a brown oil. A column was prepared using 2 kg of silica gel slurried in hexane as described before. The elution was carried out using a sequence of ETOAC/hexane of 5/95 = 2 gallons, 7.5/92.5 = 1 gallon, and then 10/90 = 1 gallon. By following the fractions with TLC, 122.5 grams of an orange oil was recovered. This was the product with a 4-chlorobutane ring substituent. The butyl termini was next transformed to the

azide by treating 122.5 grams of the previous step product with 200 grams of sodium azide (Caution) in a liter of DMF, heating at 80∞C for 4 hours. The reaction was poured into 5 liters of ether, extracted using water and then brine, dried, and stripped. The azide product undergoes a ring closure by stirring (under nitrogen) 119 grams of it in 2300 mL of a 1M solution of titanium tetrachloride in methylene chloride. Stir for 4 days. Transfer the reaction mixture to a separatory funnel large enough for addition of 4 liters of ETOAC . Wash the organic phases with a liter of saturated sodium carbonate solution and then with 500 mL of saturated sodium chloride solution. Dry over sodium sulfate and concentrate to yield 29 grams of oil. Back-extracting the aqueous phases with chloroform (3 x 500 ml) yields 85 grams of oil. Both isolated materials are the same by TLC. Next purify further using column chromatography. 1.5 kg of silica gel (230-400 mesh) slurried in chloroform has the compound loaded on, and elution was begun using 2/98 methanol/chloroform. Collection of relevant fractions yields 88 grams of the lactam. The lactam was next reduced in methylene chloride/ether using LAH, as described for ENTRY 14. 16.5 grams of the recovered tertiary, bridgehead amine was dissolved in methanol and alkylated with an excess of methyl iodide. Work-up and eventual recrystallization from hot acetone/isopropanol yields crystals with M.P. = 260-262∞C.

ENTRY 32 - This product was prepared as in ENTRY 30 except the starting ketone was 2-chloro cyclopentanone and the second Diels-Alder component used was furan.

ENTRIES 33 & 34 - These two isomeric products were separately recovered from a reaction like ENTRY 30, except the same starting ketone as in ENTRY 32 was used.

ENTRY 35 - The same lactam was used as in ENRY 28. Once the secondary amine was obtained, the product was generated in two steps, as in ENTRY 4. Recrystallization of the final product from hot isopropanol/methanol gave a product

with M.P. = 284-287∞C. The analyses were C = 48.75 (48.61), H = 7.62(7.53), N = 4.34 (4.36).

ENTRY 36 - 1-Adamantanol was oxidized with iodine in the presence of lead (IV) acetate. In a 5 liter flask equipped with mechanical stirrer, nitrogen sweep, reflux condenser, and a heating mantle controlled by a Thermo-watch, 2400 mL of anhydrous benzene was used as solvent for 40 grams of adamantanol, 233 grams of the lead acetate, and 149.6 grams of iodine. The reaction was brought to 70-75∞C after reagent addition. The very thick, jamlike solution becomes difficult to stir during the heat-up. About an hour was used to reach temperature, and then the reaction was held there for 2 hours. Next cool to room temperature, filter off solids, and wash solids with ether (3 x 400 ml). The organic collections are combined and shaken against 2 liters of sodium bisulfite until the dark red color has disappeared. Continue a cycle of letting the separation stand and reshaking if the color comes back after 15 minutes of standing. The organic layer was eventually washed with 1 liter of water and then 1.5 liter of saturated sodium bicarbonate. (Caution: Much gas evolution occurs.) Dry over magnesium sulfate and then remove solvent below 30∞C because of thermal instability of the product . Nearly 100 grams (still contains a little benzene) of this iodomethylene, fragmented adamantanone, was stirred in 600 mL methanol and with 28 grams of KOH (s) was brought to reflux for 3 hours. The reaction mixture was poured onto 1.2 kg ice. Extract with ether (5 x 400 ml), dry over magnesium sulfate, and recover 36 grams of yellow solid. This product was the tricyclo [5.2.1.0] deca-3-one. 8.54 grams of this ketone was given the one-step oxime/lactam formation, as in ENTRY 13 above. Following LAH reduction, the secondary amine (potential mix of two isomers) was alkylated using methyl iodide, as in ENTRY 2. The NMR of the product indicates that it was mainly the isomer shown as ENTRY 36. M.P. = 290-292∞C after recrystallization of hot isopropanol. C = 47.46 (46.91), H = 7.00 (7.22) N = 4.54 (4.56), C/N = 10.45 (10.29).

ENTRY 37 - Starting with the lactam in ENTRY 28, the amine was formed via LAH reduction. The alkylation using ethyl iodide was carried out in a single step. 10 grams of the amine was stirred in 66 mL methanol with 9.93 grams of potassium bicarbonate. 31 grams of ethyl iodide are added and the reaction was brought to reflux. After heating for a day and work-up as in ENTRY 2, recrystallization from isopropanol/methanol yields yellow flakes with M.P. = 270-272∞C. C = 49.92 (50.15) H = 7.83 (7.82), N = 4.12 (4.18 ).

# CHAPTER SEVEN

# Concluding Remarks

In this thesis, the development and application of techniques for solving crystal structures of materials that form as crystals too small for single crystal X-ray analysis have been presented, with a particular emphasis on the structure solution of microporous materials:

- Structure solution of the first ordered 14 MR containing zeolite, CIT-5, using model building (Chapter 2)

- The first application of Fourier recycling to solving the crystal structures of high-silica zeolites (Chapter 3)

- The development and application of electron diffraction methods to solve the structure of a large pore zeolite containing an occluded organic structure directing agent (Chapter 4)

Additionally, the structural information, acquired using these techniques, has been utilized to study the organic/inorganic interactions that lead to zeolite synthesis phase selectivity:

- Molecular modeling results reveal that the strong phase selectivity for CIT-5 by N(1)-methyl-α-isosparteine compared to the diastereomer N(16)-methylsparteinium arises due to the greater number of stabilizing van der Waals interactions of the former within the pores of the high-silica zeolite CIT-5 (Chapter 5)

- Computation studies of the guest/host interactions of 37 designed structure directing molecules and the novel phases that these molecules direct for provides insight into the factors that lead to the observed novel zeolites by the organic structure directing agents (Chapter 6)

The advent of powerful techniques for solving the crystal structure of microporous materials allows detailed structural information to be acquired that has previously proven elusive. Obtaining detailed structural information of the organic SDA/zeolite composite assists the design efforts of the zeolite chemist by providing

insights into the organic/inorganic interactions that lead to zeolite phase selectivity. The combined experimental and computational approaches, presented in this thesis, advance our understanding of the factors that effect zeolite formation, and these investigations highlight the potential for developing a rational route to the design of desirable zeolite frameworks.